Development of a Fabry-Pérot optical interferometer with low thermal and accelerometric sensitivities

Shambo Mukherjee

THESE DE DOCTORAT DE L'ETABLISSEMENT UNIVERSITE BOURGOGNE FRANCHE-COMTE

PREPAREE A L'ECOLE NATIONALE SUPERIEURE DE MECANIQUE ET DES MICROTECHNIQUES

Ecole doctorale n° 37

SPIM

Doctorat de Sciences pour l'ingénieur

Par

Shambo MUKHERJEE

Development of a Fabry-Pérot optical interferometer with low thermal and accelerometric sensitivities

Réalisation d'un interféromètre optique de Fabry-Pérot à faibles sensibilités thermique et accélérométrique

Thèse présentée et soutenue à Besançon le 10 juillet 2024

Composition du Jury :

Marie HOUSSIN	Professeure, Université Aix-Marseille	Rapportrice
Thomas LEGERO	Chercheur, PTB	Rapporteur
Jérôme DELPORTE	Ingénieur, CNES	Examinateur
François VERNOTTE	Professeur, Université de Franche-Comté	Examinateur
Yann KERSALÉ	Professeur, ENSMM	Directeur de thèse
Clément LACROÛTE	Chargé de recherche, CNRS	Co-directeur de thèse
Jacques MILLO	Ingénieur de recherche, ENSMM	Membre invité

Acknowledgement

I would like to express my deepest gratitude to my supervisors, Clement, Jacques, and Yann, for their unwavering support, guidance, and encouragement throughout my PhD journey. From the very beginning, they believed in my potential, constantly motivating me to push boundaries. Their expertise, insightful feedback, and remarkable patience helped shape this thesis into what it is today. I truly couldn't have reached this point without their mentorship, and for that, I am forever grateful.

A special thank you to Fabienne and Sarah for helping me navigate the administrative maze. And of course, a big shoutout to the cleaning lady, whose cheerful smile each morning was an unexpected but much-appreciated boost to my day.

I also want to extend my heartfelt thanks to everyone in the Time and Frequency department. Your collective knowledge, expertise, and collaboration provided the perfect environment for my research to thrive. If I've forgotten anyone, it's not because you weren't important—it's because my brain is still recovering from this whole PhD ordeal!

This journey, as we all know, was not without its challenges. There were many ups and downs, but thankfully, I had a crew of friends and colleagues who kept me sane (most of the time).

A special shoutout goes to Anthony for always being that friend in need. I promised to write a paragraph about you if I somehow survived this PhD journey, so here it is. The most gloriously annoying friend ever—you're the guy who made me eat raw tuna with mustard sauce and called it "lunch," and the same genius who taught me how to cool down a heated laptop with a pack of frozen chicken (because why not?). Let's not forget some of our more questionable late-night adventures in the lab during covid times that are probably best left vague, but still legendary. You've been my travel buddy all over Europe and my partner in annoying my already-annoying sister, Sweta (though I think you're secretly her favorite). Most importantly, you somehow helped me stumble through a PhD in metrology, despite my nearly non-existent knowledge of hands-on optics. Honestly, one paragraph doesn't even begin to cover it all, so I'll just keep the rest of our adventures to myself—for everyone's sake!

Martina, your emotional support was like a life raft in the stormy seas of this PhD. Thank you

for being that friend with the “I’ll sue anyone who crosses me” energy—it’s honestly iconic! People might think you’re all tough and scary, but to me, you’re just a giant marshmallow with a big heart (don’t worry, I won’t ruin your reputation). Special shoutout for the time you stopped the car in the middle of the road so I could puke my guts out—classic me, right? And thank you for not canceling that Munich trip despite my questionable hangover. You’re a legend!

Mario, thank you for your… let’s call them questionable jokes—they somehow managed to make even the darkest days a bit brighter.

Martin, bless you for putting up with all my coding questions and random disturbances—you’re basically a Python and FreeCAD wizard at this point.

Josipa, we’ve been partners in misery, but honestly, I couldn’t have asked for a better co-pilot on this rollercoaster of suffering. Thank you for always being there to listen to my rants and then hit me with the brutally honest advice I probably didn’t want but definitely needed. You’re like a life coach, but with more sarcasm and less sugar-coating.

Falzon, my wonderful office mate, thank you for keeping me grounded and for being my mental support buddy.

Jana, thank you for always being the stable, understanding friend who listened to my rants and offered sage advice.

Alok, your support was invaluable—thank you for always having my back.

Kevin, the farmer with a PhD. You are and have always been the best.

Meriem, thank you for making me deaf due to your laugh from downstairs..But also for being a sweet friend to gossip about multiple stuff..

Isha, thank you for being one of the coolest Indian friends.

And Yara, you’re easily one of the coolest and sweetest people I’ve shared an office with—despite your incredible talent for being completely negative about everything! You kept things real, and our office chats were always a highlight. Honestly, I wouldn’t have had it any other way!

Geetika, Sweta, Paresh, Ria, and Daksh, you’ve been my unwavering support team, offering advice, encouragement, and a listening ear whenever I needed it. I can’t express how much your presence has meant to me.

Above all, I want to thank my family. My parents, the pillars of my life, deserve the highest recognition. Their unconditional love and belief in me have been my greatest strength, keeping me going even when the road seemed impossible.

And finally, Sagnika: thank you and this is for you..

Contents

Conclusion and Future Works **121**

Abstract

The measurement of time, one of the most fundamental aspects of human existence, has undergone significant evolution over the centuries. The second, as the base unit of time in the International System of Units (SI), has seen its definition refined with advances in technology and science. Initially defined by Earth's rotation, the second found a more stable reference in the transition frequency of the Caesium atom in 1967 by the Conférence Générale des Poids et Mesures (CGPM), marking a significant leap in precision and reliability. However, the relentless pursuit of even greater accuracy has led to the development of optical atomic clocks using ultra-stable lasers and optical frequency combs.

The definition of the second based on the Caesium atomic clock was a milestone in metrology, providing a stable and reproducible standard for time measurement. The 9,192,631,770 oscillations of the Caesium-133 atom offered a precision that was unimaginable with previous methods. This era witnessed the widespread adoption of atomic timekeeping in various applications, from global positioning systems (GPS) to telecommunications and beyond. However, the physical limitations of microwave frequencies used in Caesium clocks have prompted the search for more accurate alternatives.

Recent decades have seen the advent of optical atomic clocks, which promise a new frontier in timekeeping. Unlike their microwave counterparts, optical atomic clocks utilize transitions in the optical range, significantly increasing the frequency of oscillations and thus the potential for precision. The core of this innovation lies in the use of ultra-stable lasers and optical frequency combs. Ultra-stable lasers provide the incredibly precise and stable frequencies required for optical clocks, while optical frequency combs serve as rulers to transpose these frequencies with unparalleled accuracy. This synergy has led to the development of clocks that are orders of magnitude more accurate than Caesium atomic clocks, heralding a new era in the definition of the second.

Despite their superior precision in laboratory environments, the practical application of optical atomic clocks faces significant challenges. The primary concerns revolve around their size, weight, and power requirements, which currently limit their deployability in field operations. These challenges are particularly pertinent in scenarios requiring portable and energy-efficient solutions,

such as in remote sensing and defense applications. Efforts to overcome these obstacles are intensifying, driven by the profound impact that enhanced timekeeping precision could have across various sectors. Innovations aimed at miniaturizing these technologies and reducing their power consumption are crucial for enabling a broad range of applications, from improving global navigation systems to enhancing telecommunications and beyond.

A key challenge in the adoption of optical atomic clocks is the dissemination of the highly accurate frequencies and time signals they generate. Optical frequency dissemination via optical fibers emerges as a pivotal technology in this context, enabling the transfer of ultra-precise time signals over long distances with minimal loss of accuracy. This method leverages advanced photonics and telecommunications technologies to maintain the integrity of the optical signals, ensuring that the unprecedented precision of optical atomic clocks can be effectively utilized in applications worldwide. Whether for scientific research, global timekeeping infrastructures, or advanced navigation systems, optical frequency dissemination is critical for realizing the full potential of optical atomic clocks.

This thesis presents the design and realization of an ultra-narrow linewidth laser utilizing a Fabry-Pérot cavity with an optical length of 25 mm working at room temperature. The cavity is made from ultra low expansion glass with optically contacted Fused Silica mirrors. The expected fractional frequency stability of this cavity is 1×10^{-15} at 1-second integration time. The resulting laser system achieves good stability and portability, making it suitable for various applications requiring frequency control. Additionally, the thesis demonstrates the development of a laboratory-scale optical frequency dissemination setup aimed at distributing the ultra-stable frequency generated by this narrow-linewidth laser. The optical fiber link employed in the dissemination setup leverages modern FPGA-based phase-locked loops to ensure simplicity and compactness without compromising on performance. Through experimental validation and analysis, the thesis showcases the effectiveness of this dissemination system in maintaining the stability of the transmitted frequency. Overall, this work contributes to advancing the state-of-the-art in ultra-stable laser technology and optical frequency dissemination, with potential implications for fields such as metrology, communications, and precision instrumentation.

Chapter 1 lays the groundwork by detailing the foundational concepts and theoretical framework surrounding Fabry-Pérot cavities and the dissemination of frequency via optical fibers. This initial chapter also explores the various factors that could potentially hinder the performance of ultra-stable lasers based on Fabry Pérot cavities, alongside the challenges faced in frequency dissemination through optical fiber links. It outlines methodologies for detecting and addressing noise that may affect both the cavity and the link, while concurrently reviewing the current advancements in ultra-stable laser systems and optical fiber link technologies.

Chapter 2 details the development and testing of a laboratory-scale ultra-stable frequency dissemination system using a 15 m long optical fiber achieving a residual phase noise, measured

in terms of fractional frequency stability of 2×10^{-18} at 1 second integration time. Our aim was to reliably transfer a stable optical signal within our laboratory while mitigating external noise through a digital phase-locked loop implemented on an FPGA based board. We also developed a compact, rack-mountable version for portable use. This work advances stable frequency transfer technology, with potential impacts across precision timekeeping.

Chapter 3 outlines the progress made in developing a compact and highly stable laser setup, a project initiated by the work of Alexandre Didier and Séverine Denis. It describes a laser system that is frequency-locked to an ultra-stable Fabry-Pérot cavity with a double tetrahedral-shaped spacer made from ULE (Ultra Low Expansion) glass, with a 25 mm optical length. The discussion extends from the cavity's design and the rationale behind its geometry to the optical and electronic approaches adopted for frequency stabilization, notably the digital implementation of the Pound-Drever-Hall (PDH) technique. Further sections delve into the cavity's characterization, addressing phase fluctuations and thermal expansion considerations, followed by an analysis of identified limitations and the strategies devised to overcome them, setting the stage for potential improvements in cavity performance.

Chapter 4 details the development of a transportable, ultra-stable laser system, based upon an updated version of the compact Fabry-Pérot cavity mentioned in Chapter 3. It outlines the novel features introduced and the key modifications to the system to enhance its stability and portability, with particular attention to the choice of INVAR for the new mount due to its thermal and mechanical advantages. The chapter also describes a redesigned compact power supply system for low-noise operation. The discussion covers the integration of optical and electronic components, highlighting the system's improved performance. It also highlights the limitations of the system and potential for future research improvements. A 25 m long optical fiber link setup for frequency dissemination from this ultra-stable laser system is also mentioned, aiming to connect ultra-stable lasers across different lab rooms.

Chapter 1

Introduction

1.1 Time and Frequency metrology

Time and frequency metrology is an essential scientific field that deals with accurately measuring time and frequency. Its significance has grown in recent years, as it finds applications in various areas such as telecommunications, global navigation systems, and scientific experiments that rely on precise timing.

A critical outcome of time and frequency metrology is the development of highly accurate frequency standards. These standards serve as primary references for measuring time and frequency with exceptional precision in a wide range of applications. The most notable frequency standards are atomic clocks, known for their remarkable accuracy and stability. They play a central role in advancing technologies and scientific research that depend on precise timekeeping.

State-of-the-art optical atomic clocks are advanced timekeeping instruments based on the precise transitions of neutral atoms or ions. These clocks have achieved remarkable systematic uncertainty levels of 10^{-18} and beyond [1–5]. They are crucial tools for various scientific and technological applications requiring utmost precision.

Concurrently, significant progress has been made in developing ultra-stable lasers using Fabry-Pérot cavities, demonstrating fractional frequency stability levels as low as 10^{-17} [6–10]. These lasers play a vital role in precise measurements and experimental setups that demand stable and reliable frequency sources.

However, it is important to note that primary frequency standards with the best accuracy are typically realized using atomic clocks such caesium atomic clocks. Optical atomic clocks are still under active research and development, and they have the potential to become an integral part of future frequency standards as their technology advances.

The integration of ultra-stable lasers and other precise timekeeping methods with atomic clocks has significantly advanced time and frequency metrology, enabling researchers and engineers to achieve unprecedented levels of frequency stability. These technologies hold the poten-

tial to drive further scientific exploration and facilitate the development of revolutionary applications that rely on precise and stable timing.

1.2 Ultra-stable lasers

1.2.1 Introduction

In the introductory part of Chapter 1, an overview will be given about the technique of laser frequency stabilization using a Fabry-Pérot cavity. The working and the properties of a Fabry-Pérot cavity will be explained in detail. Following that, an explanation of the principles behind laser frequency stabilization to a Fabry-Pérot cavity using the Pound-Drever-Hall method will be provided.

Furthermore, we will discuss the fundamental limits that affect the frequency stability of an ultra-stable laser. This will involve exploring both physical and technical factors that place restrictions on the achievable stability of the laser output frequency. These considerations will encompass factors such as thermal noise, quantum noise, and other intrinsic limitations influencing the overall frequency stability of the laser system.

Moreover, an outline of the tools and techniques employed to characterize the frequency stability of an ultra-stable laser will be presented. This will cover advanced measurement techniques and instruments utilized to evaluate the laser performance in terms of frequency stability. The methods will include determining phase noise, fractional frequency stability, thermal noise etc.

Finally, this section will conclude by spotlighting state-of-the-art ultra-stable lasers that are currently leading in scientific research and technological advancement. This will involve reviewing the latest developments in ultra-stable laser technology, encompassing innovative designs, novel methods, and breakthroughs that have achieved remarkable levels of frequency stability in modern laser systems.

1.2.2 Cavity stabilized lasers

In physics, particularly atomic physics, lasers are important tools in numerous experiments. Ensuring reproducibility and experiment quality hinges on the laser maintaining a stable, well-defined absolute frequency. In experiments where laser coherence is relevant, the short-term fluctuations around its mean frequency, known as the laser linewidth, become important. Controlling the laser linewidth is critical for experiments relying on temporal coherence, ensuring consistent conditions and meaningful results. In essence, managing the absolute frequency and linewidth of lasers is crucial for advancing our understanding of fundamental quantum phenomena in atomic physics. An ultra-stable laser is a very narrow linewidth laser whose frequency is stabilised to

the resonance frequency of an ultra-stable resonator which in my work was a Fabry-Pérot cavity. The fractional frequency fluctuations of an ultra-stable laser, stabilized to a Fabry-Pérot cavity, are fundamentally limited by the length fluctuations of the cavity and are given by the equation 1.1

$$\frac{\Delta L}{L} = -\frac{\Delta \nu}{\nu} \tag{1.1}$$

where, $\Delta L/L$ is the fractional length fluctuations of the Fabry-Pérot cavity and $\Delta\nu/\nu$ are the fractional frequency fluctuations of the laser. Length fluctuations in a Fabry-Pérot cavity can be caused by environmental noise including temperature fluctuations, vibrations, pressure fluctuations etc. which directly affect the frequency stability of the laser. So, in order to design an ultra-stable laser, one has to realise a system reducing these fluctuations.

1.2.3 Fabry-Pérot Cavity

A Fabry-Pérot cavity consists of a pair of mirrors that exhibit high reflectivity while also allowing partial transmission. These mirrors are placed at a fixed and predetermined distance denoted by L. To ensure structural stability and minimize the risk of unwanted deformations or misalignments that could negatively impact performance, these mirrors are carefully positioned on a spacer. This is achieved through optical contact. The schematic of a Fabry-Pérot cavity is shown in Fig.1.1.

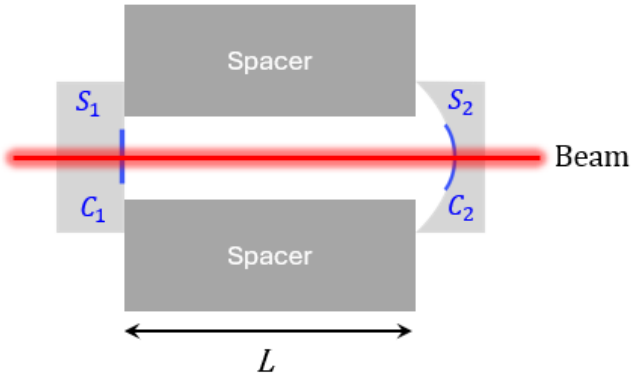

Figure 1.1: Schematic of a Fabry-Pérot cavity where S_1 and S_2 are the mirror substrates, L is the optical length of the cavity, C_1 and C_2 are the reflective coatings on the substrates.

The spacer, crucial for the Fabry-Pérot cavity functionality, can be crafted from various materials like glass, silicon, or sapphire. The choice of material depends on specific application requirements. Additionally, to enable reflectivity and reduce optical losses caused by scattering or absorption, thin films of amorphous or crystalline dielectric materials are applied as coatings onto the substrates. These coatings play a vital role in optimizing performance.

The Fabry-Pérot cavity mainly acts as an optical resonator, with resonance frequencies denoted by ν_C and given by the equation 1.2

$$\nu_c = \frac{mc}{2L} \tag{1.2}$$

where, c is the speed of light in vacuum and m is an integer indicating the order of resonance. The Fabry-Pérot cavity works on the phenomenon of multiple beam interference. From [11, 12], we know that when light of wavelength λ is incident on a Fabry-Pérot cavity, it undergoes multiple reflections between the mirrors. Intensity builds up inside the cavity until an equilibrium is reached; part of the light escapes through both mirrors. The reflected beam from the cavity is the coherent sum of the part of the incident beam that gets reflected off the first mirror without entering the cavity and a part of the standing wave inside the cavity that leaks through the first mirror. Both beams have the same frequency and amplitude near resonance but the phase of the two beams are strongly dependant on the frequency of the laser beam denoted by ν_L. If ν_L is in resonance with the cavity, these two beams will be 180° out of phase with each other resulting in destructive interference between them. This results in the complete disappearance of the reflected beam and all the light incident on the cavity will pass through. If ν_L is far from resonance with the cavity, there is no standing wave inside the cavity; the interference between all the round trip of light is zero. Therefore, the reflected beam is nearly the incident beam.

The Fabry-Pérot cavity provides multiple resonance modes that can be used to generate ultra-stable frequency references. The spacing between these resonant frequency modes is called the free spectral range (FSR) of the cavity. The FSR of a Fabry-Pérot cavity denoted by $\Delta\nu_{FSR}$ is given by the equation 1.3

$$\Delta\nu_{FSR} = \frac{c}{2L}. \tag{1.3}$$

The FSR of a Fabry-Pérot cavity generally lies in the radio frequency (RF) or microwave domain and is dependant on the length of the cavity (L) and the laser phase velocity that is the speed of light in case of a free space cavity. For an incident laser beam with an electric field (E) with a hypothesis of no losses (absorption), the incident and reflected electric fields are given by the equation 1.4

$$\begin{aligned} E_{inc} &= E_0 e^{(i\omega t)} \\ E_{ref} &= E_1 e^{(i\omega t)} \end{aligned} \tag{1.4}$$

where, E_0 and E_1 are the amplitude of the incident and reflected fields respectively and $\omega = 2\pi\nu_L$ is the angular frequency of the carrier. The electric field reflection coefficient ($\mathfrak{F}(\omega_e)$) for a cavity with symmetric mirrors of reflectivity (r) and transmitivity ($t = \sqrt{1-r^2}$) is given by the equation 1.5

$$\mathfrak{F}(\omega_e) = \frac{E_{ref}}{E_{inc}} = \frac{r(e^{i\omega_e/\Delta\nu_{FSR}} - 1)}{1 - r^2 e^{i\omega_e/\Delta\nu_{FSR}}}. \tag{1.5}$$

where, $\omega_e = \omega - \omega_c$ is the difference between the angular frequencies of the laser and the Fabry-Pérot cavity with $\omega_c = 2\pi\frac{mc}{2L}$ measured in radians per second. ω_e is also known as the angular frequency detuning measured in radians per second and can be expressed as $\delta\nu_{detuning}$ in Hz. The reflectivity (r) of the mirrors determines the amount of light that builds up inside the cavity. For highly reflective mirrors ($r > 0.99$), an average photon bounces many times between the mirrors before escaping. The number of round trips of a photon inside the cavity is proportional to the finesse denoted by $\mathcal{F}$. The finesse for a Fabry-Pérot cavity with highly reflective mirrors is given by the equation 1.6

$$\mathcal{F} = \frac{\pi\sqrt{r}}{1-r}. \tag{1.6}$$

The finesse plays an important role in characterizing the cavity capacity to enhance the interaction of light with its resonance mode. This parameter is derived by comparing the FSR of the cavity with the full width at half maximum (FWHM) of its resonant peak, often referred to as the linewidth. Mathematically, finesse is given by the equation 1.7

$$\mathcal{F} = \frac{\Delta\nu_{FSR}}{\delta\nu}, \tag{1.7}$$

where, $\delta\nu$ signifies the linewidth of the cavity. Finesse is directly connected to the number of oscillations the resonant mode experiences within the cavity before its energy dissipates. This relationship is inversely proportional to the losses within the cavity. Consequently, a high-finesse cavity corresponds to lower losses and the ability to sustain high-Q resonant modes characterized by narrow linewidths and exceptional spectral purity. This connection between linewidth and finesse is illustrated in Figure 1.2.

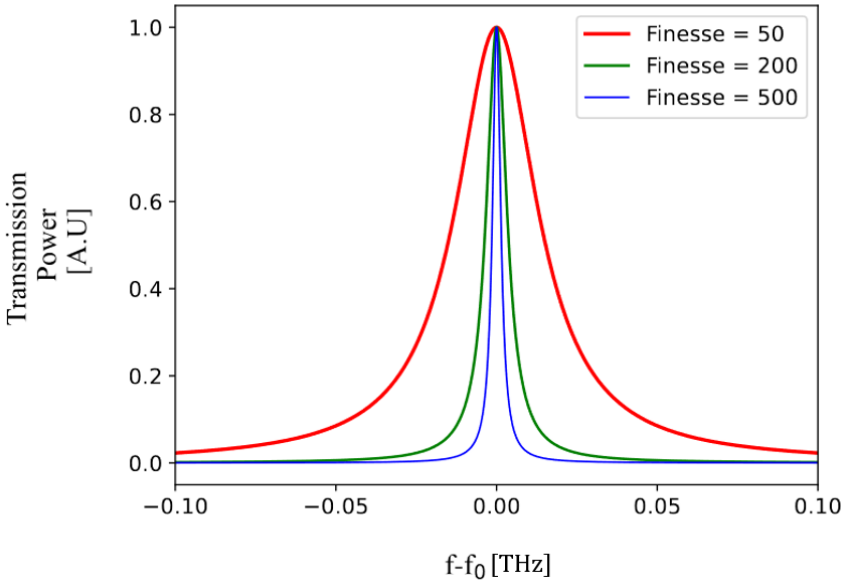

Figure 1.2: Transmission spectrum of a Fabry-Pérot cavity versus frequency for three different values of cavity finesse where f_0 is the resonance frequency of the cavity.

A higher finesse indicates a more efficient cavity, capable of confining light for extended durations and facilitating constructive interference. This leads to distinct, well-defined peaks in the Airy distribution of transmitted light, showcasing narrower linewidths (blue solid line). Conversely, a lower finesse results in broader linewidths (red and green solid lines), as the cavity efficiency in storing light decreases, and interference patterns become less well-defined. In essence, the quality of the cavity dictates the extent of constructive interference, consequently influencing the linewidth of resonant modes.

Various experimental methods are available for measuring finesse, dependent on the type of resonator and available equipment. The ringdown time method is the most commonly used approach, particularly for optical cavities with high finesse values. This technique involves switching off the input laser pulse and observing the decay of the resonant field using a high-speed photodetector. The finesse can be calculated based on the ringdown time and the cavity length.

The higher the finesse, the more time a photon spends inside the cavity. A high finesse cavity has a very narrow linewidth ($\delta\nu$), making it more sensitive to fluctuations in the frequency of the laser. To establish a link between the finesse ($\mathcal{F}$) and the linewidth ($\delta\nu$), we use the equation 1.8

$$\delta\nu = \frac{\Delta\nu_{FSR}}{\mathcal{F}}. \tag{1.8}$$

The intensity of the reflection, the transmission and the phase of the reflected beam near resonance for a cavity with a length of 100 mm and mirror reflectances of 99 $\%$, for a laser at 1.5 μm, is shown in Fig 1.3.

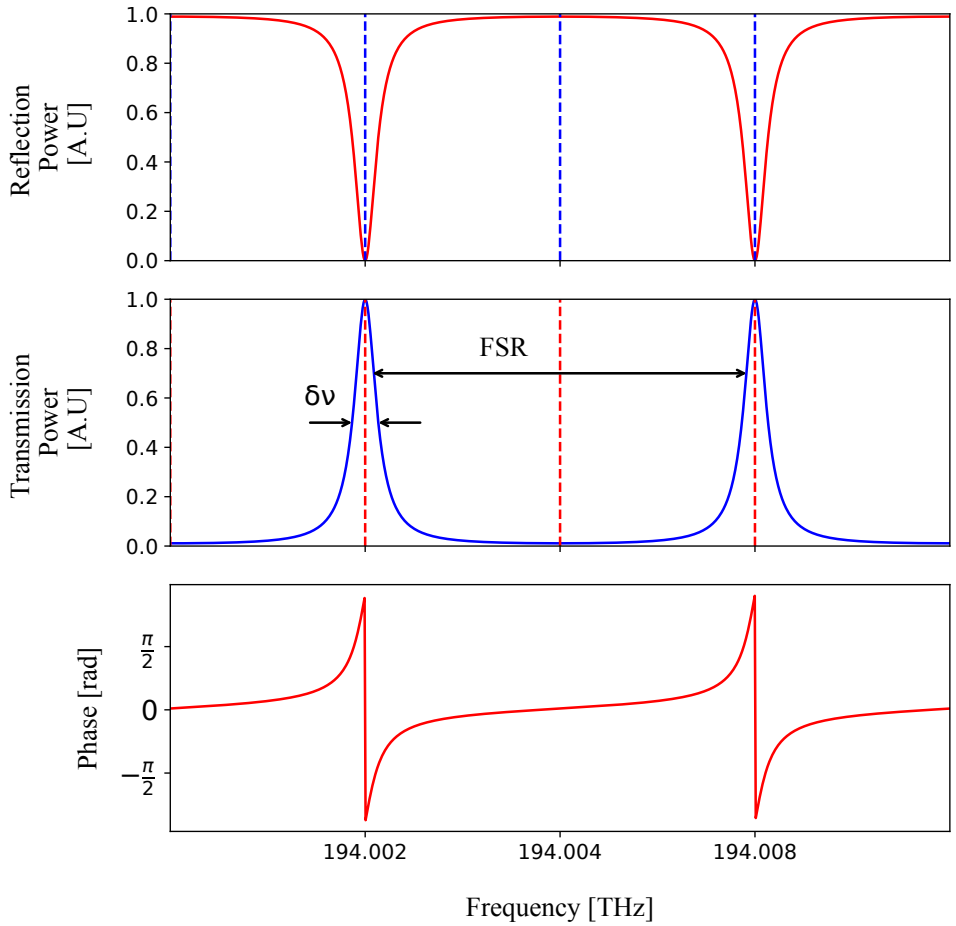

Figure 1.3: Red solid line: Intensity of cavity reflection over laser frequency; Blue solid line: Intensity of cavity transmission over laser frequency; Red solid line (plot 3): Phase of the reflected beam.

From Fig. 1.3, red and blue solid lines represent the intensity of reflection and transmission for a Fabry-Pérot cavity over frequency respectively and red solid line in the third plot represents the phase of the reflected signal. When the incoming light is in resonance, the phase of the reflected light from the Fabry-Pérot cavity displays a distinct change as the reflected intensity diminishes. When the light is detuned from resonance, the reflected light demonstrates a phase alteration with an opposing sign. This alteration in phase depends on the direction of the detuning.

1.2.4 Cavity Transmission Modes

Cavity transverse electromagnetic (TEM) modes are a type of resonant mode that can be sustained in a cavity bounded by two mirrors or reflective surfaces. These modes are characterized by the spatial distribution of the electric and magnetic fields within the cavity, and are fundamental to understanding the behavior of electromagnetic waves within optical cavities. Specifically, the TEM modes exhibit a uniform electric field and a magnetic field that is perpendicular to the direction of wave propagation.

The frequencies of the TEM modes are determined by the length of the cavity and the radius of curvature of the mirrors. These frequencies are separated by the free spectral range of the cavity. In the context of laser stabilization, the most commonly used TEM modes are the fundamental mode (TEM00) and higher-order modes such as TEM01 and TEM10. These modes have different spatial distributions and resonant frequencies, and can be selectively excited by varying the shape and alignment of the laser beam. However, the TEM00 mode is generally preferred due because it is easier to couple which leads to a more stable and precise laser output. According to [13], for a Gaussian standing wave inside a Fabry-Pérot cavity, the necessary conditions for the electric field to form a stable cavity mode are based on two conditions that are

1. the wavefront curvature condition.
2. the resonance condition.

The wavefront condition states that the curvature of the wavefront at each mirror of the cavity should match the effective radius of curvature (R) of the mirrors. Applying the wavefront condition for a Gaussian beam with wavelength λ incident on a cavity of length L, the waist (w_0) of the Gaussian beam that defines the distance from the beam centre where the electric field amplitude has fallen to $1/e$ of its maximum value is given by the equation 1.9

$$w_0 = \sqrt{\frac{\lambda}{\pi}L}\left[\frac{R}{L} - 1\right]^{1/4}. \tag{1.9}$$

State of the art Fabry-Pérot cavities can be configured with mirrors that have different radii of curvature, with the g parameter of each mirror in a general configuration given by

$$g_i = 1 - \frac{L}{R_i} \tag{1.10}$$

where, R_i is the radius of curvature of the i^{th} mirror. Stability in a Fabry-Pérot cavity occurs when the product of the g parameters for both mirrors satisfies the stability condition 1.11

$$0 < g_1 g_2 < 1 \tag{1.11}$$

The condition for resonance inside a Fabry-Pérot cavity states that the total round-trip phase shift of the light must be an integer multiple of 2π. Besides the fundamental mode, there are several other higher order modes in a cavity which are known as transverse electromagnetic modes (TEM_{mn}). The frequency of a Hermite-Gaussian mode in a Fabry-Pérot cavity is given by the equation 1.12

$$\nu_{mnq} = \Delta\nu_{FSR}\left[q + \frac{n+m+1}{\pi} arccos\left[\sqrt{g_1 g_2}\right]\right] \tag{1.12}$$

where, q is the principal mode number and m and n are the transverse mode numbers.

Frequency locking on a Fabry-Pérot cavity

The Pound-Drever-Hall (PDH) technique represents a laser frequency stabilization method that effectively synchronizes a laser frequency with the resonance frequency of a stable Fabry-Pérot cavity [14, 15]. This widely employed method owes its name to its pioneers, Robert Pound, Ronald Drever, and John Lewis Hall, and it plays a crucial role in stabilizing the frequencies of cutting-edge ultra-stable lasers.

In the PDH technique, a laser beam with frequency ν_L is directed into a Fabry-Pérot cavity with resonance frequency ν_c as described previously. The reflected signal from the cavity contains valuable information about both the cavity resonance and the laser frequency. A photodetector is employed to detect this reflected signal. Photodetectors have a limited measurement bandwidth, making it impossible to directly measure optical frequencies. However, the phase shift caused by changes in optical frequencies can be measured. In the PDH technique, the key parameter of interest is the phase shift of the reflected beam from the Fabry-Pérot cavity.

To accomplish this, an Electro Optical Modulator (EOM) is used to introduce phase modulation to the incident beam at a specific modulation frequency Ω. The modulation depth (β) of the EOM is carefully set to ensure that 50 $\%$ of the power is in the carrier, while the remaining 50 $\%$ is in the first-order sidebands.

It is crucial for the modulation frequency Ω to be higher than the linewidth of the cavity. This way, when the phase-modulated carrier beam is directed into the cavity, only the carrier frequency couples with the cavity, while the sidebands get reflected. These sidebands, operating at the frequency Ω, interfere with the reflected beam from the cavity, enabling the phase of the reflected beam to be detected through a beatnote at Ω.

Additionally, please note that the PDH technique capitalizes on the symmetric behavior of the Fabry-Pérot cavity reflection coefficient near resonance, as documented in [12]. Specifically, when the laser frequency is above resonance, the reflection coefficient derivative is positive, resulting in the reflected beam intensity varying in phase with frequency changes. Conversely, when the laser frequency is below resonance, the derivative becomes negative, leading to the intensity behaving out of phase with frequency variations. At the exact resonance frequency, the reflected intensity is cancelled.

The detected signal is then filtered and demodulated by mixing it with a local oscillator signal in a mixer. The output of the mixer is directly proportional to the difference in frequency between the laser and the cavity, which is commonly referred to as the detuning frequency $\delta\nu_{detuning}$. This detuning frequency is subsequently used to generate an error signal, allowing for precise frequency stabilization. The implementation of the Pound-Drever-Hall (PDH) technique involves following the scheme depicted in Figure 1.4.

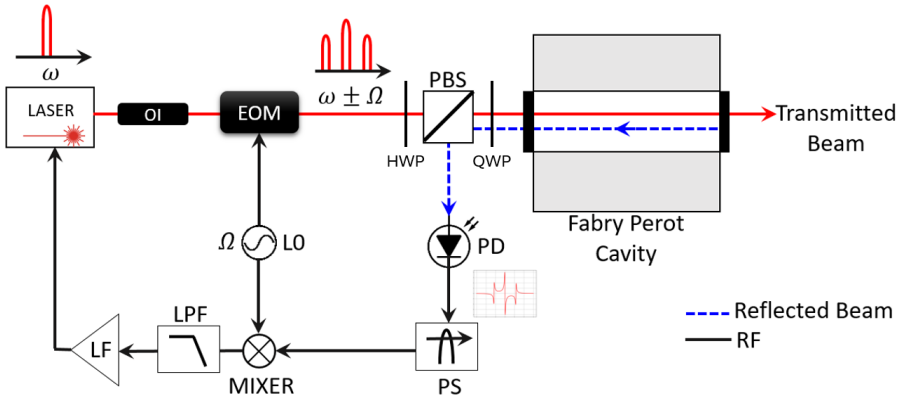

Figure 1.4: Scheme of PDH frequency locking technique where ν_L is the frequency of the laser, ν_C is the frequency of the Fabry-Pérot cavity, OI is optical isolator, EOM is electro optical modulator, LO is local oscillator, LF is loop filter, PD is photodiode, PS is phase shifter, LPF is low pass filter, PBS is polarised beam splitter.

By carefully observing the intensity of the reflected beam versus laser frequency near resonance, the PDH technique generates an error signal, which is the derivative of the reflection coefficient with respect to the detuning frequency. This error signal is then used in a feedback loop to tune the laser frequency. Leveraging this feedback, the system adjusts the laser frequency to match the cavity resonance, effectively stabilizing the laser output. The intensity of the reflected beam is quantified by equation 1.13

$$I(R) = |E_{ref}|^2 = \mathfrak{F}^2 |E_{inc}|^2, \tag{1.13}$$

where $I(R)$ is the intensity of the reflected beam, E_{ref} is the reflected electric field, E_{inc} is the incident electric field, and $\mathfrak{F}$ is the cavity reflection coefficient and is given by the equation 1.14

$$\mathfrak{F} = \frac{E_{ref}}{E_{inc}}. \tag{1.14}$$

Mathematically, the incident electric field of phase-modulated light on the cavity is given by equation 1.15

$$\begin{aligned} E_{inc} &= E_0 e^{i(\omega t + \beta sin(\Omega t))} \\ &\approx E_0 \left[J_0(\beta) e^{i\omega t} + J_1(\beta) e^{i(\omega+\Omega)t} - J_1(\beta) e^{i(\omega-\Omega)t} \right]. \end{aligned} \tag{1.15}$$

where, $J_i(i = 0, 1)$ is the i-th order Bessel function. It comprises the carrier wave at a frequency ω and the two sidebands at frequencies $\omega \pm \Omega$ due to the Electro Optical Modulator (EOM) phase modulation. The reflected electric field, E_{ref}, is obtained by multiplying E_{inc} with the reflection coefficients, $\mathfrak{F}(\omega)$, as shown in equation 1.16

$$E_{ref} = E_0 \left[\mathfrak{F}(\omega_e) J_0(\beta) e^{i\omega t} + \mathfrak{F}(\omega_e + \Omega) J_1(\beta) e^{i(\omega+\Omega)t} - \mathfrak{F}(\omega_e - \Omega) J_1(\beta) e^{i(\omega-\Omega)t} \right]. \tag{1.16}$$

To indirectly measure the electric field, the power of the reflected signal on the photodiode, denoted as $I(R)$, is analyzed. This intensity is given by Equation 1.17

$$\begin{aligned} I(R) &= |E_{ref}|^2 \\ &= P_c|\mathfrak{F}(\omega_e)|^2 + P_s|\mathfrak{F}(\omega_e+\Omega)|^2 + P_s|\mathfrak{F}(\omega_e-\Omega)|^2 \\ &+ 2\sqrt{P_cP_s}Re[\mathfrak{F}(\omega_e)\mathfrak{F}^*(\omega_e+\Omega) - \mathfrak{F}^*(\omega_e)\mathfrak{F}(\omega_e-\Omega)] \cdot \cos(\Omega t) \\ &+ 2\sqrt{P_cP_s}Im[\mathfrak{F}(\omega_e)\mathfrak{F}^*(\omega_e+\Omega) - \mathfrak{F}^*(\omega_e)\mathfrak{F}(\omega_e-\Omega)] \cdot \sin(\Omega t)) \\ &+ O[2\Omega] \end{aligned} \tag{1.17}$$

where,

$$\begin{aligned} P_c &= J_0^2(\beta) P_0 \\ P_s &= J_1^2(\beta) P_0 \end{aligned} \tag{1.18}$$

It consists of various frequency components, including the carrier frequency (ω) producing a DC signal, the first-order sidebands oscillating at the modulation frequency (Ω), and higher-order harmonics (2Ω). The modulation depth (β) is chosen such that $P_c + 2P_s \approx P_0$, ensuring the discriminant D of the error signal is maximised.This optimization enhances the system's sensitivity to frequency deviations. Further details on how the modulation depth influences the error signal are provided after equation 1.20.

A frequency mixer is utilized to isolate the phase information carried by the $\sin(\Omega t)$ and $\cos(\Omega t)$ components. By mixing the photodiode (RF) signal with a local oscillator at the modulation frequency (Ω) and passing it through a low-pass filter, the Pound-Drever-Hall error signal (ϵ) is obtained which can be expressed as given in equation 1.19

$$\epsilon = 2\sqrt{P_cP_s}Im[\mathfrak{F}(\omega_e)\mathfrak{F}^*(\omega_e+\Omega) - \mathfrak{F}^*(\omega_e)\mathfrak{F}(\omega_e-\Omega)]. \tag{1.19}$$

When the modulation frequency is sufficiently high, the sidebands do not enter the cavity, and the error signal is approximately proportional to $Im[\mathfrak{F}(\omega)]$. When the frequency of the laser is nearby the frequency of the cavity, ϵ an be approximated as 1.20 [12]

$$\begin{aligned} \epsilon &= -\frac{4}{\pi}\sqrt{P_cP_s}\frac{\omega_e}{\delta\nu} = D\delta\nu_{detuning} \\ D &= -8\frac{\sqrt{P_cP_s}}{\delta\nu} = -16\frac{\mathcal{F}L}{c}\sqrt{P_cP_s} \end{aligned} \tag{1.20}$$

where, $\delta\nu$ is the linewidth of the laser, ω_e is the angular frequency detuning, $\delta\nu_{detuning}$ is the fre-

quency detuning and D is the frequency discriminant that is the slope of the error signal. It reflects the system's sensitivity to small frequency deviations from the desired lock point. A higher value of D indicates a steeper slope, which enhances the precision of laser frequency stabilization by increasing the feedback response to any frequency shifts. A steeper slope is particularly beneficial because it reduces the system's vulnerability to various noise sources, such as electronic offsets or drifts in the control electronics. In essence, a large D improves the robustness of the frequency lock by ensuring that corrections are applied rapidly and effectively over a wide range of operational conditions. Moreover, the discriminant can be adjusted by modifying the modulation depth or amplitude of the modulation sidebands in the stabilization process, as these factors directly affect the shape and steepness of the error signal. This adjustment further enhances the system's resolution and its ability to maintain tight control over the laser frequency.

1.2.5 Ultra-stable laser characterization tools

In this subsection, I will give a short description about the tools we use to characterise the frequency noise and stability in oscillators, atomic clocks and ultra stable lasers. Please note that I will give a short summary of the tools. Detailed explanation can be found in several books and journal articles available online. To describe the tools I mostly used the books by [16] and [17].

Power Spectral Density (PSD)

Power Spectral Density (PSD) is a measure of the distribution of power within a signal as a function of frequency. The PSD of a signal is defined as the power per unit frequency, and it describes how the power of the signal is distributed across different frequency components. As per Wiener–Khinchin theorem, the PSD is the Fourier transform of the autocorrelation function ($R(t)$) of a signal, and it is typically expressed in units of power per hertz. The power spectrum $S(\omega)$ of a random process $x(t)$, specifically known as the two-sided power spectrum denoted by $S^{II}(\omega)$ is given by the equation 1.21

$$S^{II}(\omega) = \int_{-\infty}^{+\infty} R(t) e^{j\omega t} dt. \tag{1.21}$$

The autocorrelation function quantifies the similarity between a signal and itself at different points in time. PSD provides information on how the power of a signal is distributed among different frequencies.

In the frequency domain, the phase noise in an oscillator is mainly characterized by the one sided PSD of the random phase fluctuations of $\varphi(t)$ as a function of the Fourier frequency f from the carrier in a measurement bandwidth of 1 Hz [18]. One-sided PSD is a variant of the PSD that describes the distribution of power in a signal as a function of positive frequencies only. In contrast, the standard two-sided PSD describes the distribution of power as a function of both positive

and negative frequencies. Please note that, positive and negative frequencies are mathematical concepts in signal processing where positive frequencies represent counterclockwise oscillations and negative frequencies represent clockwise oscillations in the complex plane. While real signals contain both, negative frequencies do not correspond to physical phenomena but are necessary for fully describing real-world signals in the frequency domain.

The PSD of phase fluctuations, expressed as $S_\varphi(f)$ measures the phase noise relative to the carrier frequency. It provides information about the amount of phase noise power that is present at each frequency offset from the carrier frequency. The unit of $S_\varphi(f)$ is rad^2/Hz.

Another term used to characterize the phase noise of a signal is denoted by $\mathscr{L}(f)$, which is basically the one-sided PSD of the phase fluctuations as a function of frequency f and is given by the equation 1.22

$$\mathscr{L}(f) = \frac{1}{2} S_\varphi(f). \tag{1.22}$$

In practice, $\mathscr{L}(f)$ is expressed in units of dBc/Hz where dBc refers to the power relative to the carrier. It describes the power level of the phase noise relative to the carrier power in a 1 Hz bandwidth at each frequency offset from the carrier. Therefore the relation between $S_\varphi(f)$ and $\mathscr{L}(f)$ can be expressed by the equation 1.23

$$\begin{aligned} 10\log_{10}[\mathscr{L}(f)] &= 10\log_{10}\left[\frac{1}{2}S_\varphi(f)\right], \\ &= 10\log_{10}\left[S_\varphi(f)\right] - 3 \text{ dB}. \end{aligned} \tag{1.23}$$

$S_\varphi(f)$ can be expressed in terms of the power law [19] which states that the PSD for phase fluctuations is a sum of the integer power of the Fourier frequency. $S_\varphi(f)$ in terms of the power law is given by the equation 1.24

$$S_\varphi(f) = \sum_{i=0}^{-4} b_i f^i, \tag{1.24}$$

where, b_i is the amplitude associated with each power of f. The various types of noise associated with $S_\varphi(f)$ is shown in Fig. 1.5.

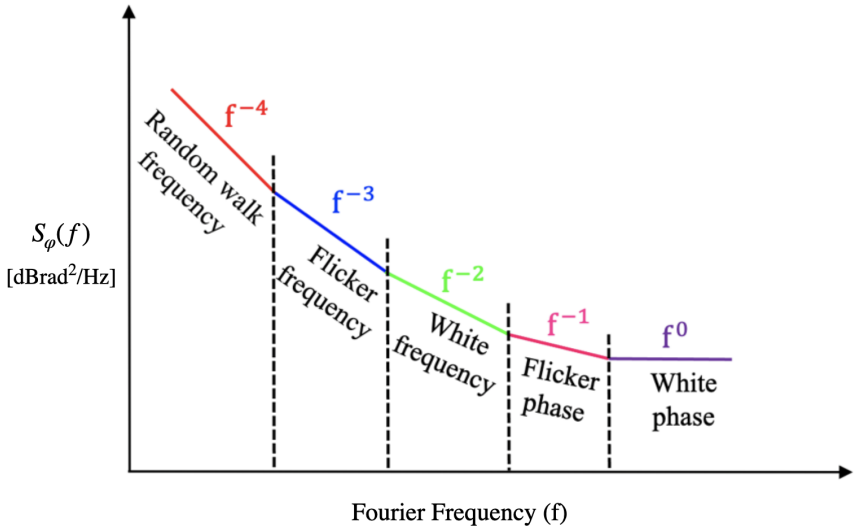

Figure 1.5: Types of noise associated with $S\varphi(f)$.

PSD of phase fluctuations can be written in terms of PSD of phase-time fluctuations ($x(t)$) denoted by $S_x(f)$ and given by the equation 1.25

$$S_x(f) = \frac{1}{(2\pi\nu_0)^2} S_\varphi(f). \tag{1.25}$$

The unit for $S_x(f)$ is s^2/Hz. Phase noise can also be converted into frequency noise. PSD of frequency fluctuations which characterizes the power of frequency deviations from a reference frequency can be expressed in terms of $S_\varphi(f)$ using the equation 1.26

$$S_{\Delta\nu}(f) = f^2 S_\varphi(f). \tag{1.26}$$

$S_{\Delta\nu}(f)$ is measured in Hz^2/Hz. On the other hand, the PSD of fractional frequency fluctuations $S_y(f)$ characterizes the power of the fractional deviation of the instantaneous frequency from the nominal or carrier frequency. It tells us how much the frequency of a signal varies relative to its nominal or carrier frequency over time. $S_y(f)$ is given by the equation 1.27

$$S_y(f) = \frac{1}{\nu_0^2} S_{\Delta\nu}(f) = \frac{f^2}{\nu_0^2} S_\varphi(f). \tag{1.27}$$

where, ν_0 is the carrier frequency. The unit of $S_y(f)$ is Hz^{-1}

The PSD of fractional frequency fluctuations can be represented as a sum of terms, where each term is characterized by an integer power of the Fourier frequency, denoted as f. These integer powers, ranging from -2 to +2, correspond to different types of noise. Thus, the PSD

$S_y(f)$ can be expressed using the equation 1.28

$$S_y(f) = \sum_{i=-2}^{2} h_i f^i \tag{1.28}$$

where h_i represents the amplitude associated with each power of f. This power-law expression is commonly used to estimate the spectral densities of high stability frequency standards [19]. It provides valuable insights into the different noise contributions and their impact on the overall frequency stability. Fig. 1.6 illustrates the different types of noise based on the slope of f.

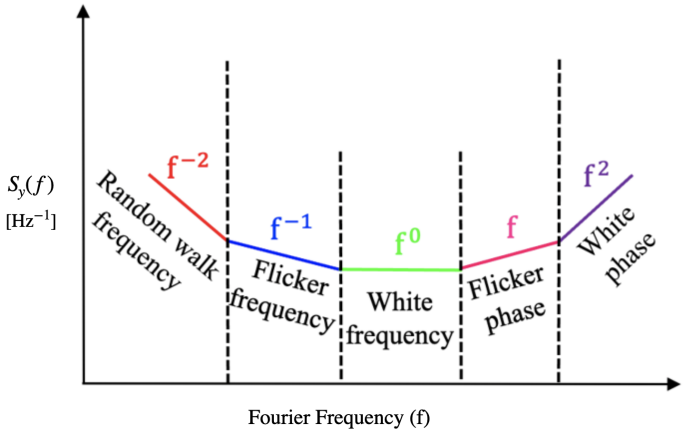

Figure 1.6: Types of noise associated with $S_y(f)$.

Allan Variance

Allan variance (AVAR) also called 2-sample variance is an important tool used by metrologists to estimate the frequency instability of oscillators and clocks in the time domain. One can use standard variance to measure the frequency fluctuations but the problem with this estimator is that, standard variance is divergent for some types of noise mostly present in clocks such as random walk frequency noise and linear frequency drift. Therefore we use AVAR that converges for all types of noises shown in Fig. 1.6 for time domain characterisation of fractional frequency instability. For a finite dataset containing N samples, AVAR is defined mathematically by the equation 1.29

$$\sigma_y^2(\tau) = \frac{1}{2}\langle(\bar{y}_{i+1} - \bar{y}_i)^2\rangle = \frac{1}{2(N-1)} \sum_{i=1}^{N-1} (\bar{y}_{i+1} - \bar{y}_i)^2 \tag{1.29}$$

where, $\bar{y}_i$ are the discrete fractional frequency averages, the brackets ($\langle\rangle$) denote an infinite time average and the term 2 at the denominator is the normalization factor to classical variance for a classical white frequency noise [20]. The fractional frequency average is calculated by taking the derivative of the phase x_i and is given by the equation 1.30

$$\bar{y}_i = \frac{1}{\tau}(x_{(i+1)} - x_i). \tag{1.30}$$

Generally, Allan deviation (ADEV) is used which is defined as the square root of AVAR and is given by the equation 1.31

$$\sigma_y(\tau) = \sqrt{\sigma_y^2(\tau)}. \tag{1.31}$$

The overlapping Allan variance (OAVAR), introduced by [21], makes better use of the available data by incorporating overlapping samples. OAVAR is computed by dividing the time domain data into overlapping segments, and then calculating the variance of the frequency fluctuations within each segment. OAVAR for an N sample frequency data is defined by the equation 1.32

$$\sigma_y^2(\tau) = \frac{1}{2n^2(N-2n+1)} \sum_{j=1}^{N-2n+1} \left\{ \sum_{i=j}^{j+n-1} (\bar{y}_{i+1} - \bar{y}_i)^2 \right\}. \tag{1.32}$$

Using OAVAR helps in getting a better estimate of the stability of an oscillator but the computation time is more for OAVAR when compared to AVAR. So, both AVAR and OAVAR can be used to estimate the stability of an oscillator. However one drawback of AVAR and OAVAR is that, none of them can distinguish between white and flicker phase noises because the slope of $\sigma_y^2(\tau)$ versus τ is the same (τ^{-1}) . As a result, to distinguish between these two types of noises, the modified Allan variance (MVAR) was developed and is defined by the equation 1.33

$$mod\ \sigma_y^2(\tau) = \frac{1}{2n^4(N-3n+2)} \sum_{j=1}^{N-3n+2} \left\{ \sum_{i=j}^{j+n-1} \left(\sum_{k=i}^{i+n-1} (\bar{y}_{i+1} - \bar{y}_i)^2 \right) \right\}. \tag{1.33}$$

Comparing equations 1.33 and 1.32, we can see that an extra averaging is used for MVAR. Using MVAR, one can easily compute the fractional frequency instability of an oscillator that is mostly affected by white phase noise.

Relationship between PSD and Allan Variance

If the PSD of fractional frequency fluctuations ($S_y(f)$) is known, it can be easily converted to Allan Variance ($\sigma_y^2(\tau)$) and modified Allan variance ($mod.\ \sigma_y^2(\tau)$). In order to establish a relationship between the PSD of fractional frequency fluctuations ($S_y(f)$) and AVAR, we use the equation 1.34 [22]

$$\sigma_y^2(\tau) = 2 \int_0^\infty S_y(f) \frac{\sin^4(\pi f \tau)}{(\pi f \tau)^2} df \tag{1.34}$$

In the given context, τ represents a time interval, which is determined by the integer n and the fixed sampling time τ_0. The fixed sampling time τ_0 denotes the time interval between successive frequency measurements or data points in the time domain analysis. However, converting $\sigma_y^2(\tau)$

to $S_y(f)$ is not feasible due to the loss of certain information during the conversion process. Table 1.1 provided below contains the formulae for converting PSD to AVAR and MVAR for different types of noise, as illustrated in Fig. 1.5 and Fig. 1.6.

Types of Noise	$S_\varphi(f)$	$S_y(f)$	$S_\varphi(f) \leftrightarrow S_y(f)$	$\sigma_y^2(\tau)$	$mod.\sigma_y^2(\tau)$
White PN	b_0	$h_2 f^2$	$h_2 = \frac{b_0}{\nu_0^2}$	$0.0760\ f_H h_2 \tau^{-2}$	$0.0380\ h_2 \tau^{-3}$
Flicker PN	$b_{-1} f^{-1}$	$h_1 f$	$h_1 = \frac{b_{-1}}{\nu_0^2}$	$\frac{1.038+3ln(2\pi f_H \tau)}{4\pi^2} h_1 \tau^{-2}$	$0.0855\ h_1 \tau^{-2}$
White FN	$b_{-2} f^{-2}$	h_0	$h_0 = \frac{b_{-2}}{\nu_0^2}$	$\frac{1}{2} h_0 \tau^{-1}$	$\frac{1}{4} h_0 \tau^{-1}$
Flicker FN	$b_{-3} f^{-3}$	$h_{-1} f^{-1}$	$h_{-1} = \frac{b_{-3}}{\nu_0^2}$	$1.3863\ h_{-1}$	$0.9352\ h_{-1}$
Random walk FN	$b_{-4} f^{-4}$	$h_{-2} f^{-2}$	$h_{-2} = \frac{b_{-4}}{\nu_0^2}$	$6.5797\ 2h_{-2}\tau$	$5.4283\ 2h_{-2}\tau$

Table 1.1: Relationship between PSD,AVAR and MVAR [23][24] for different types of noise; f_H denotes the high frequency cutoff of the measurement bandwidth.

1.2.6 Limitations of ultra-stable lasers

Thermal noise of cavity

The fundamental limit affecting the fractional frequency instability in optical cavities is thermally induced noise also called thermal noise [25]. There are various types of thermal noise affecting an optical resonator [26] which include:

1. Spacer, Substrate and coating Brownian noise.
2. Substrate and coating thermoelastic noise.
3. Coating thermorefractive noise.
4. Coating photothermoelastic and photothermorefractive noises.
5. Substrate and coating Stefan-Boltzmann thermoradiation noises.

In my thesis, I will just focus on the thermal noise induced by Brownian motion as this type of noise is dominant over other thermal noises mentioned in [26]. This Brownian motion directly affects the fractional length fluctuations in an optical cavity which affects its frequency instability.

Generally, Brownian thermal noise is calculated using the Fluctuation Dissipation Theorem (FDT) [27, 28]. In order to estimate the thermal noise of a Fabry-Pérot cavity, I used the equations introduced by [25] and [29], derived using the FDT. They separately calculate the thermal noise of each part of the cavity (spacer, coating and substrates). To facilitate the complex calculations, they considered that the thermal noise due to each part does not influence the other part. Finally, to calculate the thermal noise of the whole system, they added the contributions of each element. The equation determining the total noise spectral density of the cavity with length L is determined by equation 1.35

$$S_x^{TN}(f) = S_x^{spac.}(f) + 2S_x^{sub.}(f) + 2S_x^{coat.}(f) \tag{1.35}$$

where, $S_x^{TN}(f)$ is the total PSD of length fluctuations due to the thermal noise, $S_x^{spac.}$, $S_x^{sub.}$ and $S_x^{coat.}$ are the displacement noise due to the spacer, substrates and reflective coatings respectively. The most significant parameters required for the calculation of thermal noise are the mechanical quality factor Q and the Young's modulus E of the material under study. The noise due to the two substrates $S_x^{sub.}$ is given by the equation 1.36

$$S_x^{sub.}(f) = \frac{4k_BT}{\pi f}\frac{1-\sigma^2}{2\sqrt{\pi}Ew}\phi_{sb} \tag{1.36}$$

where,

- k_B is the Boltzmann constant,
- T is the temperature of the substrate,
- σ is the Poisson's ratio for the material of the substrate,
- w is the laser beam radius,
- $\phi_{sb} = 1/Q_{sb}$ is the loss angle of the substrate.

The noise of the reflective coatings $S_x^{coat.}(f)$ is directly dependant on the noise of the substrate and is given by the equation 1.37

$$S_x^{coat.}(f) = S_x^{sub.}(f)\frac{2}{\sqrt{\pi}}\frac{1-2\sigma}{1-\sigma}\frac{\phi_{ct}}{\phi_{sb}}\frac{d_{ct}}{w} \tag{1.37}$$

where,

- d_{ct} is the thickness of the layer of the reflective coatings,
- $\phi_{ct} = 1/Q_{ct}$ is the loss angle of the coatings.

To calculate the noise of the spacer $S_x^{spacer}(f)$, we consider the spacer to be a cylinder of length L, radius R_{sp} and central bore radius r_{sp} and we use the equation 1.38

$$S_x^{spac.}(f) = \frac{4k_BT}{\pi f}\frac{L}{2\pi E(R_{sp}^2 - r_{sp}^2)}\phi_{sp} \tag{1.38}$$

where,

- $\phi_{sp} = 1/Q_{sp}$ is the loss angle of the spacer.

We can convert $S_x^{TN}(f)$ into PSD of phase noise $S_\varphi(f)$. In order to convert $S_x^{TN}(f)$ to $S_\varphi(f)$, we use equations 1.39 and 1.40

$$S_y(f) = \frac{S_x^{TN}(f)}{L^2} \tag{1.39}$$

$$S_\varphi(f) = S_y(f) * \frac{\nu_L^2}{f^2} \tag{1.40}$$

PSD of Thermal noise $S_x(f)$ has a $1/f$ slope which indicates that it is flicker frequency noise. So, we can convert this frequency instability into time domain fluctuations characterized by the Allan-deviation $\sigma(y)$ of the fractional frequency fluctuations using the equations mentioned in Table 1.6. From the equations 1.37, 1.38 and 1.36, it is quite evident that the temperature T, laser beam radius w, thickness of the reflective coatings d, the loss angle ϕ material properties (E, σ) and the length of the cavity (L) directly affect the thermal noise of the cavity. Higher temperatures, smaller laser beam radii, thicker coatings, higher loss angles and specific material properties contribute to increased thermal noise levels. Controlling and optimizing these parameters is essential to minimize thermal noise and enhance the performance and stability of Fabry-Pérot cavity-based systems.

Thermal expansion

The spacing (L) between the two mirrors in a Fabry-Pérot cavity is sensitive to temperature fluctuations, which in turn affects the resonance frequency of the cavity as described by Equation 1.1. This dependency on temperature fluctuations is dictated by the coefficient of thermal expansion (CTE) of the cavity material, denoted by α. To mitigate this dependency, materials with low or negligible CTE are used for the Fabry-Pérot cavity spacer and mirrors. Common materials used for cavities operated at room temperature include zerodur [30][31], ultra low expansion (ULE) glass [32], or a combination of ULE spacer with fused silica (FS) substrates [33].

Both ULE and Zerodur are used because their CTE vanishes to the first order at a temperature known as the inversion temperature (T_0), which is near room temperature [34]. However, ULE is generally preferred over Zerodur due to its smaller and more stable drift rate. In contrast, the drift rate of Zerodur is strongly influenced by prior tempering steps, making it less predictable and often larger than that of ULE. However, an all ULE cavity can be limited by thermal noise primarily from the ULE mirror substrates [25]. To reduce the thermal noise floor, fused silica mirror substrates have been used, resulting in a factor of 2 improvement in cavity performance compared to an all ULE cavity, as demonstrated by Legero *et al.* [35] and Millo *et al.* [33].

However, the use of fused silica mirrors introduces a disadvantage in the form of a larger CTE (5×10^{-7}/K) compared to ULE, which lowers the CTE inversion point to below $0^{\circ}C$ instead of $10^{\circ}C$ to $20^{\circ}C$. To address this issue, techniques such as optically contacting ULE rings to the mirrors or using special mirror configurations have been employed [25]. Alternatively, some cavities are based on high Q materials, such as Silicon, which exhibits vanishing CTE at two different temperatures of 123 K and 17 K [36].

In my thesis, I will be utilizing a Fabry-Pérot cavity with a ULE spacer and fused silica mirrors. The fractional change in spacer length ($\frac{dL}{L}$) due to thermal expansion can be described by the equation 1.41

$$\frac{dL}{L} = \alpha_{ULE}(T)dT \tag{1.41}$$

where $\alpha_{ULE}(T)$ represents the temperature-dependent coefficient of thermal expansion of ULE. Around the inversion temperature (T_0), α_{ULE} can be approximated by the equation 1.42

$$\alpha_{ULE} = a(T - T_0) + b(T - T_0)^2 \tag{1.42}$$

with a, being the linear temperature coefficient and b, being the quadratic coefficient. a lies in the range of $1.8 \times 10^{-9}/K^2$ and b in the range of $-10 \times 10^{-12}/K^3$ [35]. Hence, b can be considered as negligible. Therefore, equation 1.41 can be expressed as 1.43

$$\frac{\Delta L}{L} = \frac{a}{2}(T - T_0)^2. \tag{1.43}$$

Legero *et al.* [35] considered $a = 2.4 \times 10^{-9}/K^2$ and $b = 0$ for their FEM simulations for a cavity made of ULE spacer and fused silica mirrors. They also considered the CTE of fused silica to be constant with a value of 500×10^{-9}/K.

Acceleration & Vibration sensitivities

Seismic and acoustic perturbations can impose significant limitations on the frequency stability of a Fabry-Pérot cavity mostly in the lower frequency (kHz) range, as they affect the precise length between the cavity mirrors. Referred to as vibration noise or acceleration noise (S_a), these perturbations deform the cavity and introduce frequency noise to the laser. Studies by Young *et al.* [34] have reported that an acceleration of 1 m/s^2 can lead to a fractional length change of 2×10^{-10} for a cylinder-shaped resonator, underscoring the considerable impact of acceleration noise on the Fabry-Pérot cavity stability in high-precision applications.

A quantitative relationship between the fractional frequency noise (S_y) and acceleration noise (S_a) is commonly expressed using the equation 1.44

$$S_y(f) = \sum_{i=x,y,z} k_i^2 S_{a_i}, \tag{1.44}$$

where $k_{x,y,z}$ represent the acceleration sensitivity coefficients, with x, y, and z denoting the transverse, cavity optical axis, and vertical directions, respectively. This equation highlights the influence of the square of the acceleration sensitivity coefficients for each direction on the fractional frequency noise, underscoring the importance of understanding acceleration noise characteristics in different directions for accurate frequency stability analysis.

To mitigate the effects of acceleration noise, a robust vibration isolation system is crucial. Specialized isolation techniques, such as active or passive vibration isolators, are employed to minimize the transfer of external vibrations to the Fabry-Pérot cavity. Moreover, optimized cavity designs that reduce susceptibility to vibrations along the optical axis are implemented. Advanced Fabry-Pérot cavities are carefully engineered to suppress deformations induced by acceleration

noise, thereby mitigating the limitations posed by vibration noise on the frequency stability in precision measurement and high-performance laser systems.

In conclusion, seismic and acoustic perturbations, manifested as acceleration noise, represent one of the technical limitations to the frequency stability of Fabry-Pérot cavities in the kHz range. Understanding acceleration noise characteristics and implementing effective vibration isolation measures and optimized cavity designs is critical for mitigating these limitations and achieving superior frequency stability in advanced laser systems and precision measurement applications.

Shot noise and Electronic noise

The PDH technique [12] is commonly used to stabilize the frequency of a laser, as discussed in Section 1.2.4. It generates an error signal (ϵ) with a slope denoted by D, known as the frequency discriminant, which exhibits a linear behavior near the cavity resonance regime. D is directly proportional to the finesse of the cavity and significantly influences the laser performance.

The stability of the laser frequency is affected by two main noise sources: shot noise and electronic noise. Shot noise, also known as quantum noise, arises due to the random nature of photon detection by the photodiode in the PDH technique. It results from the discrete nature of photons and their unpredictable arrival times at the photodetector, causing an irregular flow of photons and the generation of shot noise.

In the PDH technique, shot noise contributes to the noise on the error signal from optics (S_ϵ) used for frequency stabilization, setting a fundamental limit on the achievable signal-to-noise ratio on the photodetector [37–39]. It is challenging to distinguish shot noise from other types of noise, such as frequency noise, as they are combined in the detected signal.

Shot noise is equally split between AM and PM noise. Amplitude Modulation (AM) noise signifies variations in signal amplitude, leading to fluctuations in the signal strength over time. Conversely, Phase Modulation (PM) noise entails changes in the phase of a signal, resulting in random alterations to the timing of the signal cycles. While the PM shot noise contribution is corrected by the PDH, the AM contribution translates into frequency noise, making it a limiting factor in achieving the desired frequency stability of a laser. The shot noise generated by the photodiode contributes to the overall noise on the error signal and affects the frequency stability of the laser.

On the other hand, electronic noise from various sources like amplifiers, cables, and other components in the PDH technique detection and control circuitry also affects the laser frequency stability. Electronic noise contributes to the voltage noise of the error signal (S_V). For laser frequencies close to the resonance frequency of the cavity, a relation can be established between

shot noise, electronic noise, and the stability of the laser frequency given by the equations 1.45

$$S_{\delta\nu} = \frac{1}{D^2} S_\epsilon = \frac{1}{\eta^2 R^2 D^2} S_V. \tag{1.45}$$

$S_{\delta\nu}$ is the PSD of frequency fluctuations of the laser and S_V is the voltage noise of the error signal obtained from the quantum efficiency η of the photodiode and its load resistance R and D is the frequency discriminant. The higher the value of D, lesser is the sensitivity of the laser to the voltage noise of the error signal.

For the cavity mentioned in this thesis, the shot noise generated by a photodiode can be estimated by using the equation 1.46

$$S_\epsilon = 2h\nu \times (2P_s), \tag{1.46}$$

where h is Planck's constant and ν is the frequency of the laser light. For a load resistance of 1 kΩ and P_s=2.2 μW, we obtain a voltage noise S_V = 7.2×10^{-19} V^2/Hz. Using the equation 1.45 with an approximate value of $D = 1.2 \times 10^{-18}$ W^2/Hz, we can confirm that the influence of the shot noise is much below the estimated thermal noise limit of the cavity. Hence, we can neglect the effect of shot noise on the performance of this ultra stable laser. For a detailed explanation on thermal noise of the cavity mentioned in this thesis, please refer to section 1.2.6 of Chapter 3 of this thesis.

1.2.7 State-of-the-art

Cavity stabilized lasers have applications in various fields of fundamental research ranging from local oscillators in optical frequency standards [3, 40–42], gravitational wave detection [43, 44], quantum optomechanics [45, 46], fundamental test of physics [47, 48] or for low phase noise microwave generation [49]. These lasers in the future can be used in detection of dark matter [50] and atom based gravitational wave detectors [51].

Generally, these cavity stabilized lasers can be categorized on the basis of the size, material and working temperature of the cavity. The fundamental limitation of a cavity stabilized laser is the thermal noise due to intrinsic Brownian motion and the largest contribution comes from the highly reflective coatings on the mirror substrates [29, 52, 53]. For more details on thermal noise and its effect on a Fabry-Pérot cavity, please refer to 1.2.6.

Fabry-Pérot cavities initially used amorphous dielectric coatings. Cole *et al.* [54–56] proposed a novel technique in replacing the amorphous dielectric coatings by highly reflective crystalline AlGaAs coatings that lead to the reduction of Brownian noise by ten times at room temperature. Villar *et al.* [57] and Harry *et al.* [58] proposed improving the thermal noise performance of optical coatings by doping tantalum pentoxide (Ta_2O_5) with titanium dioxide (TiO_2). This modification reduces the internal mechanical loss in the coating, which is a significant source of thermal noise, especially in precision instruments like gravitational-wave detectors. By incorporating TiO_2,

they were able to reduce the loss angle of the coating, thus lowering thermal noise, without significantly increasing optical absorption. Brückner *et al.* [59] proposed to use coatingless, diffractive mirror substrates to reduce the effect of Brownian motion. Some other approaches employed to reduce the effect of thermal noise in ultra-stable lasers include increasing the beam waist of the cavity mode which allows better averaging of the thermal noise leading to a reduction in its influence.

Gregory *et al.* [60] showed that using mirror substrates with large Young's modulus reduces the thermal noise. However, the most viable solution to reduce the thermal noise limit in an ultra-stable laser is to use ultra-long Fabry-Pérot cavities and working at cryogenic temperatures.

Häfner *et al.* [6] was the first group from PTB (Germany) to report a fractional frequency instability of 1×10^{-16} at an integration time of 1 second to 1000 seconds reaching instabilities of down to 8×10^{-17} for their room temperature ULE cavity with optically contacted fused silica mirrors. The length of the cavity is 48 cm and they managed to reduce the vibration noise to $10^{-10}/(ms^{-2})$ in all directions (x, y and z). Their cavity is based on a cylindrical geometry with a measured finesse of $280,000$.

Matei *et al.* [10] reported two ultra-stable lasers stabilized on a 212 mm long single-crystal silicon Fabry-Pérot cavity, oriented vertically with a working temperature of 124 K in collaboration with PTB (Germany) and JILA (USA). The measured finesse was $500,000$. Additionally, a vibration sensitivity of below $10^{-12}/(ms^{-2})$ in the vertical axis was achieved by exploiting the three-fold symmetry of the silicon crystal, which was oriented along the <111> direction. This symmetry, combined with a three-point support system near the midplane of the cavity, minimized seismic and acoustic vibration effects. By carefully adjusting the azimuthal angle between the cavity and the tripod support, they were able to further reduce the vertical vibration sensitivity. This approach effectively leveraged the anisotropic elasticity of silicon to optimize the system's mechanical response . They reported a record fractional frequency instability of 4×10^{-17} at integration times of 0.8 seconds to few tens of seconds. The paper also reports of obtaining an ultra-low linewidth of 10 mHz with a very low laser frequency drift of 100 μHz/s.

Robinson *et al.* [8] at JILA presented an ultra-stable laser based on a 6 cm long silicon cavity cooled to 4 K. The cryogenic temperature of 4 K was achieved using a three-stage cryogenic thermal damping system. The measured cavity finesse was $500,000$. The fractional frequency instability reached 6.5×10^{-17} at integration times of 0.8 seconds to few tens of seconds. They were also the first group to show a linear dependence of the cavity frequency drift to the incident optical power. The lowest frequency drift of -3×10^{-19} /second was reported for an incident optical power of 40 nW.

The state-of-the-art silicon cavity operating at cryogenic temperature and the state-of-the-art ULE cavity working at room temperature are shown in Fig. 1.7.

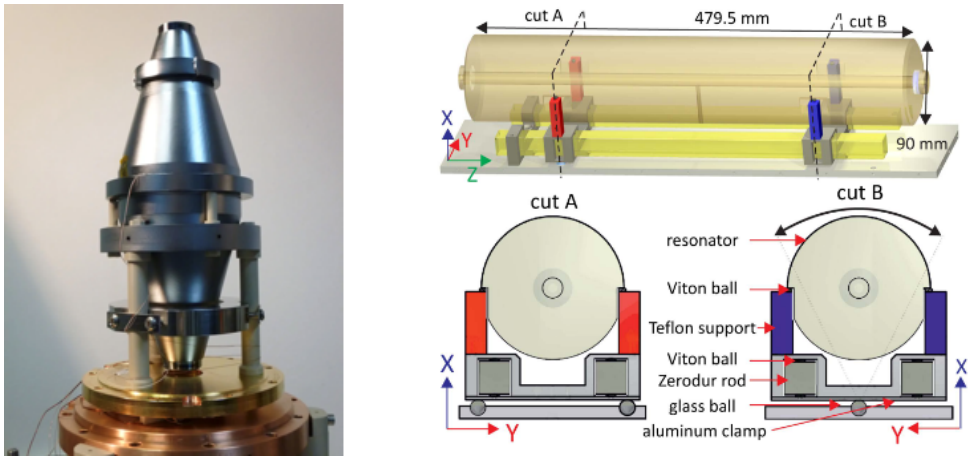

Figure 1.7: Two state-of-the-art Fabry-Pérot cavity designs working at room temperature and cryogenic temperature. (a) Cryogenic silicon cavity with a linewidth of 10 mHz [10]; (b) Room temperature ULE cavity with a fractional frequency stability of upto 8×10^{-17} [6].

Aside from thermal noise, acceleration sensitivity poses technical limitation for a cavity-stabilized laser. Fluctuations induced by acceleration can arise from multiple sources, including seismic activity or acoustic noise. These fluctuations can cause changes in the cavity length, ultimately compromising the laser stability. To mitigate the impact of these external forces, various approaches have been proposed, including vibration isolation techniques and methods specifically designed to reduce acceleration sensitivity.

Young *et al.* [34] presented a Fabry-Pérot cavity with fractional frequency stability of 3×10^{-16} at 1 second integration time in 1999 with a vibration isolation scheme by placing the entire optical bench on rubber supports. Chen *et al.* [61] proposed a way to accurately locate the positions of the support points for the cavity along the optical axis using finite element analysis.

Zhang *et al.* [9] and Robinson *et al.* [8] presented a vertically oriented silicon cavity with vibration sensitivities of the order of 10^{-12}/(ms^{-2}) along the vertical axes. They significantly reduced vibration sensitivity in their silicon cavity by carefully decoupling the cryocooler from the cavity. The cryocooler was mounted on a main plate fixed to a stable foundation, while the vacuum chamber was placed on a mechanically separated split plate. This setup, combined with an active vibration isolation table and optimized support structures via finite element analysis, reduced vibrations by several orders of magnitude, allowing the system to achieve high stability at cryogenic temperature

Leibrandt *et al.* [62] presented an ultra-stable laser based on a spherical cavity with an acceleration sensitivity of 4×10^{-11}/(ms^{-2}) along the vertical direction and 1.6×10^{-10}/(ms^{-2}) and 3.1×10^{-10}/(ms^{-2}) along the two other horizontal directions. The cavity is insensitive to orientation also. The acceleration sensitivity is mostly reduced due to the symmetric spherical geometry. They also suggested that using a smaller area support contact for mounting the cavity may also help in reducing the vibration noise.

Millo *et al.* [33] proposed two Fabry-Pérot cavity designs, one with a vertical optical axis and the next one with a horizontal optical axis. They achieved a vibration sensitivity of better than or equal to 10^{-11}/(ms^{-2}) in both directions for the horizontal cavity. For the vertical cavity, an acceleration sensitivity of 3.5×10^{-12}/(ms^{-2}) in the vertical direction and 1.4×10^{-11}/(ms^{-2}) in the horizontal direction was achieved.

The demand for transportable ultra-stable lasers is rising in various scientific fields, such as geodesy, fundamental physics, atomic clocks, and industrial applications. Precision and stability are paramount for these applications; however, external actors such as vibrations, temperature fluctuations, and pressure variations can degrade the performance of ultra-stable laser systems during transport. While vibrations and temperature shifts are common concerns, atmospheric disturbances, specifically changes in air pressure can subtly impact the optical alignment by causing mechanical stress or deformation in critical components, leading to instability in the laser frequency or precision. These effects, though not immediately apparent, can reduce the laser's overall performance after transport.

To tackle this challenge, research is concentrated on developing vibration isolation systems to shield the laser from external vibrations. Moreover, considerations regarding the size and weight of these lasers are crucial, particularly for applications in remote or space environments.

In conclusion, the significance of transportable ultra-stable lasers spans scientific, industrial, and commercial domains. Ensuring high performance and stability during transport and in challenging environments necessitates the continual development of innovative and robust methods.

Argence *et al.* [63] reported a transportable ultra-stable laser based on a 100 mm long cavity for space applications. The cavity is meant to withstand an acceleration of 20 g while it travels to space. They achieved acceleration sensitivities of $(4 \pm 0.5) \times 10^{-11}$/(ms^{-2}) along the vertical direction and $(6 \pm 3) \times 10^{-12}$/(ms^{-2}) along the horizontal direction.

Tai *et al.* [64] have demonstrated a transportable ultra-stable laser system based on a commercially available fiber laser and a compact, robust optical setup for Pound-Drever-Hall (PDH) stabilization. The laser cavity has a length of 10 cm and a finesse of approximately 400,000. The laser system achieved a frequency stability of 2.2×10^{-15} over a one-second integration time, making it comparable to other state-of-the-art ultra-stable lasers. The portable design of the laser system, along with a vacuum system to eliminate environmental noise, makes it an attractive choice for researchers seeking to conduct experiments in various environments.

Häfner *et al.* [65] reported a transportable interrogation laser system for a strontium lattice clock operating at 698 nm based on a 12 cm-long cylindrical, ULE reference cavity with fused silica mirrors and amorphous dielectric coatings. They reached a stability of 3×10^{-16} at 1 second integration time.

The successor to this ultra-stable laser system was Herbers *et al.* [66], who presented

a transportable clock laser system based on a 20 cm long cylindrical ULE cavity with fused silica mirrors and $Al_{0.92}Ga_{0.08}As$/GaAs mirror coatings. The cavity exhibits a finesse of approximately 300,000 and they have reached stabilities of the order of 1.6×10^{-16} at 1 second integration time, which is among the best achieved for transportable laser systems. The system is also compact and can be transported to various locations, making it ideal for field experiments.

Similarly, Webster *et al.* [67] presented a horizontal cubical cavity design based on a four-point tetrahedral support with an acceleration sensitivity of $2.5\times10^{-11}/(\mathrm{ms}^{-2})$ and a reported finesse of 300,000.

Kelleher *et al.* [68] also presented a transportable cavity stabilised laser based on 6.3 mm long, cylindrical ULE cavity. The diameter of the cavity is 12.7 mm leading to a total volume of 5.2 mL. The reported fractional frequency instability was 2×10^{-14} at 0.1 second integration time with a finesse of 600,000. Three examples of transportable cavities are shown in Fig. 1.8.

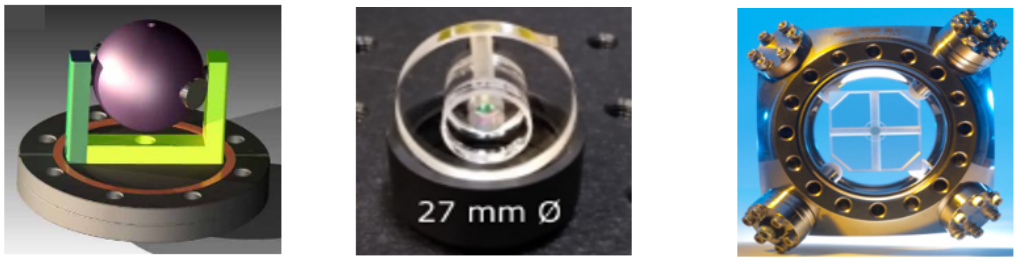

(a) (b) (c)

Figure 1.8: Designs of three transportable Fabry-Pérot cavities. (a) Spherical cavity [62] (b) Cylindrical cavity [68] (c) Cubical cavity [67].

1.2.8 Conclusion

In this section, a presentation of the theoretical aspects of Fabry-Pérot cavity stabilized lasers is provided. The working of a Fabry-Pérot cavity is explained, encompassing various cavity properties such as linewidth, finesse, and transmission modes. The reflection and transmission spectrum, including the phase behavior within the cavity, is thoroughly described.

Furthermore, the Pound-Drever-Hall technique, a widely used method for frequency locking of a laser to the resonance frequency of a cavity, is elaborated upon. The fundamental limitations of a Fabry-Pérot cavity, including thermal noise, thermal expansion, acceleration sensitivity, and electronic noise, are comprehensively discussed, along with the approaches undertaken by researchers to overcome these limitations.

Sophisticated techniques such as cryogenic cooling, vibration isolation, and advanced feedback control methods are employed to mitigate the impact of these noise sources on the laser frequency stability. The characterization of cavity-stabilized laser performance, utilizing tools such as PSD and Allan variance, is presented in detail, highlighting their significance in evaluating stability and accuracy.

Furthermore, the state-of-the-art advancements in Fabry-Pérot cavities are showcased, including developments in size, geometry, and working temperature. Miniaturized cavities with optimized geometries, such as monolithic or micro-cavities, offer improved stability and performance. Cavities designed to operate in extremely low temperatures, such as cryogenic temperatures have also been developed to cater to specific application requirements.

1.3 Time and frequency dissemination over optical fiber links

1.3.1 Introduction

Frequency transfer is a critical process with applications in telecommunications, scientific research, and navigation systems, ensuring precise synchronization and communication. However, achieving accurate and stable frequency transfer over optical fibers is influenced by several factors, including fiber length, optical noise, and dispersion effects.

This section explores the theoretical background of frequency transfer over fiber links, covering the underlying concepts and principles involved. It also addresses the limitations and challenges, focusing on factors like fiber length and optical noise that impact frequency transfer system performance. Emphasizing the importance of overcoming these limitations, the section highlights the significance of achieving precise and reliable frequency transfer in practical applications.

The state-of-the-art in frequency transfer over fiber links is reviewed, encompassing advancements in fiber technology, signal processing techniques, and synchronization methods. Specialized fibers, advanced signal processing algorithms, and digital phase-locked loops (PLLs) are discussed as promising approaches to enhance frequency transfer performance and mitigate limitations.

Moreover, the section analyzes different approaches and techniques utilized in frequency transfer for varying link lengths. This analysis covers long-haul links spanning hundreds or thousands of kilometres, as well as short-haul links covering distances of a few kilometres or less. It outlines the challenges and solutions associated with each link length, offering insights into the current research landscape and potential research directions.

By providing an overview of the theory, limitations, state-of-the-art, and link length considerations in frequency transfer over fiber links, this section establishes the foundation for subsequent discussions and analysis in the thesis. A thorough understanding of fundamental concepts and the current research landscape can provide valuable insights into advancements and challenges in frequency transfer, contributing to its further development for practical applications.

1.3.2 Principle

The principle of optical fiber-based frequency transfer technique relies on a sophisticated round-trip phase noise cancellation method, facilitated through a bidirectional optical fiber link. This technique is designed to suppress the optical length fluctuations of the fiber at the remote end by employing a phase-locked loop (PLL) at the local end to compensate for these fluctuations, as reported in the studies by Ma and Newbury [69, 70]. The phase, and consequently the frequency, of the light propagating through the fiber is inherently influenced by various environ-

mental perturbations, such as thermal and acoustic effects, which introduce Doppler frequency shifts along the path through the fiber, as elaborated in subsection 1.3.3.

To effectively detect and cancel these Doppler frequency shifts over optical fibers, the optical interferometry concept is combined with electronics in a novel approach. The general scheme used to implement this technique is shown in Fig. 1.9.

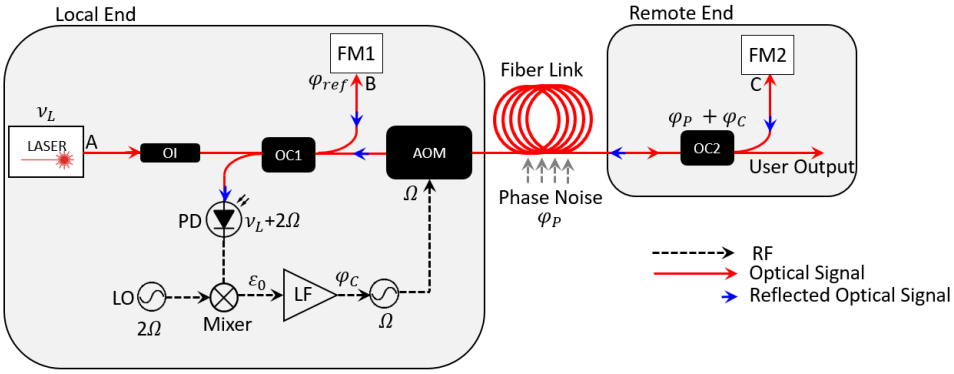

Figure 1.9: Schematic diagram illustrating the frequency dissemination setup using an optical fiber link. The components include a photodiode (PD), Faraday mirror (FM), optical isolator (OI), optical coupler (OC), local oscillator (LO), and acousto-optical modulator (AOM).

Specifically, a heterodyne Michelson interferometer, a type of optical interferometer that utilizes a beam splitter or a fiber optic coupler (OC1) to split light from the same source into two different optical paths, is employed in the conventional interferometry setup. The first path, denoted as the distance between points A and B in a heterodyne phase detection scheme, serves as a short reference path. The second path, determined by the distance between points A and C, is used to transfer the signal through the fiber link. To introduce a frequency shift, an Acousto Optical Modulator (AOM) is inserted into the beam path at the local end.

At the remote end of the fiber link, a portion of the light is sent back to make a round-trip through the fiber link by passing through a Faraday mirror (FM2), and is then made to interfere with the light reflected back from the local end through another Faraday mirror (FM1). FM2 at the remote end rotates the polarization of light by 90 degrees, which allows for the distinction between the forward and backward directions of light traveling through the fiber. The reflected light is then directed to a photodetector (PD1), where a heterodyne beatnote is generated in the radio-frequency (RF) domain between the round-trip light and a local copy of the original signal at 2Ω, where Ω represents the introduced frequency shift due to the AOM. The factor of 2 arises from the round-trip of light. Heterodyne beat detection is employed because it allows for the measurement of phase and frequency shifts with more precision by converting the high-frequency signal into a lower, more manageable intermediate frequency in the microwave range. This method increases sensitivity and improves the signal-to-noise ratio by isolating and amplifying the beat frequency. The heterodyne process also preserves the phase information of the optical signal.

The beatnote signal contains critical information about the accumulated phase noise

of the fiber (φ_P). This beatnote signal is then fed into a frequency mixer, where it is mixed with a reference signal through the Local Oscillator (LO) input. The resulting mixed signal contains the dephasing between the reference arm and the long arm of the Michelson interferometer, which serves as the error signal (ϵ_0) for the servo-loop filter (LF) that is used to correct the phase fluctuations. The servo-loop filter incorporates proportional and integral functions to generate corrections (φ_C) that are added via the AOM.

1.3.3 Fundamental limits of optical fiber communication systems

Attenuation

Fiber attenuation refers to the reduction in signal power as it travels through an optical fiber. The amount of signal loss depends on factors such as the wavelength of the transmitted light, the fiber's length, quality, and the presence of physical or technical mechanisms causing loss. In telecommunications, fused silica single-mode fibers (such as SMF-28) are commonly used, where attenuation is typically around 0.2 dB per kilometre in the wavelength window near 1550 nm.

As fiber length increases, especially over several tens or hundreds of kilometres, the system becomes increasingly susceptible to phase noise. Environmental factors, such as temperature fluctuations and mechanical vibrations, introduce noise that accumulates along the fiber, resulting in increased phase noise. This phase noise must be canceled to maintain the integrity of the frequency transfer. Beyond 100 km, attenuation becomes more significant, requiring the use of amplifiers or repeaters, which may introduce additional noise.

The bandwidth of noise cancellation systems is also affected by the fiber length due to the round-trip delay. For example, in a 100 km fiber link, the round-trip time is approximately 1 ms. This limits the system's ability to correct high-frequency noise fluctuations beyond 1 kHz. As a result, longer fiber lengths pose greater challenges for real-time noise correction and frequency transfer over long distances.

Parallelly, as the wavelength increases ($\lambda > 1700$ nm), absorption by impurities in the glass leads to greater attenuation. Conversely, at shorter wavelengths ($\lambda < 500$ nm), intrinsic UV absorption becomes the dominant factor. Additionally, technical losses from fiber bending and connectors contribute to overall attenuation. Therefore, it is crucial to implement proper fiber design, fabrication, and characterization techniques to minimize these losses and ensure efficient, reliable optical signal transmission.

As part of this thesis, I will investigate a laboratory-scale optical fiber link approximately 25 meters in length, using 1550 nm light. In this setup, attenuation is expected to be negligible for the purposes of the experiment.

Phase Fluctuations

Generally, the major sources of noise in fiber-optic connections in telecommunication networks are caused by temperature fluctuations and mechanical perturbations mostly due to stress induced refractive index variation. Mechanical perturbations affect optical fibers at short time scales ($< 100\ s$). For longer time scales ($> 100\ s$), optical fibers are mostly affected by thermal perturbations induced by the change of the refractive index of the fibers due to thermal fluctuations and thermal expansion. These fluctuations cause a change in the length of the optical path. So, for time transfer, the fluctuations induce timing errors and in frequency transfer, it induces Doppler shifts of the transmitted frequency.

Let us consider we have a monochromatic light beam, propagating through an optical fiber of length L_{fiber}. A phase shift of φ_{fiber} is introduced while propagation. A relation can be established between φ_{fiber} and L_{fiber} given by the equation 1.47

$$\varphi_{fiber} = \frac{\omega_0}{c} n L_{fiber} \tag{1.47}$$

where, ω_0 is the angular frequency of light, c is the speed of light and n is the refractive index of the medium. For a change in phase ($d\varphi_{fiber}$) during a time dt, the corresponding frequency shift ($\Delta\nu_{fiber}$) can be defined by the equation 1.48

$$\Delta\nu_{fiber} = \frac{d\varphi_{fiber}}{dt} = \frac{\omega_0}{c} \frac{d(nL_{fiber})}{dt}. \tag{1.48}$$

If the frequency shift in the fiber is caused by changes in temperature (dT), equation 1.48 can be written by the equation 1.49

$$\Delta\nu_{fiber} = \frac{d\varphi_{fiber}}{dt} = \frac{\omega_0}{c} \left[L_{fiber} \frac{dn}{dT} \frac{dT}{dt} + n \frac{dL_{fiber}}{dT} \frac{dT}{dt} \right] \tag{1.49}$$

where, $\frac{1}{n}\frac{dn}{dT} = \alpha_n$ is called the thermo-optic coefficient of the fiber $(dL_{fiber}/dT)/L_{fiber} = \alpha_\Lambda$ is the coefficient of thermal expansion of the fiber glass. α_Λ at room temperature has a typical value of $5.6 \times 10^{-7}/°C$ while the thermo-optic coefficient has a value of $\alpha_n = 1.06 \times 10^{-5}/°C$ [71, 72] which is about twenty times higher and is the root cause for phase shifts in light through the fiber due to changes in temperature. Generally, aerial fibers are more prone to noise from environmental perturbations than fibers buried in the soil [73–75].

The temperature induced length variations in a fiber are much lower compared to tem-

perature induced refractive index change. Hence, equation 1.49 can be simplified as 1.50

$$\Delta\nu_{fiber} = \frac{d\varphi_{fiber}}{dt} = \frac{\omega_0}{c}\left[L_{fiber}\frac{dn}{dT}\frac{dT}{dt}\right]. \tag{1.50}$$

External pressure, such as from mechanical stress or environmental conditions, can impact the stability of optical fiber links. Mechanical stress, caused by bending, twisting, or crushing of the fiber cable, can introduce additional loss or attenuation to the transmitted signal. This can result in decreased signal strength, reduced signal-to-noise ratio (SNR), and ultimately degraded link performance. This phenomenon is known as the acousto-optic effect. When there is a time-varying acoustic pressure applied to the fiber, it can result in changes in the refractive index, leading to frequency shifts in the transmitted optical signal. To account for the effect of acoustic pressure on the refractive index, we replace the term $\left(\frac{dn}{dT}\frac{dT}{dt}\right)$ with $\left(\frac{dn}{dP}\frac{dP}{dt}\right)$, where $\frac{dn}{dP}$ is the pressure coefficient of the refractive index and $\frac{dP}{dt}$ is the rate of change of pressure with time.

Stimulated Brillouin Scattering

Stimulated Brillouin scattering (SBS) occurs when intense light in an optical fiber interacts with acoustic waves, causing backscattering at a lower frequency. This process is driven by electrostriction, where the optical field creates density fluctuations in the medium, generating acoustic waves. The interaction between the forward-propagating light and the backward-scattered light forms a feedback loop, amplifying the scattered signal. The Brillouin frequency shift (ν_B) depends on the optical wavelength (λ_0) and the speed of sound in the fiber (v_s), and is given by the equation 1.51

$$\nu_B = \frac{2nv_s}{\lambda_0}, \tag{1.51}$$

where, n is the refractive index, v_s= 6×10^3 m/s which is the speed of sound in glass and λ_0 is the wavelength. For silica-based optical fibers such as SMF-28, which are commonly used in telecommunications, the Brillouin frequency shift is typically around 11 GHz for a wavelength of 1550 nm. SBS becomes more prominent in longer fiber links due to the cumulative effect of scattering over distance, reducing the power transmission capabilities of optical systems. However, for short fibers such as a 15 m link, SBS is less significant since the shorter interaction length limits the energy transfer to backward-propagating Stokes waves. In such short links, the SBS threshold (the power level beyond which SBS becomes problematic) is much higher, allowing greater optical power to be used without encountering significant Brillouin scattering [76, 77].

Polarization mode dispersion (PMD)

In optical fibers, mechanical stress can induce changes in the refractive index, leading to the phenomenon of polarization mode dispersion (PMD), where light propagates with two different

modes that have orthogonal polarization and different speeds. This results in birefringence, which can cause propagation delays between orthogonal polarisations and limit the frequency transfer performance. The time difference between the two polarization modes is known as differential group delay (τ_{DGD}). While it is not possible to calculate τ_{DGD} analytically, it can be estimated statistically.

PMD can have detrimental effects on optical communication systems, as it can cause random fluctuations in the arrival time of different polarization modes of light, leading to signal distortions and degradation of system performance.

PMD is a well-known effect in optical communication systems and has been extensively studied in the literature [78–81]. For the specific case of the SMF-28 fiber that is being used in the thesis, the datasheet indicates a low PMD coefficient of 0.1 ps/$\sqrt{\text{km}}$ [82]. The PMD coefficient is a measure of PMD in an optical fiber, typically expressed in ps/$\sqrt{\text{km}}$.

However, in the context of the thesis, where a relatively short fiber link of only 15 m is being considered, the impact of PMD is expected to be minimal. The calculated DGD for the given fiber length of 15 m is only 12 fs, which is well below the tolerable limits for most optical fiber links used for frequency dissemination. Therefore, it is reasonable to neglect the effect of PMD in this case, and the focus of the thesis can be directed towards other relevant factors affecting the system performance.

1.3.4 State-of-the-art

Fiber-based time and frequency transfer techniques have been successfully implemented across various scales, ranging from laboratory to continental distances, to achieve ultra-stable frequency dissemination while preserving spectral purity. Optical fiber techniques offer significant advantages compared to satellite-based time and frequency transfer techniques such as GPS or two-way satellite time and frequency transfer (TWSTFT), as reported by Bauch [83], with performance levels surpassing satellite-based techniques by over four times of magnitude. This is attributed to the higher frequencies of optical carriers, which enable improved resolution. Satellite-based systems are limited to an accuracy level of 10^{-15} in one day, as reported by Brown, Lombardi, and Larson [84–87], which is inadequate for comparing optical clocks due to their higher stability requirements.

Ultra-stable frequency transfers over optical fiber networks find numerous applications in various scientific fields, including time and frequency metrology [83, 88–91], high-precision measurements of atomic or molecular absolute frequencies [92–94], radioastronomy [95], fundamental tests of physics through clock frequency comparisons to test the stability of fundamental constants [96–100], astrophysics including very long baseline interferometry (VLBI) and the NASA deep space network (DSN), and particle physics such as the Large Hadron Collider (LHC) [101, 102]. Notably, A. Matveev *et al.* [92] and K. Predehl *et al.* [103] reported the measurement of the optical fre-

quency of the 1S-2S atomic transition in hydrogen with a relative uncertainty of 4.5×10^{-15} using a remote Cs frequency standard and a 920 km long optical fiber link, achieving a fractional frequency stability of 4×10^{-19} at 2000 seconds. Recent advancements in noise cancellation techniques have enabled ultra-stable frequency transfer from laboratory or campus scales to continental scales, achieving accuracy levels as low as 10^{-20} [104].

In the realm of long-distance optical fiber communication networks (exceeding 500 km), recent advancements have been made in achieving ultra-stable frequency transfers. A noteworthy example is the work of M. Schioppo *et al.*[105], who presented a pioneering 2220 km long fiber link connecting the United Kingdom and Germany for comparing two state-of-the-art ultra-stable lasers. These lasers demonstrated fractional frequency instabilities of 7×10^{-17}, with an integration time ranging from 30 seconds to 200 seconds. This remarkable achievement represents the longest fiber link ever constructed for time and frequency transfer.

Prior studies have also reported significant progress in this field. For instance, Droste *et al.* [106] achieved a fractional frequency instability of 2.7×10^{-15} at an integration time of 1 second for an underground optical fiber link spanning 1840 km, which further improved to 4×10^{-19} at 100 seconds. Raupach *et al.* [104] demonstrated even lower instabilities, below 6.9×10^{-21} at an averaging time of 30000 seconds, by implementing cascaded Brillouin amplification in their 1400 km long optical fiber link connecting PTB, Braunschweig (Germany) and Strasbourg (France). Stefani *et al.* [107], Chiodo *et al.*[108], and Calonico *et al.* [109] also reported uncertainties at the level of 10^{-19} through their long-haul fiber links.

These advancements in achieving ultra-stable frequency transfers over long distances in optical fiber networks open up new possibilities for various applications in fields such as time and frequency metrology, high-precision measurements of atomic or molecular absolute frequencies, and fundamental tests of physics.

Fig. 1.10 shows the 2220 km long European fiber link network, that extends from National Physics Laboratory, UK to PTB, Germany via SYRTE, Paris and University of Strasbourg, that was used to compare two state-of-the art ultra stable lasers between these two labs with fractional frequency stability levels of 7×10^{-17} [105].

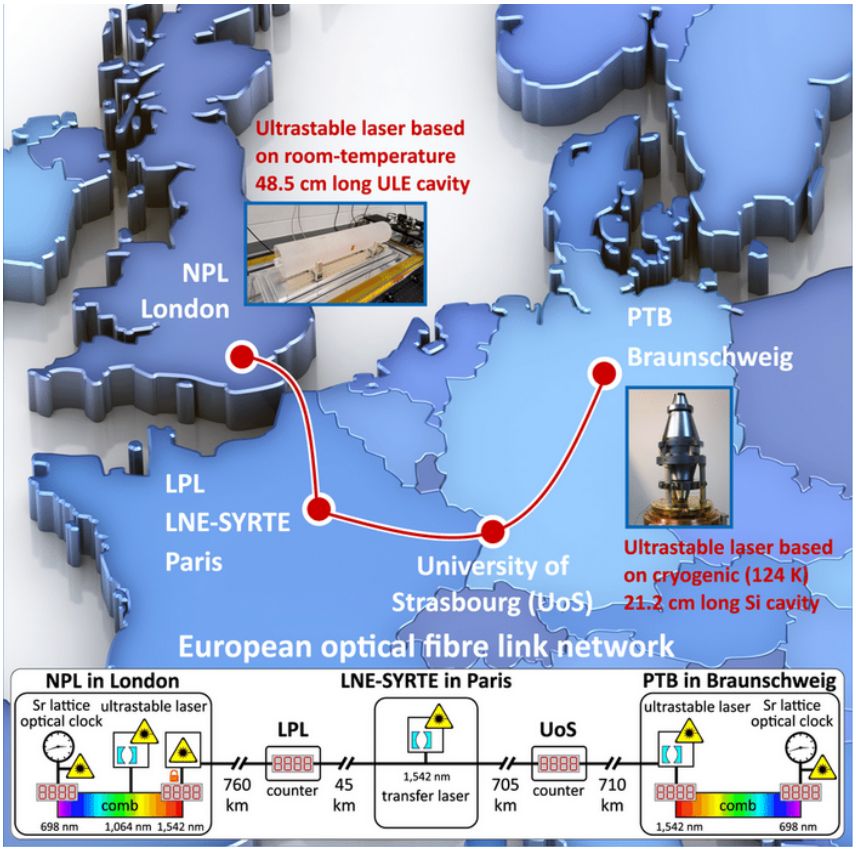

Figure 1.10: Schematic of the continental scale 2220 km long European fiber link network connecting Europe with the United Kingdom. This fiber link network was utilized to compare the performance of two state-of-the-art ultra-stable lasers between two laboratories, demonstrating fractional frequency stability levels of 7×10^{-17} [105].

In the domain of medium to short optical fiber links, notable achievements have been reported by researchers. Kudeyarov *et al.* [110] demonstrated a 2.8 km long optical fiber link for characterizing a transportable Yb^+ clock, achieving residual noise in terms of FFS (Fractional Frequency Stability) of 5×10^{-16}. The fiber link used in this study had a frequency stability of 2×10^{-19} at an integration time of 1100 seconds. Furthermore, NIST researchers in Boulder, Colorado (USA) presented a network of optical clocks based on Al^+, Sr, and Yb^+ with uncertainties below 10^{-18}, and the performance of these clocks was compared through fiber links and a 1.5 km long free space link over a duration of 8 months [111–113].

In another study, Bercy *et al.* [114] presented a 100 km long fiber link in two different configurations. The first configuration involved a two-way optical frequency transfer technique using two optical fibers for each propagation way and unidirectional amplifiers, achieving a fractional frequency stability of 2×10^{-17} at an integration time of 4000 seconds. The second configuration employed a two-way setup with a single optical fiber and bidirectional amplifiers, which outperformed the unidirectional approach with a fractional frequency stability of 5×10^{-21} at the same integration time of 4000 seconds. These findings highlight the significant advancements in optical fiber links for time and frequency transfer in medium and short distance ranges, as demonstrated

by these studies.

In recent years, there has been significant progress in digital electronics for optical systems, leading to the replacement of conventional analog electrical components. High-resolution analog-to-digital converters (ADCs) and digital-to-analog converters (DACs), field programmable gate arrays (FPGAs), and direct digital synthesizer (DDS) RF generators are now widely used in time and frequency metrology, offering improved performance, software reconfigurability, low costs, easy integration, easy replication, and compact control electronics for various applications.

Researchers such as Dietrich *et al.* [115], Huang *et al.* [116], and Preuschoff *et al.* [117] have proposed FPGA-based digital lock-in techniques for frequency stabilization of lasers on Fabry-Pérot cavities, replacing conventional lock-in amplifiers and analog PID control. Dietrich *et al.* [115] also demonstrated the generation of modulation signals required for electro-optic modulation (EOM) using the same hardware. Furthermore, Software Defined Radio (SDR) setups based on FPGAs can control multiple channels in parallel with high data rates and computing power, as shown by Pruttivarasin *et al.* [118], who proposed an FPGA-based pulsed sequencer and multi-channel RF generator for trapped atom experiments, replacing bulky and expensive single-channel analog RF signal generators.

Digital phase-locked loops (DPLLs) are also widely used for phase and frequency control in various applications. Tourigny *et al.* [119] implemented a low-cost FPGA-based DPLL based on an open-source design [120]. Mahnke *et al.* [121] and Stimpson *et al.* [122] proposed a software-defined radio for use in lock-in amplifiers.

DPLLs have also been implemented for optical frequency dissemination over optical fiber links. Calosso *et al.* [123] reported the benefits of digital electronics over analog electrical components in a 47 km long metropolitan optical fiber communication network. Olaya *et al.* [124–126] successfully implemented an FPGA-based DPLL for a 300 km long optical fiber link, incorporating phase detection and fiber noise compensation techniques using a tracking direct digital synthesizer (DDS) approach on the same FPGA-based board [127].

1.3.5 Conclusion

In conclusion, this section has provided an overview of the theory of frequency transfer over fiber links, highlighting the fundamental principles and limitations involved in this process. The significance of frequency transfer in various fields, such as telecommunications, scientific research, and navigation systems, has been emphasized, underscoring the need for accurate and reliable frequency transfer methods.

The limitations of frequency transfer over fiber links, including factors such as fiber length and optical noise, have been discussed. However, researchers are continuously working towards overcoming these limitations through advancements in fiber technology, signal processing techniques, and synchronization methods, as evident from the state of the art in this field.

The current state of the art in frequency transfer over fiber links has been summarized, with an emphasis on the use of specialized fibers, advanced signal processing algorithms, and digital phase-locked loops to improve frequency transfer performance. The advantages of digital PLLs, such as high stability, flexibility, and adaptability, have been highlighted.

1.4 Objectives of thesis

The primary objective of this thesis is to design and develop a highly stable and transportable laser system based on a Fabry-Pérot cavity with a short length of 25 mm. The cavity spacer is fabricated using ultra-low expansion glass with fused silica substrates coated with reflective crystalline coatings made of AlGaAs, known for its high reflectivity and high Q factor in the desired wavelength range. The intended operating temperature for the cavity is room temperature, and the expected thermal noise floor is set at an ambitious level of 1×10^{-15}, reflecting the stringent stability requirements of the system.

The first goal of the thesis is to improve the performance of an existing Fabry-Pérot cavity by optimizing the digital electronics scheme that is currently implemented. This will involve carefully analyzing and optimizing the electronic components, control algorithms, and feedback mechanisms to minimize noise sources, reduce system complexity, and enhance the overall stability and performance of the cavity. It is hypothesized that the use of digital electronics, with its inherent advantages of precision, flexibility, and scalability, can result in a more compact and efficient cavity compared to analog electronics.

Furthermore, the initial version of the Fabry-Pérot cavity used in this study lacks a coefficient of thermal expansion zero crossing, which may have implications on the overall stability and performance of the system. The thesis aims to investigate the underlying reasons for this limitation, through experimental and theoretical analyses, and propose appropriate solutions to overcome this challenge.

The second goal of the thesis is to design a new Fabry-Pérot cavity that surpasses the performance of the previous version. This will involve a comprehensive analysis of the system requirements and constraints, followed by design and fabrication of a compact setup for the entire cavity, including specialized boxes for optical fibers and electronics. The emphasis will be on reducing the footprint and size of the electronics compared to the earlier version, while maintaining or enhancing the stability and performance of the system. The proposed design will be thoroughly tested and validated, and its performance will be compared with the existing cavity to demonstrate the improvements achieved.

The subsequent objective of this thesis is to design a compact and noise-compensated frequency dissemination setup that can effectively distribute the ultra-stable laser signal generated from the Fabry-Pérot cavity to different rooms for various applications. These applications may include low-noise microwave generation through frequency comb locking, serving as a reference for other stable lasers in the laboratory, and other related uses.

The design of the frequency dissemination setup will focus on achieving high stability and low noise performance. This will involve careful consideration of the system architecture, including the selection of appropriate components such as fiber-optic cables, splitters, amplifiers,

and phase-locking techniques, to minimize the introduction of noise and fluctuations into the transmitted signal. Special attention will also be given to compensating for potential environmental and technical noise sources, such as temperature fluctuations, vibrations, and electronic noise, through innovative noise reduction techniques and advanced signal processing algorithms.

The setup will be designed to be compact, ensuring efficient use of space and easy integration into different laboratory environments. The frequency dissemination setup will be thoroughly characterized and validated to demonstrate its performance in maintaining the high frequency stability of the ultra-stable laser signal during distribution to different rooms. This will involve comprehensive measurements and analyses to quantify the stability and noise performance of the distributed signal, and comparison with established performance benchmarks.

The successful implementation of the compact and noise-compensated frequency dissemination setup will enable the widespread utilization of the ultra-stable laser signal in various applications, such as precision measurements, frequency metrology, and advanced scientific research, where high stability and low noise performance are critical requirements. The outcomes of this thesis will contribute to advancing the field of optical frequency metrology and its practical applications, providing valuable insights and solutions for the design of frequency dissemination systems in other research and industrial settings.

Chapter 2

Frequency dissemination over short optical fiber

2.1 Introduction

In this chapter, I will present a thorough demonstration of the effective realization of a laboratory-scale frequency transfer system. The system is tested with an ultra-stable laser that is locked to a Fabry-Pérot cavity. The cavity exhibits a Fractional Frequency Stability (FFS) of 2×10^{-15} at an integration time of 1 second. The core aim of this setup is to distribute the highly stable optical signal produced within one room of our laboratory to another, preserving its spectral integrity and frequency stability against external disturbances.

To achieve this, we employ compensation techniques to mitigate the noise introduced by temperature changes and vibrations that occur during signal transmission. Perturbations in the signal caused by the noise are detected through precise measurements of the optical signal phase shift. We then utilize a digital phase-locked loop (PLL) implemented using a Redpitaya commercial board to cancel out these perturbations, ensuring the signal remains stable and pure.

During the course of my doctoral studies, I dedicated significant effort to improve the noise compensation technique for this fiber link. I will provide a detailed account of the steps taken to achieve this improvement, including the methodology and experimental procedures. Furthermore, I will present the results obtained during my research, including assessments of residual noise in the frequency domain ($S_\varphi(f)$) and the time domain ($\sigma_y(t)$). The noise-compensated fiber link setup that I designed demonstrates residual noise measured at 2×10^{-18} in terms of FFS at 1 second integration time in the time domain, a significant advancement that makes it suitable for transmitting signals from cutting-edge cavity-stabilized lasers and optical atomic clocks.

In addition to the laboratory-scale setup, we have also developed a compact version of the fiber link that is designed to be mounted in a 19-inch rack. This compact setup encompasses all the necessary components, such as the fiber, amplifiers, detectors, and electronics, integrated

within a single box, complete with its own low-noise power supply. This compact setup offers a portable and convenient solution for transferring ultra-stable optical signals between different locations, without compromising on the signal quality or stability.

In conclusion, the laboratory-scale fiber link setup presented in this chapter represents a significant scientific advancement in achieving highly stable frequency transfer over short to intermediate distances. Despite the limitations, such as the requirement for precise environmental control, this technology has the potential for wide-ranging applications in fields such as telecommunications, astronomy, and timekeeping. Further research and development efforts hold promise for pushing the boundaries of frequency stability and expanding the practical applications of this technology.

2.2 Principle

The development of a laboratory-scale, noise-compensated, ultra-stable frequency dissemination system utilizing optical fibers has been an area of significant interest in recent years [90–100, 103, 104]. One of the promising approaches to achieve this goal is the implementation of the so-called Doppler cancellation scheme based on a heterodyne Michelson interferometer (HMI) technique.

The first optical path, which is identified as the short arm of the HMI, serves as a stable reference point, characterized by a fixed length. This reference provides a benchmark for comparison with the second optical path, known as the long arm of the HMI. The long arm primary responsibility is to transfer the optical signal originating from the source. Although this path introduces frequency shifts primarily through the use of an acousto-optical modulator (AOM), it remains vulnerable to noise disturbances caused by thermal perturbations and mechanical vibrations. These factors can result in phase shifts in the laser light as it propagates along the long arm.

As the laser beams from the individual optical paths recombine at the beam splitter, a beatnote is generated. This beatnote signal carries information related to the phase fluctuations or shifts that take place in the optical path during the light passage through the long arm of the HMI. The RF beatnote is detected by a photodiode which allows for subsequent correction using a PLL. This PLL incorporates the AOM for frequency shift compensation, effectively counteracting the phase fluctuations.

To obtain a deeper understanding of the principle, I encourage readers to consult Section 1.3.2 for an explanation. In summary, the HMI technique furnishes an efficient resolution for achieving a noise-corrected stable frequency distribution system from a laboratory scale to a continental scale, using optical fibers. By tackling the hurdles posed by phase fluctuations and noise disruptions, this methodology offers a substantial enhancement in frequency transfer and signal stability, thereby broadening the applicability across domains where precision and accuracy hold utmost significance.

2.3 Optical Scheme

The primary objective of this experiment is to transmit an ultra-stable signal generated from a laser stabilized on a Fabry-Pérot cavity across two rooms situated 15 meters apart, using optical fibers. To achieve this goal, an integrated experimental apparatus consisting of both signal transmission and characterization setups has been implemented. This combined system incorporates a HMI for efficient signal transmission and a heterodyne Mach-Zehnder interferometer (HMZI) for precise system performance assessment, as illustrated in Fig. 2.1.

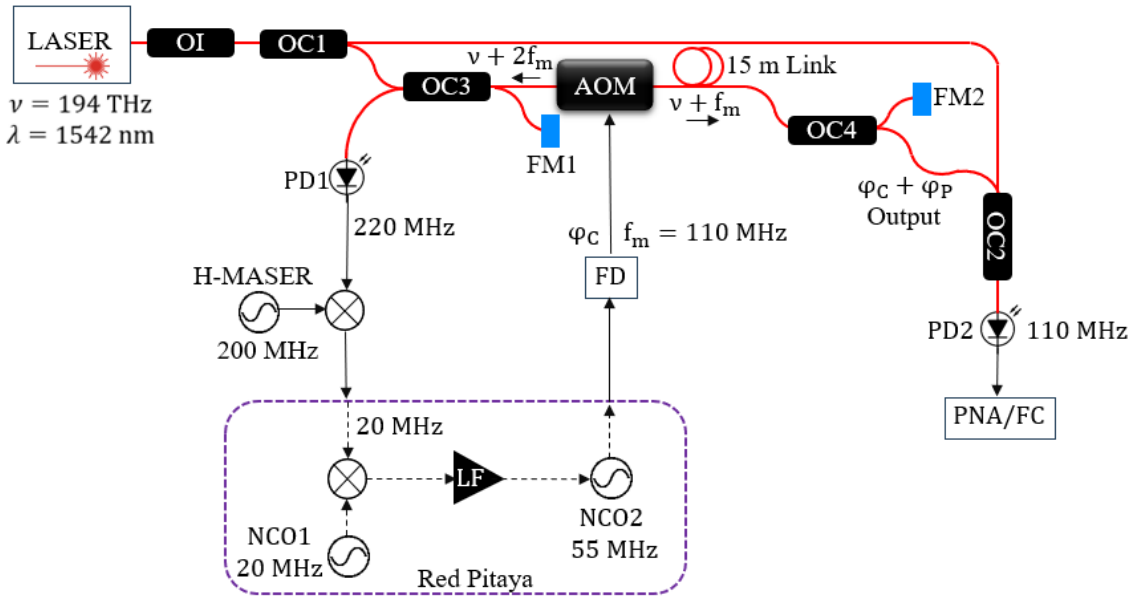

Figure 2.1: Laboratory-scale 15 m optical fiber link experimental setup, showing optical fibers (red lines), radio frequency cables (black dashed lines), and digital signals (black solid lines). Components include Faraday mirrors (FM1, FM2), acousto-optical modulator (AOM), optical couplers (OC1-OC4), numerically controlled oscillators (NCO), optical isolator (OI), photodiodes (PD1, PD2), phase noise analyzer (PNA), frequency counter (FC), and frequency doubler (FD).

In the context of time and frequency dissemination over optical fibers, we consider a laser source operating at 194.4 THz with a corresponding wavelength of 1542.42 nm. This laser emits 14 mW power, which is directed through an optical isolator (OI) into a 90:10 splitting ratio optical coupler (OC1). The system utilizes OC1 to bifurcate the laser beam, effectively distributing it between two distinct paths: characterization and signal transmission.

The 90 % output of OC1 is channeled towards a 90:10 optical coupler (OC3), which functions as a beam splitter for the heterodyne Michelson interferometer, dividing the incident light into two separate optical paths. The 10 % portion of OC3 output is reflected back by Faraday mirror FM1, which serves as a reference with phase φ_{ref} and constitutes the short path. Conversely, 90 % of the light is directed into a 15 m long link via an AOM. This long path constitutes the signal arm of the Michelson interferometer, guiding the optical signal through a 15 m optical fiber link, from OC3 secondary output to another Faraday mirror (FM2), with the AOM positioned along the route. The AOM mitigates environmental perturbations' impact on the optical signal phase in the signal arm (φ_P) by introducing a controlled phase (φ_C) at an operational frequency of 110 MHz.

Subsequently, the optical signal is subjected to another 90:10 beam splitter (OC4) at the fiber link output, segregating the signal into two segments. One output port caters to the user, while the other returns the signal through FM2 to form the HMI long arm. A detector at the interferometer output port measures the phase difference between the reference and signal arms. The signal at OC4 possesses a total phase described by the equation 2.1

$$\varphi_T = \varphi_P + \varphi_C. \tag{2.1}$$

Arising from the constructive interference between the round-trip optical signal and the signal reflected by FM1, a beatnote forms at 2f$_m$ = 220 MHz on PD1. This 220 MHz signal carries the phase variations induced by environmental perturbations along the extensive optical pathway. The primary objective involves mitigating these phase fluctuations, denoted by φ_P, through the deployment of a digital PLL. Upon detection by the photodetector, the 220 MHz signal is demodulated, revealing the phase perturbations that are subsequently compensated for by the PLL. Following this adjustment, the corrected signal is conveyed to the optical link by the AOM utilizing a driving frequency of 110 MHz, which is supplied by a voltage-controlled oscillator (VCO) and a high-power RF amplifier. An error signal is generated, which is represented by the equation 2.2

$$\epsilon = 2(\varphi_P + \varphi_C - \varphi_{ref}) - \varphi_0. \tag{2.2}$$

Here, φ_0 denotes the phase of the RF reference signal. When the loop filter is activated, ϵ diminishes to zero, indicating compensation of the link phase fluctuations. Ultimately, the noise-compensated output of the link exhibits a total phase given by the equation 2.3

$$\varphi_T = \varphi_{ref} + \frac{1}{2}\varphi_0. \tag{2.3}$$

This equation suggests that the phase at the output of the link, φ_T, primarily depends on the phase of the reference arm, φ_{ref}, and the RF reference, φ_0. Consequently, the noise compensation of the link is fundamentally constrained by the reference arm and the utilized RF reference signal.

The 10 $\%$ output of OC1 is employed for characterizing the setup by connecting it to a 50:50 optical coupler (OC2), the second input of which corresponds to the user output (i.e., the output of OC4). The heterodyne Mach-Zehnder interferometer (HMZI) scheme is implemented for characterization purposes. The first arm of the HMZI is formed by the uncompensated path between OC1 and OC2, while the second arm is established by the ultra-stable link and its output. A beatnote at 110 MHz is produced due to the interference between the signals of these two arms. During the characterization process, the user output is rendered inaccessible as it is connected to OC2. Please note that to assess the performance of the system, the characterisation setup is placed on the same optical table as the original setup.

In order to assess the performance of the link in time and frequency domain, a Phase Noise Analyzer (PNA, Rohde $\&$ Schwarz FSWP) and a Frequency Counter (FC, K+K FXE) are utilized. A beatnote forms at 110 MHz and is dispatched to a frequency counter or a phase noise analyzer to assess the system performance. It is essential to note that the optical path between OC1 and OC2 is not compensated. Hence, this path is maintained as brief as possible.

2.4 Control Electronics

This section presents an overview of the electronics scheme for implementing a digital PLL in optical fiber frequency dissemination. It begins with essential digital signal processing concepts, crucial for understanding the digital PLL architecture and its components' functionality. The control electronics scheme, including key elements like ADCs, DACs, and DSPs, will be explored, highlighting their roles and control algorithms in maintaining phase coherence. The goal is to provide an understanding of the principles and practical implementations for an effective digital PLL system in optical fiber frequency dissemination.

2.4.1 Concepts

Nyquist Shannon Theorem

The Nyquist-Shannon theorem states that to accurately transform an analog continuous-time signal into a discrete-time signal in the digital realm, the signal should be sampled at a rate of at least twice the frequency of its highest frequency component. This theorem rests on the principle that sampling an analog signal at specific times causes information loss. To prevent this loss, the sampling rate must be sufficiently high to capture the full analog signal spectrum, facilitating precise reconstruction as a digital signal.

The f_N, half of the minimum required sampling rate, represents the maximum frequency that can be accurately represented digitally. The signal frequency to be correctly portrayed in the digital domain must not exceed the f_N. For instance, in the context of an analog-to-digital converter (ADC) operating at a 125 MS/s sampling rate, the f_N equals half of this rate, or 62.5 MHz. To guarantee accurate digital representation of an analog signal, its frequency must be less than or equal to this Nyquist frequency.

Aliasing

Aliasing arises when an analog signal is sampled at a rate lower than twice its highest frequency component. This can lead to higher-frequency components being misinterpreted as lower-frequency ones, resulting in data loss and distortion of the original signal.

Illustrating this, consider a scenario with a beatnote signal frequency of 220 MHz, sampled by an ADC at 125 MS/s. Here, the Nyquist frequency is 62.5 MHz. To accurately portray the signal digitally, the sampling rate must exceed twice the signal highest frequency, which in this case is 440 MHz. However, the FPGA board maximum sampling rate is limited to 125 MS/s, leading to undersampling. Consequently, the signal is undersampled, causing aliasing. Specifically, the

220 MHz signal folds back into a lower frequency, determined by the formula 2.4

$$f_A = 2f_S - f_{signal}, \tag{2.4}$$

where, f_A denotes the aliased frequency, f_S is the sampling frequency, and f_{signal} represents the frequency of the original signal. Hence, in this scenario, the 220 MHz signal appears as a lower 30 MHz frequency signal. Despite its drawbacks, proper signal processing techniques can mitigate aliasing, enabling accurate analog-to-digital representation. Notably, the signal phase remains intact in the digital realm.

2.4.2 Digital PLL Scheme

Creating a digital phase-locked loop involves using FPGA based Redpitaya STEMlab 125-14 board. This board has a System-on-a-Chip (SoC) design and comes with two input and two output channels. These channels have high-quality 14-bit ADC and DAC converters, allowing accurate measurement of signal phase and frequency.

The SoC part of the Redpitaya board uses the Xilinx Zynq 7010 embedded processor. This provides flexibility to program the digital PLL algorithm using software or hardware. The board internal clock is a precise quartz oscillator running at 125 MHz, giving each channel a consistent sampling rate of 125 MS/s. For achieving phase locking, two different methods are used depending on the beatnote signal frequency.

2 stage demodulation

The proposed approach involves a demodulation process that uses two stages of multiplication with a local oscillator to extract the phase information from the 220 MHz signal obtained from the photodetector. Figure 2.2 depicts the control electronics utilized to implement this technique.

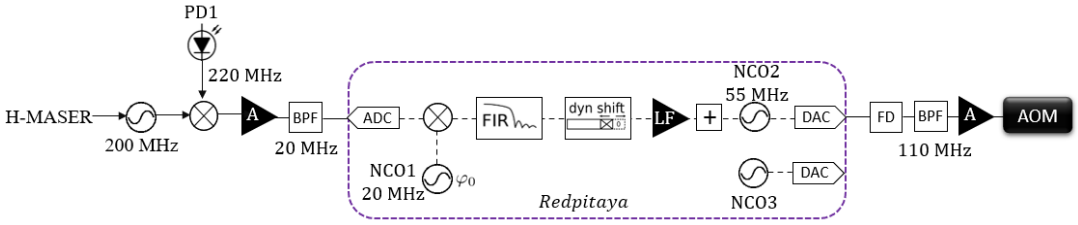

Figure 2.2: Schematic representation of the control electronics utilized for the fiber link. The system includes an active Hydrogen Maser (H-MASER), amplifier (A), Analog-to-Digital Converter (ADC), Digital-to-Analog Converter (DAC), numerically controlled oscillator (NCO), loop filter (LF), finite impulse response filter (FIR), frequency doubler (FD) and band pass filter (BPF).

The first stage of demodulation is analog, where the frequency is mixed with a 200 MHz signal generated by a direct digital synthesizer (DDS) that is referenced to an active Hydrogen Maser (H-

MASER). The signal from the DDS acts as a local oscillator. The resulting output of the mixer is a signal at a frequency of 20 MHz, which is significantly lower than the f_N of 62.5 MHz.

The frequency mixer generates undesired higher frequency components along with the desired frequency component. To eliminate these undesired components, the signal is filtered and amplified. This filtering process facilitates the acquisition of a clean 20 MHz signal with a power output of 11.6 dBm that is fed into the input connector of the Redpitaya.

Moreover, to ensure optimal signal transmission and minimize any signal loss or distortion, a 50 ohm load is included in parallel to the high-impedance ADC input. The board jumper is also positioned to the ±1 V full scale to achieve optimal signal transmission. The inclusion of the 50 ohm load and careful jumper positioning ensures minimal signal reflection and attenuation, thereby enabling the maximum transfer of energy from the source to the board.

We begin by sampling the input signal using a high-resolution ADC capable of providing 14-bit data resolution. Following the initial sampling, the signal undergoes a stage of digital demodulation, where it is subjected to multiplication with a 16-bit amplitude and a 40-bit phase accumulation register, implemented as a Numerically Controlled Oscillator (NCO). The NCO constitutes a phase reference φ_0. This demodulation process yields a 14-bit data stream, which carries the residual phase information of the input signal.

To filter the DC components of the demodulated signal and eliminate unwanted artifacts, we employ a Finite Impulse Response (FIR) filter. This digital filter is carefully configured with 25 coefficients, each precisely encoded as 16 bits. Its design specifications include a cutoff frequency of 4 MHz, effectively limiting high-frequency noise and interference, while ensuring the preservation of essential signal components. Remarkably, the FIR filter exhibits impressive rejection capabilities, surpassing 40 dB for frequencies beyond 14 MHz. The filter output consists of a refined 32-bit data stream, exhibiting enhanced fidelity and reduced noise.

To adapt the data stream from the FIR filter to subsequent processing stages, a dynamic shifter is introduced. This shifter enables the reduction of the data stream width from 32 bits to 14 bits, optimizing its compatibility with the loop filter and enabling the generation of an appropriately scaled correction signal. The dynamic shifter range is precisely adjusted to accommodate the desired bit reduction while preserving the critical information necessary for accurate phase correction.

The shifted data stream, now comprising 14 bits, is then forwarded to a loop filter (LF) equipped with a proportional-integrator function. The proportional and integrator values are carefully set to effectively suppress undesirable phase variations, thereby ensuring phase correction.

The LF output is integrated with a constant value to introduce a suitable bias to the frequency of the output DDS. The DDS, employing a second NCO, serves as the basis for generating the correction signal. By manipulating the DDS frequency, which is influenced by the LF output, we effectively control the phase correction process.

The generated correction signal is then routed to channel 1 of a high-performance DAC, which ensures reconstruction of the digital signal into its analog counterpart. In compliance with the Nyquist-Shannon sampling theorem, stringent requirements are imposed on the DAC to guarantee optimal signal reconstruction. Accordingly, f_N of 62.5 MHz is imposed by the board, necessitating the center frequency of the NCO to be set at 55 MHz, thus ensuring adequate bandwidth for faithful signal representation. The output of the DAC, carrying the reconstructed analog signal, undergoes frequency doubling using a dedicated frequency doubler.

To condition the frequency-doubled signal for its intended purpose, it undergoes filtering and amplification. The filtering stage ensures the removal of unwanted noise and spurious components, while the amplification stage boosts the signal power to achieve the necessary driving capability.

Finally, the filtered and amplified signal is utilized to drive an AOM. The AOM, operating in the optical domain, introduces the correction signal to rectify phase fluctuations in the fiber link. By applying precise control over the AOM, the correction signal effectively modifies the phase characteristics of the optical signal, aligning it with the desired phase reference.

In order to analyze and evaluate the impact of the digital phase reference on the lock performance, an additional DDS module is incorporated into the FPGA chip. This DDS module is based on a third NCO and its output is directed to channel 2 of the DAC. By utilizing this DDS module, the contribution of the digital phase reference to the lock performance can be precisely determined.

The Redpitaya embedded processor operates a GNU/Linux operating system. To cater to time and frequency metrology applications, we employ the oscimpDigital framework. With its user-friendly GUI, oscimpDigital allows for convenient control of processing blocks, parameter adjustment, resolution optimization, and precise PI controller tuning [128].

Direct digital demodulation with undersampling

To simplify the signal processing setup and avoid the need for an RF synthesizer and mixer at the output of PD1 (Fig. 2.1), we implemented the undersampling technique to directly extract the phase noise from the 220 MHz signal. The signal from the photodiode, after filtering, is directed to the input ADC (LTC2145) of the Redpitaya through a differential amplifier, which also serves as a low-pass filter, providing a bandwidth equal to half the sampling rate (62.5 MHz). However, the LTC2145 ADC has a much broader bandwidth of 875 MHz, exceeding the sampling rate.

To overcome this limitation and utilize the full measurement bandwidth of the Redpitaya, we made a modification to the Redpitaya board. We replaced the differential amplifier with a broadband RF balun, which acts as an RF transformer to convert the unbalanced signal into a balanced signal. The output signal from the RF balun was then directly connected to the input ADC. This modification involved adding three small wires from the RF balun output: two for the

differential outputs, labeled as V_{in}^{+} and V_{in}^{-}, and one for the reference voltage, labeled as V_{ref}. These three wires were directly connected to the input track of the ADC, bypassing the differential amplifier and removing the inductor located between the differential amplifier and the ADC.

The hardware implementation of the undersampling technique on the Redpitaya is illustrated in Fig. 2.3. This picture visually demonstrates the modified configuration and the connections involved in extracting the phase noise using the undersampling technique.

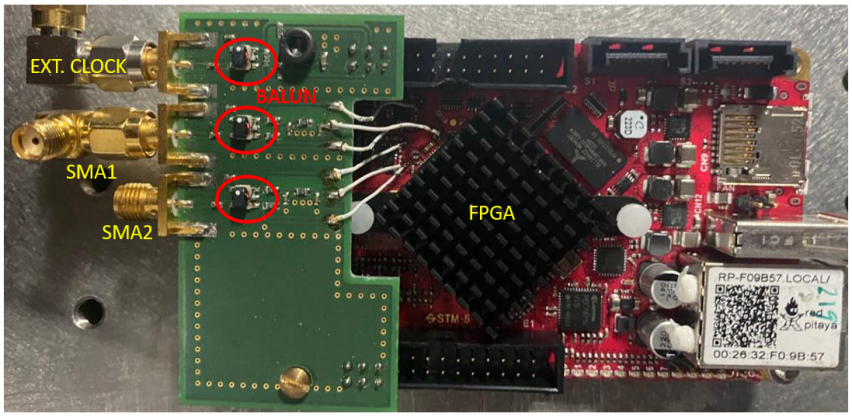

Figure 2.3: Hardware implementation of the technique of undersampling in a Redpitaya board where the red circles represent the broadband RF balun, EXT. CLOCK is the input for the external clock.

The updated control electronics scheme for the fiber link using undersampling is shown in Fig. 2.4.

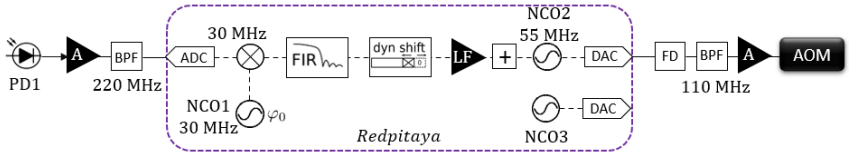

Figure 2.4: Control electronics scheme for undersampling setup of the fiber link.

When comparing Figure 2.2 and Figure 2.4, notable changes can be observed in the setup. Specifically, the frequency mixer and the 200 MHz signal from the H-MASER have been eliminated. Instead, the 220 MHz signal from the photodiode is now directly sent to the Redpitaya after undergoing amplification and filtering. In light of this modification, the filters have been replaced to accommodate the change in cutoff frequency, which has been adjusted from 20 MHz to 30 MHz. As a result, undersampling is employed, placing the system in the second Nyquist band of the input ADC. The frequency read by the Redpitaya is 30 MHz for an input frequency of 220 MHz with the clock frequency of 125 MHz.

Subsequently, we demodulate this aliased 30 MHz signal by providing a 30 MHz signal from the NCO. It is important to note that undersampling is solely implemented for the input ADC of the Redpitaya, while the remaining scheme remains consistent with what was discussed in

Subsection 2.4. Throughout the aliasing process, the phase noise is conserved. For further insights and results, please refer to Section 2.5. Additionally, for a more thorough understanding of the concepts of frequency aliasing and undersampling, please consult subsection 2.4.1.

Characterisation

To characterize the fiber link system, we utilize the out-of-loop signal. This signal, not directly involved in the main control loop, emerges at a frequency of 110 MHz. It's detected on PD2 due to the beatnote produced between the optical signal single pass through the link via a 110 MHz operating AOM and the signal from the laser output before entering the link. The electronic setup employed for characterization is shown in Figure 2.5.

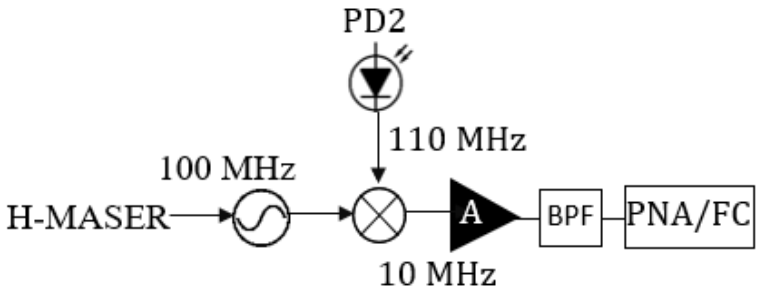

Figure 2.5: Control electronics scheme for the characterization setup of the fiber link, where PNA denotes the phase noise analyzer and FC represents the frequency counter.

The phase noise analyzer accurately measures the phase noise of the 110 MHz signal due to its wide bandwidth. However, our experiment frequency counter is limited to a 60 MHz bandwidth. To work around this limitation, we use a demodulation technique to lower the signal frequency. This demodulation process follows the same pattern as previously explained, except for substituting the 200 MHz signal from the synthesizer (which is synchronized to the H-MASER) with a 100 MHz signal. This results in a 10 MHz signal, which falls within the frequency counter bandwidth. This demodulated signal is then used for phase noise and FFS measurements.

2.4.3 Passive shielding

In the established optical configuration under discussion 2.1, several paths are identified as "uncompensated paths", namely those delineated by OC1-OC2, OC1-OC3, OC3-FM1, and OC4-OC2. These are termed as such due to the phase fluctuations that manifest in these paths and are not counterbalanced by the PLL. The aggregate length of this uncompensated path totals to 4.5 meters. As a consequence, this length poses a substantial limitation to the overall performance of the optical link, acting as a bottleneck to its optimal operation.

The proposed strategy to mitigate this challenge involves maintaining these paths in the utmost stable state attainable. One such solution that has been successfully implemented is

termed as "thermal shielding". This methodology revolves around the concept of passively reducing the noise that contaminates these paths. The entire optical setup, with the exception of the 15 meter long optical fiber, is positioned on a floating optical table for this purpose. A wooden box, that enclosed all the optical fibers on this table, functions as a protective shield against thermal and acoustic noise.

It is worth noting that these thermal and acoustic noises primarily originate from the room air conditioning system. This environmental factor can introduce undesirable perturbations into the optical setup, thereby compromising the stability of the uncompensated paths.

To further address the noise concern, an additional step involves strategic placement of FM2 in close proximity to OC2, while ensuring that both are connected via fibers of equivalent lengths. This configuration is based on the premise that slow fluctuating thermal perturbations will impact the two fibers concurrently and to a similar extent. In this manner, any phase shift in one fiber will be mirrored in the other, getting cancelled when the optical signals beat or interfere with each other after OC2 and thereby enabling a level of noise compensation. This simultaneity ensures that the output fiber perturbations are adequately matched and compensated for, thereby enhancing the stability and performance of the optical link.

Through these adjustments, our implementation seeks to effectively manage and counterbalance the phase fluctuations in the optical paths. By maintaining the stability of these paths and using both active and passive measures to reduce noise, we aim to improve the performance of the optical link and overcome the limitations imposed by the length of the uncompensated paths. The effect of passive shielding on the optical setup with the 15 m long fiber link, suspended over the optical table and the wooden box, is demonstrated by Fig. 2.6.

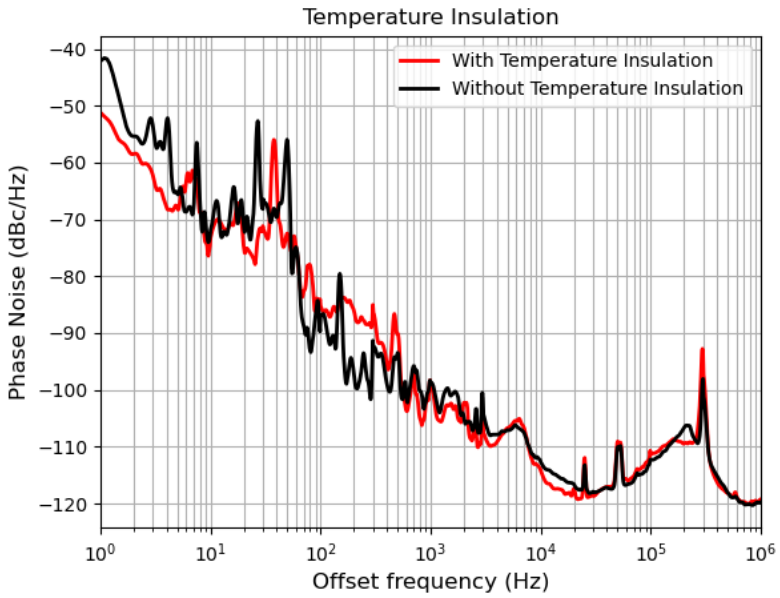

Figure 2.6: Black solid line : Phase noise spectrum of the link without temperature insulation. Red solid line : Phase noise spectrum of the link with temperature insulation.

The comparative data presented in Figure 2.6 provides valuable insight into the overall impact of the wooden box on the phase noise spectrum of the optical link. Here, the PSD of the link phase noise is evaluated both with the box (shown by the red solid line) and without it (shown by the black solid line). The data reveals that the phase noise profiles in both scenarios exhibit similarity, barring certain exceptions.

The major divergence is noticeable at lower frequencies, specifically below 10 Hz. At these frequencies, the wooden box presence seems to significantly reduce the influence of temperature fluctuations on the phase noise spectrum. This is evidenced by a gain of 9 dB at the 1 Hz Fourier frequency on the PSD when the box is employed. This enhancement suggests that the box effectively shields the optical setup from the effects of low-frequency thermal noise.

However, for frequencies greater than 60 Hz, the performance of the configuration with the box is similar to the configuration without the box. It is important to note that these measurements were conducted at different times of the day. Therefore, the origin of this noise remains uncertain. The only plausible explanation could be electronic noise originating from the PLL and optical noise arising from the uncompensated paths of the fiber link.

2.4.4 Use of stable external reference clock

In our experiment, the Redpitaya internal digital electronics operate using a local quartz oscillator, specifically the CXO BFBC90 model from TXC corporation, with a frequency of 125 MHz. To ensure high-frequency stability and low-frequency noise, it's essential to synchronize the system to a common low-noise oscillator.

A study in [129] reveals that quartz oscillators exhibit short-term stability around 10^{-9} to 10^{-10} and medium-term stability between 10^{-7} to 10^{-10}. Despite these characteristics, the stability of the Redpitaya embedded quartz oscillator, a type of CXO, fall short for effective implementation of PLLs due to the oscillator noise. Thus, achieving precise measurements necessitates substituting the built-in oscillator with a more stable external reference.

Figure 2.2 demonstrates that the phase fluctuations of a 20 MHz NCO are directly conveyed through the optical signal to the distant end of the link. This underscores the NCO pivotal role in maintaining system stability. Our experimental findings, concerning frequency stability and phase noise, highlight the adverse impact of the onboard quartz oscillator, employed as the board reference clock, on the fiber link stability. Consequently, we replace this internal oscillator with a steady 125 MHz clock signal produced by a DDS locked to an active H-MASER.

2.5 Experimental Results

In this section, we present the results that we obtained with the optical fiber link setup. The results include the residual phase noise affecting the fiber link and residual noise of the link in terms of FFS through Modified Allan Deviation (MDEV) for three different configurations that are :

1. stand alone board clocked by the internal quartz oscillator.
2. stand alone clocked by an external referenced clock *i.e.* a H-MASER.
3. using undersampling technique and the external reference clock.

Our investigation also aims to understand the influence of internal phase fluctuations (φ_0) of NCO1 on residual noise of the fiber optic link. These fluctuations directly affect the endpoint of the fiber link, posing a fundamental challenge to system performance and constraining the FFS. To assess performance under this constraint, we utilize another NCO (NCO3) integrated within the Redpitaya board, concurrently monitoring its output alongside the fiber link performance for real-time evaluation.

In the locked state, NCO1 operates at 20 MHz to digitally demodulate and extract the phase information from the incoming signal. As a result, the DDS of NCO3 is matched with this frequency of 20 MHz. In the unlocked state, the DDS of NCO3 is set at 55 MHz, that is the frequency of NCO2. Open-loop operation doubles NCO1 fluctuations, amplifying their impact, while closed-loop operation halves their impact through active adjustment. As a result, the NCO3 signals at 55 MHz and 20 MHz are plotted together for comparative analysis, multiplied by 2 and 0.5, respectively, and normalized to a carrier frequency of 194 THz.

Please note that the phase noise and FFS measurements represent distinct sets of data, conducted independently and under varying conditions. These measurements were not performed concurrently, and fluctuations in room temperature due to air conditioning were present

during each. Consequently, any direct conversion of values from phase noise to frequency noise may result in discrepancies.

2.5.1 Redpitaya clocked by internal quartz oscillator

We first measured the phase noise and the FFS of the fiber link using the Redpitaya clocked by the internal quartz oscillator. The measured phase noise spectrum is shown in Fig. 2.7.

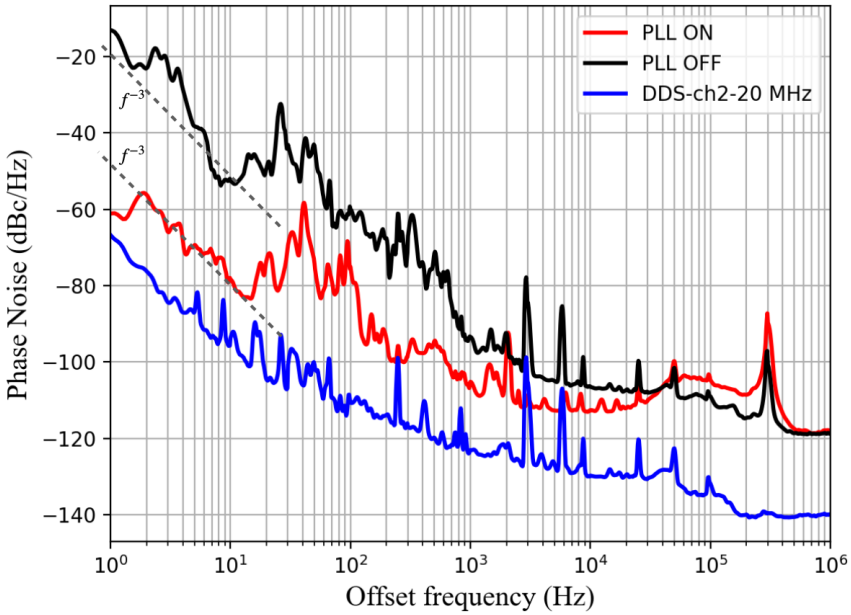

Figure 2.7: Graphical Representation of the PSD of phase fluctuations across different operational states of the optical fiber link. The black solid line corresponds to the free-running link. In contrast, the red solid line shows the phase noise spectrum corresponding to the 'locked' state of the link. The influence of the 20 MHz NCO input into the loop filter is given by the blue solid line.

In our experiment, we initially observed phase noise of -17 dBc/Hz at 1 Hz for the free running link with an f^{-3} slope until 10 Hz. However, upon engaging the PLL, we noticed a significant reduction in link phase noise given by -60 dBc/Hz at 1 Hz and -110 dBc/Hz at 10 kHz, with a lock bandwidth of 40 kHz. These findings demonstrate the effective noise rejection of the PLL for the link. It also signifies a noise spectrum gain of -48 dB at 1 Hz.

Analyzing the phase noise spectrum of the NCO, represented by the blue solid line, we observed a contribution of -67 dBc/Hz at 1 Hz at the output of the link. Scaling this to the Redpitaya internal quartz clock frequency, this corresponds to -33 dBc/Hz at 1 Hz for 125 MHz. These results align with the measured noise levels of the Redpitaya internal quartz oscillator, as documented by [129]. It confirms that the performance of the internal digital NCOs of the Redpitaya is entirely dependent on the clock source. Next, we examine the residual noise of the fiber link in time domain in terms of FFS using the Redpitaya internal quartz oscillator, as illustrated in Figure 2.8.

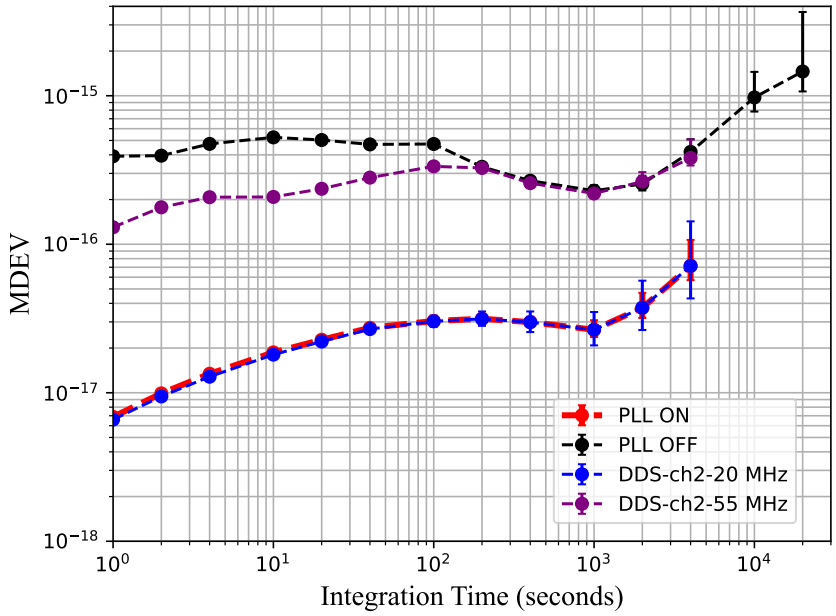

Figure 2.8: The figure represents the residual noise of the fiber link in terms of FFS in the time domain for different configurations through MDEV, represented by the following symbols: black dashed line for the free running link configuration, red dashed line for the locked link configuration, purple dashed line for the NCO with the link unlocked at 55 MHz, and blue dashed line for the NCO with the link locked at 20 MHz.

From the observations in Figure 2.8, we can analyze the FFS of different measurements. In the open loop measurements, we achieved a FFS of 5×10^{-16} at 1 second that is in accordance with the measured phase noise of -17 dBc/Hz in the frequency domain, which exhibits a plateau from 1 second to 100 seconds, followed by a gradual decrease in the curve until around the 2000 second mark. Beyond 2000 seconds, a linear frequency drift becomes evident for longer integration times.

Upon activating the PLL, we observe a significant improvement in FFS. With the PLL engaged, we achieve a FFS of 8×10^{-18} at 1 second. The FFS plot initially shows a $\tau^{1/2}$ slope, followed by a plateau until 1000 seconds. However, for longer integration times, a linear frequency drift is still present.

Based on the data in Figure 2.8, we can conclude that turning on the phase-locked loop reduces the link instability by a factor of 17 dB at 1 second corresponding to a 48 dB gain. The measured FFS of 8×10^{-18} at 1 second is in accordance of the measured link phase noise of -60 dBc/Hz at 1 Hz.

Additionally, when we analyze the FFS plots for the 55 MHz signal from the NCO (represented by the purple circles) and the FFS of the free running link, we observe an overlap from 200 seconds. This suggests that the DDS used to drive the AOM becomes a limiting factor for integration times longer than 200 seconds when the link is free running.

Similarly, when considering the FFS plots for the locked link and the 20 MHz signal (represented by the blue inverted triangles), we observe overlapping throughout the measurement. The

MDEV (See Section 1.2.5 of Chapter 1 to get an understanding about MDEV) plots of the link and the NCO overlap each other indicating that the phase reference (φ_0) of the DDS in the Redpitaya device is a limiting factor for the stability of the system.

2.5.2 Redpitaya clocked by external stable H-MASER

In order to enhance the performance of the link, we replaced the internal quartz oscillator of the Redpitaya with a 125 MHz signal generated by an RF frequency synthesizer. This synthesizer was clocked by an active H-MASER. Following this modification, we conducted a series of measurements to compare the performance of the link with the Redpitaya clocked by the internal quartz oscillator. These measurements were carried out under identical conditions to ensure a fair comparison. Results are shown in Fig. 2.9.

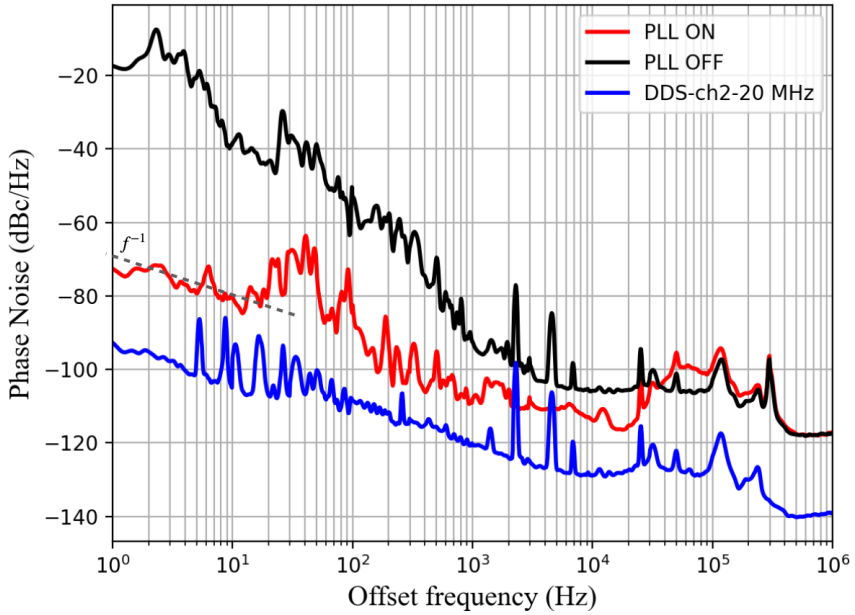

Figure 2.9: Phase noise for different link configurations with external clock. The black solid line represents the phase noise spectrum of the free-running link, while the red solid line represents the phase noise spectrum of the locked link. Additionally, the blue solid line depicts the phase noise spectrum of the 20 MHz NCO.

The phase noise analysis of the locked link demonstrates a substantial improvement compared to the free-running link which exhibits a phase noise of -17 dBc/Hz at 1 Hz (represented by the black solid line). Specifically, at 1 Hz, the phase noise of the locked link is measured at -72 dBc/Hz (depicted by the red solid line) corresponding to an MDEV of 9.14×10^{-19} at 1 second integration time , which is an impressive 55 dB lower than the phase noise of the free-running link and 20 dB lower than the configuration with the quartz clock. These results highlight the significant reduction in phase noise achieved through the implementation of the external clock signal.

To gain further insights into the factors contributing to this improved performance, we turn our attention to the phase noise spectrum of the 20 MHz signal generated by the NCO. Phase

noise of the NCO is considerably lower than that of the locked link. This observation implies that the NCO itself is not the limiting factor in achieving lower phase noise in this particular scenario.

Continuing our analysis, we measure the residual noise of the fiber link in the time domain in terms of FFS with the Redpitaya clocked to the stable H-MASER. This measurement, illustrated in Figure 2.10, provides valuable information about the residual noise present in the link under the influence of the H-MASER highly stable clock signal.

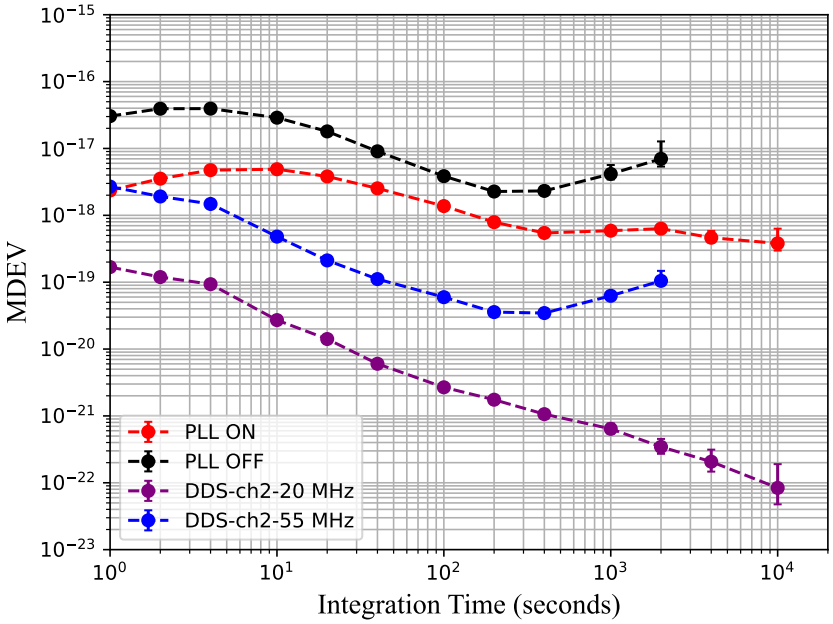

Figure 2.10: Comparison of the residual noise of the fiber link in terms of FFS in the time domain for different configurations through MDEV for different link configurations. The black dashed line represents the free-running link configuration, while the red dashed line depicts the locked link configuration. The purple dashed line corresponds to the FFS of the NCO with the link unlocked at 55 MHz. Finally, the blue dashed line illustrates the FFS of the NCO with the link locked at 20 MHz.

We have successfully achieved very low residual noise measured in terms of FFS with the PLL on. The measured FFS with PLL on, represented by the red dashed line in Fig. 2.10, reveals a result of 2×10^{-18} at 1 second integration time. It also exhibits a distinctive bump at 10 seconds, with a value of 8×10^{-18}. This bump indicates a temporary increase in frequency fluctuations within that time frame. However, for longer integration times, the stability of the locked link surpasses expectations, with values reaching below 10^{-18}. This is in stark contrast to the free-running link, which achieved a residual noise level in the time domain of 3×10^{-17}.

Furthermore, the FFS plots in Fig. 2.10 also shed light on the behavior of NCO in both the free-running and locked link scenarios. The FFS of the NCO for the free-running link is represented by the blue dashed line, while the FFS of the NCO in the locked link is depicted by the blue dashed line. The NCO FFS curves demonstrate that the NCO itself did not impose any significant limitations on the overall stability of either link configuration.

Moreover, within the PSD analysis of phase noise for the locked fiber link, we attained a

phase noise level of -72 dBc/Hz at a Fourier frequency of 1 Hz, equivalent to an MDEV of 9×10^{-19} at a 1-second integration time. However our recorded FFS was 2×10^{-18}. The difference can be explained by mostly electronic noise or optical noise arising due to the optical path length fluctuations of the uncompensated paths. Consequently, implementing adequate shielding for both electronics and uncompensated paths holds the potential to enhance overall system stability.

2.5.3 Redpitaya with undersampling

In this subsection, the results obtained through the application of the undersampling technique, as described in Subsection 2.4.2, will be presented. The methodology involved bypassing the antialiasing differential amplifier, which also functions as a low-pass filter, to directly route the 220 MHz signal from the photodiode to the input ADC of the Redpitaya. To fully exploit the ADC 875 MHz measurement bandwidth, a broadband RF balun was incorporated into the setup. Additionally, the Redpitaya was synchronized with an external H-MASER for clocking purposes.

By utilizing the undersampling technique, we achieved good results in terms of noise rejection as shown in Fig. 2.11.

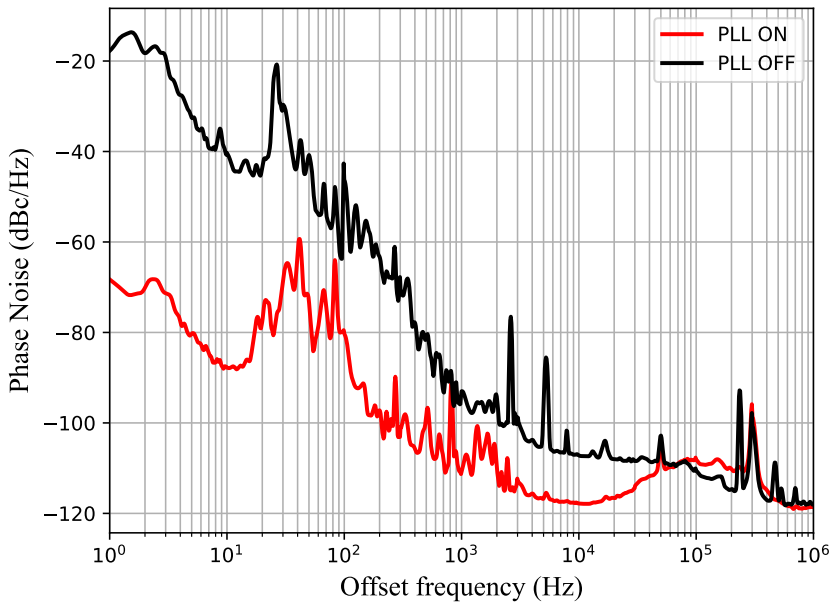

Figure 2.11: Comparison of phase noise spectra between the free running link (represented by the black solid line) and the locked link utilizing the undersampled Redpitaya (represented by the red solid line).

From Fig. 2.11, we can see that the locked link configuration achieved a very low residual phase noise level of -68 dBc/Hz at 1 Hz. This represents a significant improvement over the free-running link, where the residual phase noise measured at 1 Hz Fourier frequency was -17 dBc/Hz. This marks very low phase noise at low frequencies. At higher frequencies, the locked link continued to exhibit impressive noise reduction, with the phase noise reaching a floor of -110 dBc/Hz at

10 kHz. This noise suppression across the entire frequency range emphasizes the effectiveness of the undersampled Redpitaya in minimizing noise interference and maintaining signal integrity. It is important to highlight that the link performance closely aligns with that observed when employing an approach without undersampling, as discussed in the preceding subsection. The introduction of undersampling does not yield a noteworthy enhancement in performance. The current performance falls slightly below the previous measurements conducted with the H-MASER as the clock using the standard Redpitaya setup.

To further explore the performance of the undersampled Redpitaya, we examined the residual noise of the link in terms of FFS, as shown in Fig. 2.12.

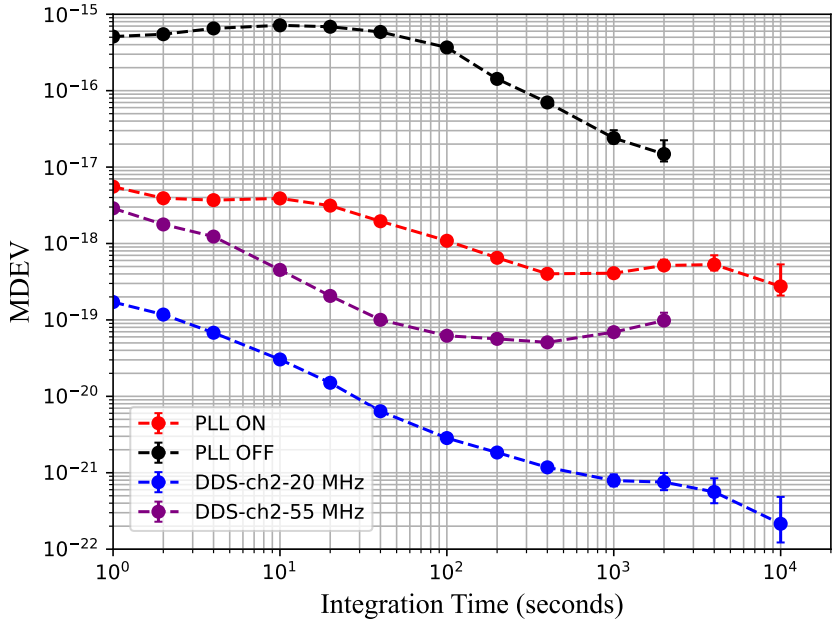

Figure 2.12: Representation of the residual noise of the link in time domain terms of FFS and using digital electronics clocked by an H-MASER and using the technique of undersampling. Black dashed line is the FFS for the free running link, red dashed line represents the locked link, purple dashed line represents the NCO at 55 MHz, and blue dashed line represents the NCO at 20 MHz.

The FFS for the locked link demonstrated a value of 6×10^{-18} at 1 second integration time. This is a significant improvement compared to the free-running link configuration, which exhibited an FFS of 4×10^{-16} at the same integration time. Notably, the FFS of the locked link exhibited a bump of 4×10^{-18} at 10 seconds, followed by a floor below 10^{-18}. By directly sending the 220 MHz signal to the Redpitaya without the need for a mixer to demodulate the signal to 20 MHz using another RF synthesizer, we effectively streamlined the setup while maintaining performance.The indication from the blue and purple dashed lines, which illustrate the NCO performance with PLL activated and deactivated respectively, suggests that the limitations are not imposed by the phase noise of the NCOs.

The success of the undersampling technique in our configuration highlights its efficacy

in achieving stable frequency transfers and reducing frequency fluctuations. This improvement is particularly significant in applications where compact setups are desired without compromising performance.

2.5.4 Comparison of three configurations

Next, we turn our attention to comparing the residual phase noise and the FFS of the three configurations discussed in Subsections 2.5.1 to 2.5.3. This comparative analysis will provide insights into the behavior of the link under different conditions. Specifically, we will focus on the configurations where the link was successfully locked. The results of the achieved residual phase noise for these locked configurations are presented in Fig. 2.13.

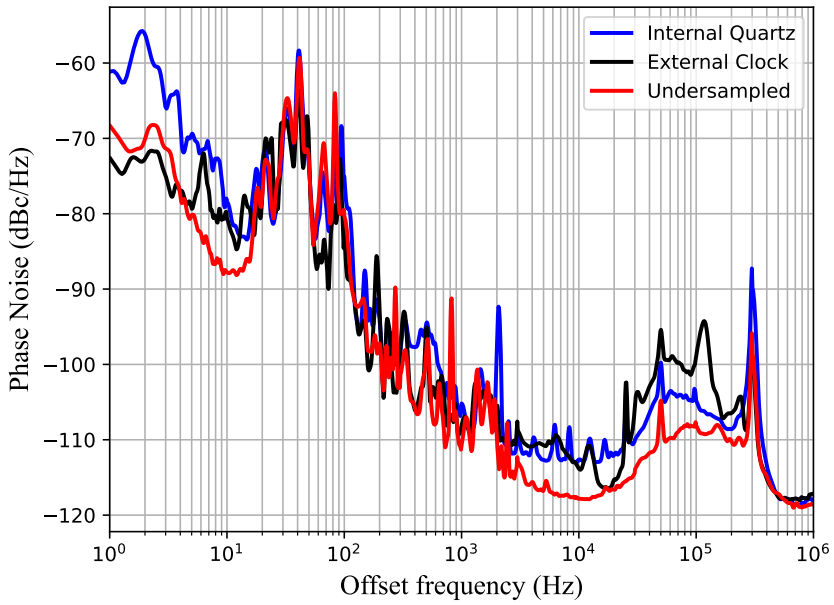

Figure 2.13: The phase noise spectra of the locked link are represented by the blue solid line for the configuration with the Redpitaya clocked to the internal quartz oscillator, the black solid line for the configuration with the Redpitaya clocked to the external stable H-MASER, and the red solid line for the configuration with the undersampled Redpitaya.

Based on the observations made in Fig. 2.13, it is evident that the link utilizing the Redpitaya clocked to the internal quartz oscillator exhibits the poorest performance among the three configurations. Conversely, the link locked with the externally clocked Redpitaya, without undersampling, demonstrates improved performance at 1 Hz. However, as the frequency surpasses 20 Hz, its performance becomes comparable to the undersampled Redpitaya configuration. Notably, for frequencies above 2 kHz, the link employing the undersampled Redpitaya showcases superior performance.

To further investigate the behavior of these configurations, we examine the FFS measurements, as depicted in Fig. 2.14.

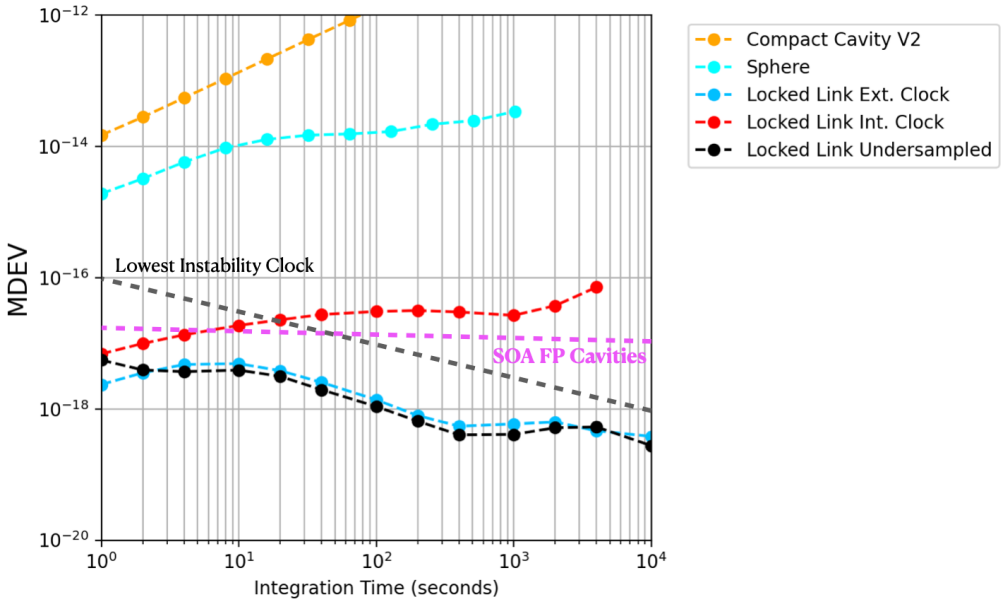

Figure 2.14: The figure displays a comparison of different configurations and their corresponding measurements. The red dashed line represent the FFS of the locked link with the Redpitaya clocked to the internal quartz oscillator. The blue dashed line correspond to the locked link with the Redpitaya clocked to an external stable H-MASER. The black dashed line depict the locked link with the undersampled Redpitaya. Additionally, the pink dashed line represents the FFS of state-of-the-art Fabry-Pérot cavities, while the grey dashed line represents the FFS of the state-of-the-art optical clocks.

Based on these measurements, we can conclude that using the stand-alone Redpitaya board is sufficient for carrying signals from ultra-stable Fabry-Pérot cavities with FFS in the range of 10^{-16}. However, for state-of-the-art Fabry-Pérot cavities and optical clocks represented by the pink dashed line and dark gray dashed line, respectively, the stand-alone board clocked to the internal quartz oscillator is not suitable. When an external clock is utilized for the Redpitaya board, the performance of the link demonstrates its capability to carry signals from state-of-the-art Fabry-Pérot cavities with fractional frequency stabilities of 10^{-17} and lower. The limiting factor in this case is the residual noise of the internal PLL [129]. According to [129], this PLL residual noise can be reduced by a factor of 2 by employing a 10 MHz reference signal, which would provide a link residual noise in terms of FFS of below 10^{-17} at 1 second.

Simultaneously, the undersampling technique yields excellent results, demonstrating its capability to transfer signals from state-of-the-art Fabry-Pérot cavities. Furthermore, comparing the FFS of the cavities within our department, such as the spherical cavity and the compact cavity, with the performance of the fiber link using the Redpitaya in its various configurations (orange and cyan curves), we can conclude that the fiber link with the Redpitaya is suitable for transmitting the optical signal from one room to another within our department while maintaining spectral purity and frequency stability.

2.6 Further Improvements

During the first one and a half years of my doctoral studies, I dedicated my efforts to designing and characterizing the optical fiber link. However, due to time constraints, we were unable to explore further enhancements to improve its performance. Nevertheless, there are several potential improvements that can optimize this fiber link:

1. Upgrading the Redpitaya: Initially, we utilized a 14-bit Redpitaya for implementing our digital PLL. However, there is now a commercially available 16-bit Redpitaya that offers improved resolution. Utilizing this upgraded version can enhance the overall performance of the link.

2. Extending undersampling technique: While we employed undersampling solely at the input of the Redpitaya, it is possible to implement undersampling at the output DAC as well. By doing so, we can directly send the 55 MHz signal to the AOM without the need for a frequency doubler. This approach avoids the introduction of noise associated with the frequency doubler, possibly enhancing the quality of the transmitted signal [130].

3. Consideration of polarisation maintaining fibers: Our current link design employed non-polarisation maintaining fibers. However, for applications involving polarisation-sensitive signal transfers, it is crucial to employ polarisation maintaining fibers. Making this switch will ensure the preservation of signal polarisation, resulting in improved performance.

4. Integration of a second AOM at the user end: To facilitate the marking of incoming and reflected optical signals, the incorporation of a second AOM can be highly beneficial. This additional component aids in distinguishing and managing the signals effectively, contributing to an optimized fiber link system.

5. Employment of a low noise power supply: We suspected that some part of noise observed in the optical signal could be attributed to the wall power supply provided by the company for the Redpitaya. Utilizing a low noise power supply, as detailed in Chapter 4 of the thesis, would effectively mitigate this issue. This improvement aims to reduce unwanted noise induced by the power supply, consequently enhancing the quality of the optical signal.

2.7 Compact electronics for optical fiber frequency dissemination

In this section, I will present the technique of ultra-stable frequency transfer from a laser locked to a Fabry-Pérot cavity over a 15 m long optical fiber between two rooms in our laboratory with a compact and transportable Doppler cancellation setup. First, I will give a description about the setup that will include the optical setup and the electronics setup. Then, I will present the results I achieved by transferring a signal from an ultra stable laser locked to a Fabry-Pérot cavity between two rooms through this fiber link setup.

2.7.1 Scheme

In order to build a compact setup we mounted the optical fiber components including the couplers, AOM, Faraday mirror, optical isolator and the electronics components for the digital PLL including the Redpitaya and RF components in a 19 inch rack mountable box. This box has dimensions of 88 mm×483 mm×466 mm (Height, Length, Breadth). We divide the box into three parts that are the optical part, the electronics part and the power supply part. This was done to separate the optical components from the electronics components to avoid any perturbations or stray noise from the active electronics. The scheme of the rack mountable box used to implement the Doppler cancellation setup is shown in Fig 2.15.

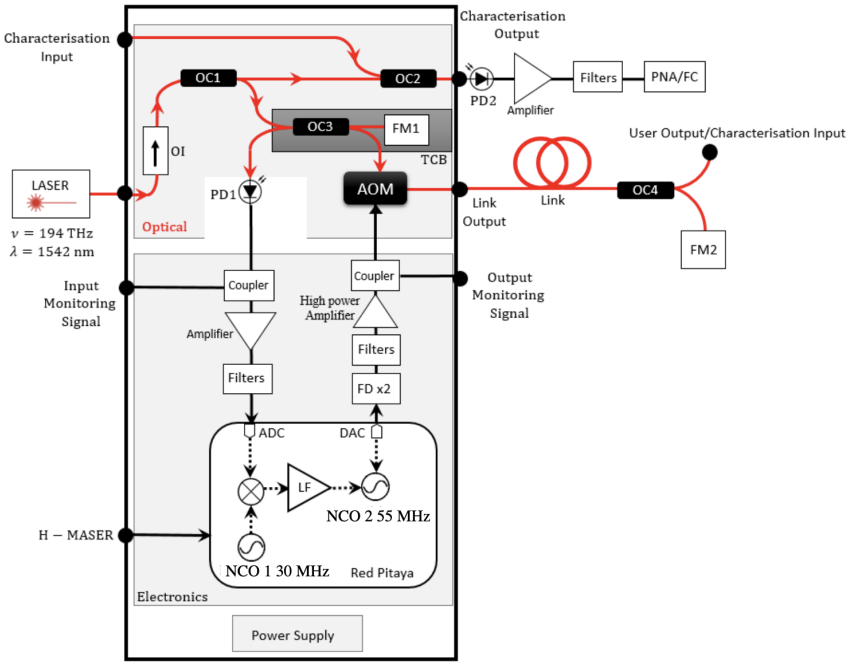

Figure 2.15: Scheme of a digital doppler cancellation setup in a 19 inch rack mountable, compact and transportable box. Red solid lines are optical signals; Black solid lines are RF signals; Black dashed lines are digital signals.

The optical setup employed follows heterodyne Michelson interferometry principles as discussed in Section 2.3, with a short arm between OC3 and Faraday mirror (FM1), and a long arm utilizing an AOM for controlled phase corrections. The AOM output connects to the fiber link front panel. The short arm, serving as a phase reference, is shielded from environmental effects through placement on a temperature-controlled breadboard, ensuring uniform temperature across the arm. At the remote fiber link end, signal extraction employs an output port of another optical coupler (OC4), and part of the signal returns via Faraday mirror (FM2).

To configure control electronics, we used the Redpitaya platform clocked by an active H-MASER incorporating a digital phase-locked loop for stable operation. Employing the technique of undersampling outlined in Section 2.4.2, we achieved a compact setup. The 220 MHz signal from photodiode PD1 underwent amplification, filtering, and direct input into the Redpitaya. The digital PLL corrected phase fluctuations, and the resulting correction signal was processed, filtered, amplified, and sent to modulate the optical signal using the AOM.

In order to assess the performance of the link, a dedicated characterisation input port has been incorporated on the front panel. This input port facilitates the characterisation process by utilizing a technique called "beating the laser against itself", as described in subsection 2.4.2. By connecting the user output to the characterisation input port on the front panel, a beatnote is generated at the modulation frequency of the AOM. This beatnote can be detected using a photodetector (PD2) and serves as a valuable signal for extracting and evaluating the link performance. The characterisation process involves analyzing various parameters and characteristics of the link based on the observed beatnote. Subsection 2.4.2 provides detailed information on this characterisation setup, offering insights into how the beatnote can be utilized to extract valuable performance metrics of the link.

To ensure optimal performance and minimize noise interference, the box incorporates its own dedicated low noise power supply distribution. A single external high current DC power supply is utilized to distribute the various voltages required by the different electronic components within the box. This distribution is achieved through a specifically designed PCB dedicated to efficient voltage management. The different electronic components within the box, including the photodiode, RF amplifiers, and temperature-controlled breadboard, receive their respective voltages through this dedicated voltage distribution system. By utilizing a dedicated PCB for voltage distribution, efficient and reliable power supply is ensured for each component, minimizing any potential voltage fluctuations or interference. In the case of the Redpitaya, which operates at a voltage rating of 5 V and current rating of 1 A, a compact and low noise power supply solution is employed. Specifically, TracoPower DC-DC Converters are utilized to provide the necessary power to the Redpitaya, ensuring stable and clean power delivery. This power supply setup, with its dedicated voltage distribution PCB and appropriate power supply solutions, plays a crucial role in maintaining the integrity and performance of the electronic components within the box, con-

tributing to optimal operation and minimizing potential noise-induced issues. The setup for the fiber link in a compact rack mountable box is shown in Fig. 2.16.

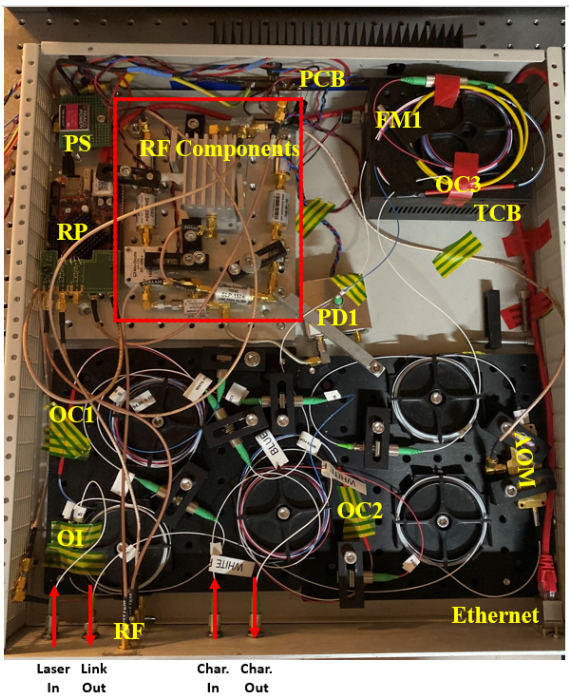

Figure 2.16: Optical fiber link control box where OI is Optical Isolator; OC1, OC2, OC3 are optical couplers; RP is Redpitaya; Char. is characterisation; FM1 is Faraday mirror; RF components include amplifiers, couplers, frequency doubler and filters (low pass and badn pass); AOM is Acousto Optical Modulator; PD is Photodiode; TCB is Temperature controlled breadboard; PS is power supply.

2.7.2 Experimental Results

In order to thoroughly characterize the performance of the optical fiber link, a phase noise measurement was taken with the digital PLL engaged. The power spectral density (PSD) of the phase noise over offset frequency is shown in Figure 2.17.

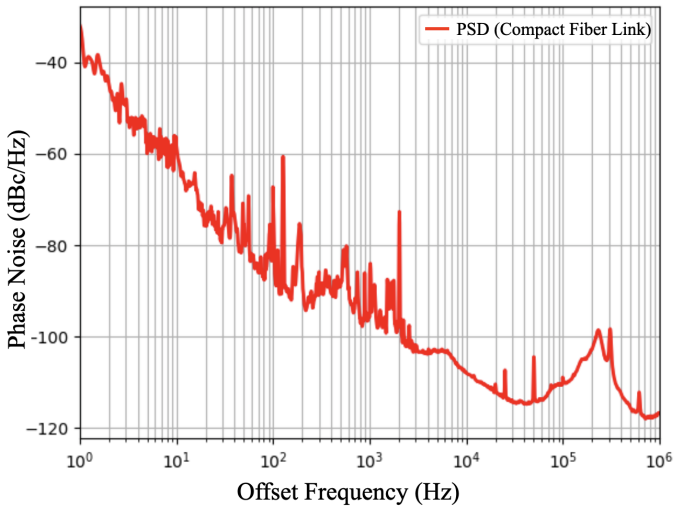

Figure 2.17: PSD of phase fluctuations versus the offset frequency of the compact optical fiber link setup.

The results show a link phase noise of -32 dBc/Hz at 1 Hz offset frequency when the PLL was engaged. When comparing this result to the phase noise measurements obtained in Figure 2.11, a difference of approximately 36 dB at 1 Hz offset frequency can be observed.

Several factors may contribute to the observed difference in performance between the compact fiber link setup and the laboratory-scale fiber link. For instance, the compact fiber link setup lacked thermal insulation as no wooden box was employed for isolation. Furthermore, the proximity of the electronics to the optical components and the potential for temperature fluctuations caused by the room air conditioning could introduce additional noise that may adversely affect the link performance. Please note that this setup needs further improvements and more optimisation which due to shortage of time was not possible during my doctoral studies.

Despite these potential sources of noise, it is worth noting that the main purpose of the compact fiber link setup was to transfer the frequency from an ultra-stable laser that boasts an FFS of 7×10^{-15} at 1 second. The compact fiber link was deemed adequate for this purpose, effectively maintaining the frequency stability of the ultra-stable laser signal.

Indeed, the compact fiber link setup was successfully utilized to transfer the signal from one of the ultra-stable lasers locked to a Fabry-Pérot cavity between two rooms through a 25 m long optical fiber link. More details can be found in Chapter 4 of my thesis.

2.8 Conclusion

This chapter of the thesis presents an in-depth exploration of the design, stabilization, and characterization of a laboratory-scale 15 meter long optical fiber link using the concept of heterodyne Michelson interferometry. The implementation of a full digital phase-locked loop using a commercial digital board in three different configurations was performed, including the use of

the board clocked with its internal quartz oscillator, and by an external stable clock signal from an active H-MASER.

The concept of undersampling was also demonstrated, which can be utilized to enhance the compactness of the control setup for the fiber link. The results achieved in the three different configurations were presented, and it was concluded that the internal quartz oscillator of the digital board is not sufficiently stable for metrological applications that require the transportation of an optical signal from an ultra-stable laser or atomic clock. In contrast, the fiber link demonstrated acceptable stability when clocked by an external stable clock signal, enabling the transportation of signals from state-of-the-art Fabry-Pérot cavities and optical clocks while preserving the spectral purity and frequency stability of the signal.

Several optimizations were implemented to enhance the stability of the fiber link, including thermal shielding utilizing a wooden box, and the use of a broadband RF balun to convert the unbalanced input to the ADC to a balanced input to maximize the full measurement bandwidth of the ADC of the control board. Additionally, a compact version of the fiber link was developed to locally transport the optical signal from the cavities in the department, while ensuring the preservation of frequency stability.

Overall, the study provides a thorough analysis of the design and characterization of optical fiber links, and the findings have implications for the advancement of stable fiber links for a wide range of applications. The design and characterization techniques presented in this study can be utilized to enhance the precision and stability of optical fiber links, rendering them more practical and effective for various applications in fields such as metrology, telecommunications, and sensing.

Chapter 3

USL based on a compact Fabry-Perot cavity

3.1 Introduction

This chapter documents the progress made during the second year of my doctoral studies, focusing on the development of a compact and highly stable laser setup designed by Alexandre Didier [131] and Séverine Denis. The setup involves a laser system frequency-locked to an ultra-stable, double tetrahedral-shaped spacer, compact ULE Fabry-Pérot cavity with a 25 mm optical length. This Fabry-Pérot cavity comprises two mirrors coated with reflective crystalline AlGaAs coatings for 99.997% reflectivity. Additionally, ULE rings placed atop the mirrors aid in compensating for the coefficient of thermal expansion (CTE) mismatch between the ULE spacer and Fused Silica substrates.

Beginning with a discussion on the Fabry-Pérot cavity design and geometry, the rationale behind selecting the tetrahedral shape, the compact vacuum chamber, and the specially devised cavity mount is highlighted. Following this, insight is provided into the optical and electronics setup used for achieving frequency stabilization, particularly the implementation of the Pound-Drever-Hall (PDH) frequency locking technique using digital electronics.

The subsequent section delves into characterizing the cavity, including measurements such as PSD of phase fluctuations, acceleration sensitivity, and CTE assessment. A discussion follows on the limitations identified with this cavity.

Concluding this segment, attention is directed toward the strategies employed to address encountered challenges while working with this cavity. Furthermore, potential avenues for enhancing the cavity performance are explored.

3.2 Design and Geometry

This cavity was designed and developed by Alexandre Didier [132]. The cavity design incorporates a double tetrahedral spacer, as shown in Fig. 3.1, along with a plano-concave resonator configuration featuring a 240 mm radius of curvature. This particular geometry was carefully selected to maximize cavity symmetries and minimize sensitivities to vibrations and accelerations across all coordinate axes.

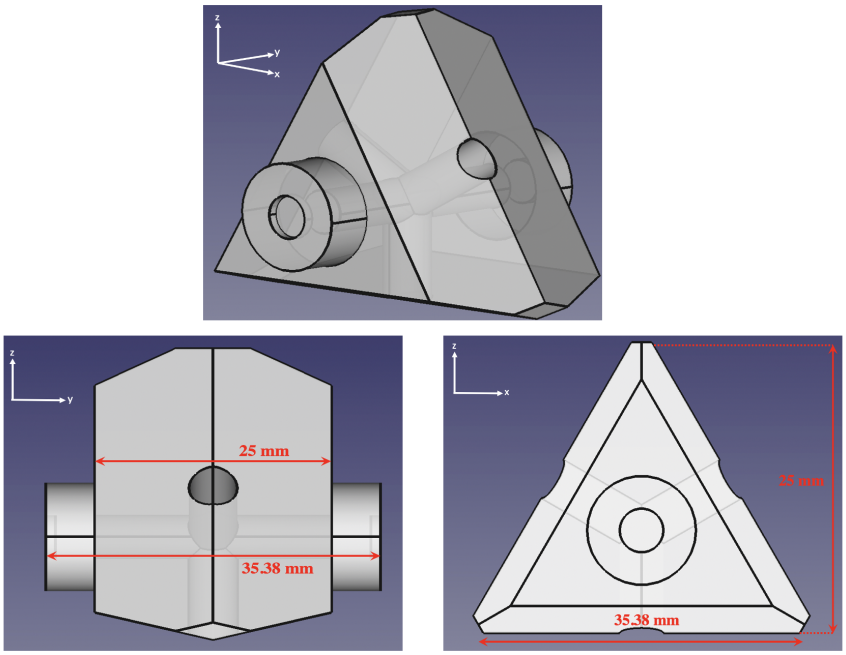

Figure 3.1: Design and geometry of the compact 25 mm Fabry-Pérot cavity based on a ULE spacer and a double tetrahedral design. The optical axis is along the y direction.

To ensure stable performance, the spacer, measuring 25 mm in length, is fabricated from Ultra Low Expansion (ULE) glass due to its negligible CTE. To achieve optimal optical performance, two Fused Silica (SiO_2) mirrors with highly reflective crystalline coatings made of GaAs/$Al_{0.92}$ $Ga_{0.08}$ As [56] are optically contacted to the spacer. These coatings are increasingly recognized for their significant advantages in reducing mechanical losses. These coatings offer an exceptionally low Brownian noise floor due to their high structural order and superior mechanical quality factors, reaching up to ten times lower loss angles compared to traditional ion-beam sputtered coatings. Furthermore, their high thermal conductivity helps dissipate heat efficiently, which is critical for minimizing thermal distortions during operation. Despite these benefits, birefringent noise arising from the intrinsic birefringence of the crystalline coatings remains a challenge. This birefringence can introduce polarization-dependent phase shifts, particularly in high-precision metrology applications, necessitating careful consideration in the design and use of these coatings [133–136].

The use of different CTE values for the ULE spacer and Fused Silica substrates introduces

a shift in the CTE zero crossing for the entire setup. To address this issue, 1 mm thick ULE rings with an inner diameter of 5 mm and an outer diameter of 12.7 mm are employed and contacted to the back of the mirrors. This configuration helps to achieve a CTE zero crossing near $11°C$ [35].

The cavity has a free spectral range (FSR) of 6 GHz and a linewidth of 24 kHz [132]. A high finesse of 247,000 at 1542 nm was measured using the cavity ring-down method.

The entire cavity is housed in a custom cubic vacuum chamber made of stainless steel. To maintain the compactness of the setup, the chamber is designed to hold free space optical components on its walls, with tapped holes serving this purpose. A conventional ion pump ensures efficient vacuum pumping within the chamber.

For passive shielding against thermal fluctuations, the cavity is surrounded by several layers of shields to maintain a constant temperature. Stainless steel was chosen to provide high thermal capacitance. The thermal enclosure consists of a central part to hold the cavity and two side parts for thermal shielding.

The cavity is supported by two Viton pads, each with a 2 mm diameter and 1 mm thickness, resting in 0.5 mm deep pockets on the bottom of the holder. Viton was selected for its mechanical damping properties and firm grip. A guided piston mechanism, operated by a top screw, provides the holding force on the cavity. This mechanism nullifies parasitic rotations during tightening, ensuring precise cavity positioning. The cavity-piston contact is facilitated by a 3.75 mm diameter Viton ball, effectively distributing contact force and dampening mechanical shocks.

A stainless steel enclosure is attached to a polished cubic copper shield. This copper enclosure acts as an active thermal shield, reducing the impact of thermal radiation from the external environment and maintaining a homogeneous temperature inside the chamber. To minimize thermal links, insulating materials are used for the screws and posts holding the copper thermal shield. A Peltier module placed at the bottom of the copper shield enables precise temperature control within the vacuum chamber.

The cavity is manually placed into the holding enclosure inside the vacuum chamber, and its alignment on the Viton pads is visually verified. The estimated position error on each support contact is 0.5 mm [137]. For reference, the cavity and its holder with the thermal enclosure are depicted in Fig. 3.2.

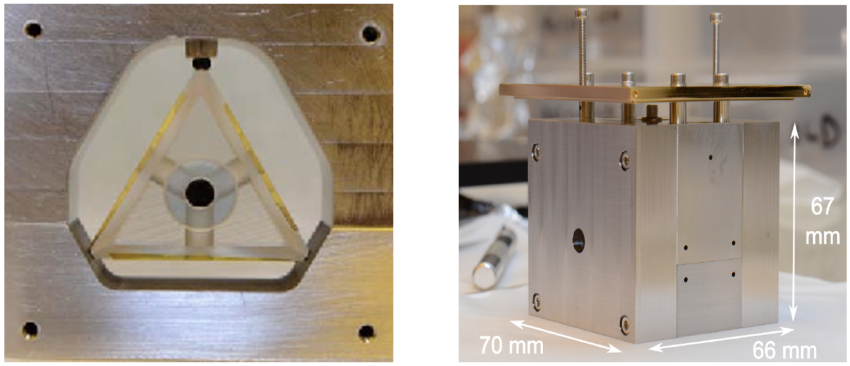

Figure 3.2: Left: cavity mounted in its stainless steel holder. Right: assembled stainless steel enclosure attached to the top of the copper shield.

3.3 Experimental Setup

3.3.1 Optical setup

The experimental scheme of the compact Fabry-Pérot cavity is shown in Fig.3.3.

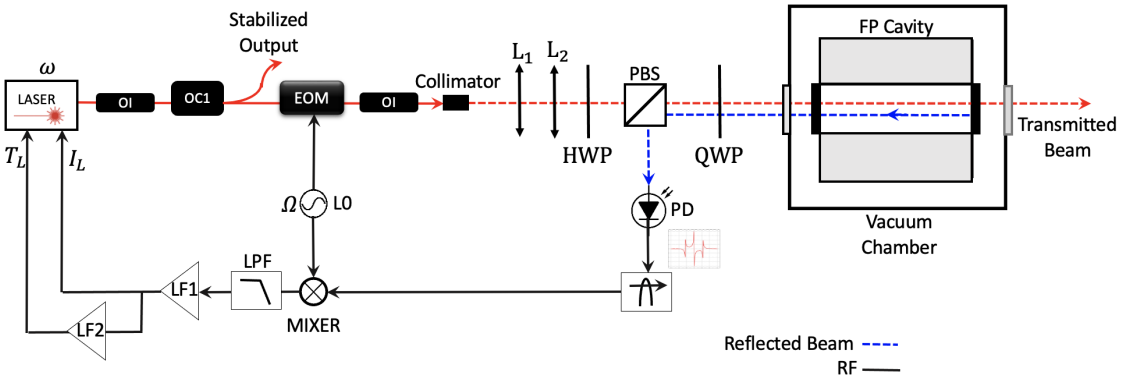

Figure 3.3: Scheme of USL based on compact Fabry-Pérot cavity : OI is optical isolator, OC is optical coupler, EOM is electro optical modulator, PD is photodiode, HWP is half wave plate, QWP is quarter wave plate, LF1 and LF2 are loop filters, LPF is low pass filter, LO is local oscillator, FR is Faraday rotator, T is transmitted beam, R is reflected beam, T_L and I_L are the temperature and current of the laser respectively.

We utilize a fibered external cavity laser diode, specifically the RIO PLANEX 1550 nm Laser Diode, as our laser source. This diode is a low-noise compact external cavity diode laser (ECDL) housed in a pigtailed butterfly case. To ensure precise control over the laser diode, we have integrated it into a custom 19-inch rack-mountable box. This box incorporates a highly stable current source and a digital temperature controller, facilitating precise control of the laser diode current and temperature. Additionally, the box features built-in channels for modulating the current and temperature of the laser diode.

The laser light is directed to a 90:10 fiber beam splitter (OC1) via an optical isolator (OI).

The OI serves the crucial function of preventing any back reflections into the laser from the beam path. Approximately 90 % of the optical power from the beam splitter is directed to the cavity via an Electro Optical Modulator (EOM), which modulates the beam at 30 MHz, generating sidebands around the carrier frequency. The distribution of optical power between the carrier and sidebands depends on the modulation depth, and only a fraction of the total power remains in the carrier after modulation. The remaining 10 % of the beam serves as the user output, providing access to the ultra-stable signal.

To preserve the optical integrity and stability of the system, we employ a second optical isolator after the EOM, followed by a fiber collimator. This second isolator serves to protect against any back reflections from the free-space components into the fibered part and reduces the creation of parasitic etalons that could degrade the laser frequency stability.

Cavity injection is achieved using free-space optical components. The beam from the optical fiber undergoes mode matching using two 1/2-inch lenses, followed by a half-wave plate, a polarized beam splitter and a quarter-wave plate to control the power of the incident beam and the acquisition of the signal reflected from the cavity. The light entering the cavity is circularly polarised. The beam is then directed using two 1/2-inch mirrors and injected into the cavity. We get a beat note signal that is detected via a fast photodiode at 30 MHz and serves as the error signal for the Pound-Drever-Hall locking technique [12]. The error signal undergoes digital electronic corrections, which are then transmitted to the laser via adjustments in its current and temperature. Fast frequency corrections are accomplished through controlling the current of the RIO laser diode, while slow frequency corrections are made by adjusting the laser diode temperature. The complete optical experimental setup with the vacuum chamber and the optical components is illustrated in Fig. 3.4.

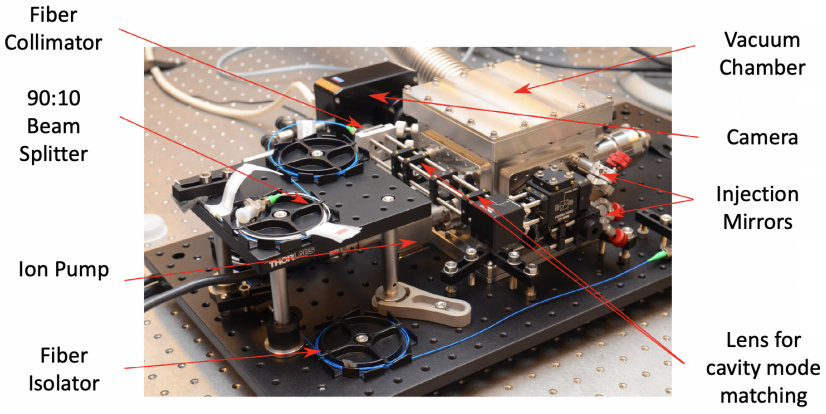

Figure 3.4: Optical setup for the compact Fabry-Pérot cavity. The vacuum chamber is on the right with the mounted free space components on its wall.

3.3.2 Control Electronics

The PDH scheme used to lock the frequency of the laser to the frequency of the cavity is implemented via a full digital electronics control scheme which is shown in Fig. 3.5. This fully digital scheme was designed and implemented by Séverine Denis.

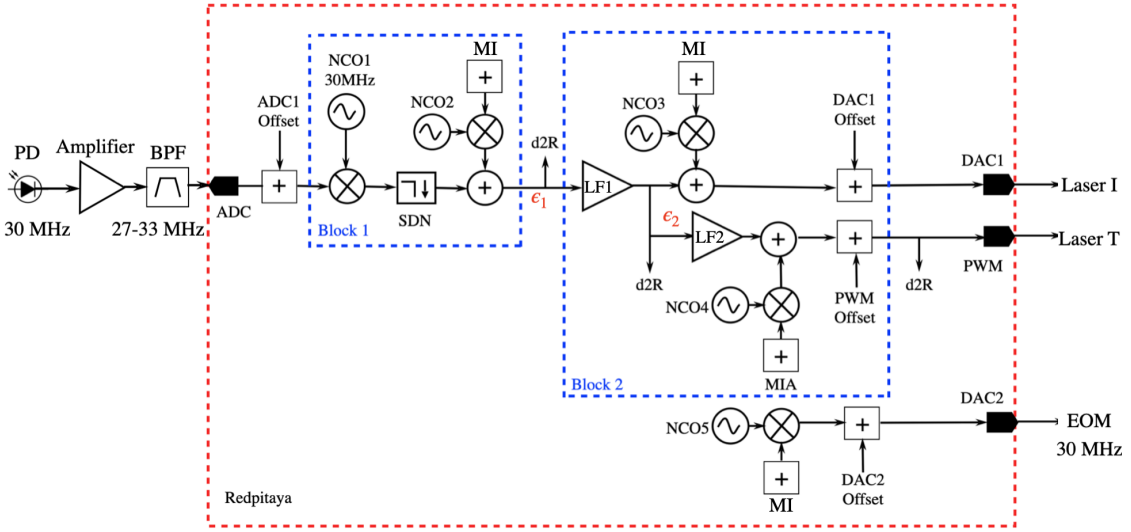

Figure 3.5: Control electronics for PDH laser frequency stabilisation technique where NCO is numerically controlled oscillator, LF is loop filter, ADC is analog to digital converter, DAC is digital to analog converter, BPF is band pass filter, PWM is pulse width modulation, d2r is data2ram, MI is modulation input, SDN is shift dynamic register and PD is photodiode.

A 30 MHz beat signal is detected using a fast photodiode. After amplification and filtering, the signal is fed into the RP input ADC. The 30 MHz signal, well within the RP measurement bandwidth and below its Nyquist frequency of f_N = 62.5 MHz, generates a 14-bit signal.

The 30 MHz signal is directed to block 1, serving to generate the error signal for PDH technique. Within this block, there's a setup comprising a digital mixer, two digital NCOs (NCO1 and NCO2), a finite impulse response (FIR) filter, and a shift dynamic register (SDN). NCO1 operates as the local oscillator, while NCO2 functions as a modulation NCO.

The generated error signal undergoes filtering through an FIR filter, resulting in a 32-bit datastream. Following the filtering process, the SDN simplifies the 32-bit signal by reducing its size down to a 14-bit signal.

The error signal generated from block 1, progresses to block 2 for the derivation of a correction signal. This block incorporates two loop filters, LF1 and LF2, integrating proportional (P) and integrator (I) functions. Precise adjustments of these parameters yield a correction signal sent to DAC1 of the RP. This correction analog signal, upon exiting DAC1, directly interfaces with the laser current controller. This interaction fine-tunes the current until resonance is achieved, effectively aligning the laser frequency with that of the cavity—a process referred to as fast laser frequency corrections.

However, prolonged operation results in the gradual drift of the laser current, leading to undesirable power fluctuations. To counter this issue, LF2 comes into play, utilizing the error signal (ϵ_2) provided by LF1. LF2's objective is to maintain ϵ_2 at zero by modulating the laser temperature. The output of LF2 is then employed as the correction signal for the laser temperature. This signal is channeled through the pulse width modulation (PWM) port of the RP, ultimately reaching the laser temperature modulation input, ensuring sustained stability and addressing the long-term fluctuations arising from the laser current drift.

In addition to frequency locking, we also use the RP to determine the cavity transmission mode by adding modulation to the laser current and temperature, shifting the laser frequency through the Fabry-Pérot cavity free spectral range while keeping the PDH loop open. When the laser frequency is in resonance with the cavity frequency, a transmission occurs, generating an error signal. This modulation to the current and temperature of the laser is achieved via two other NCOs (NCO3 and NCO4) while the PDH loop remains open.

The RP's fifth NCO (NCO5), serves the purpose of creating the modulation frequency for the EOM, delivering it via the second RF output of the RP. The resultant EOM modulation signal, emerging from DAC2 of the RP, undergoes proper filtering and amplification to reach a power level of 12 dBm.

3.4 Characterization

This section provides an overview of the measurements conducted to analyze the cavity during the second year of my thesis. Prior to my involvement in the PhD program, Séverine Denis and Jacques Millo conducted measurements where a CTE zero crossing was not observed. Simultaneously, the measured phase noise and fractional frequency stability exceeded the anticipated values. Consequently, I dedicated the second year of my thesis to investigating the absence of the CTE zero crossing. This involved performing FEM simulations by Guillaume Le Têtu, and conducting theoretical calculations. Simultaneously, efforts were made to optimize electronics to minimize phase noise. This section provides an overview of these measurements and calculations.

3.4.1 Phase noise

The PSD of phase noise for the USL was assessed by creating a beatnote between the laser locked to the compact cavity and a telecom laser locked to a spherical cavity with an FFS of 2×10^{-15} at 1 second integration time. The performance of the spherical cavity surpassed that of the compact cavity, aiding in the determination of the phase noise of the compact cavity. In Figure 3.6, we present a comparison of the phase noise of the compact cavity with respect to the spherical cavity for two configurations:

1. PSD of phase noise of USL with analog PDH locking scheme as measured by Alexandre Didier [131].

2. PSD of phase noise of USL with fully digital FPGA based PDH locking scheme.

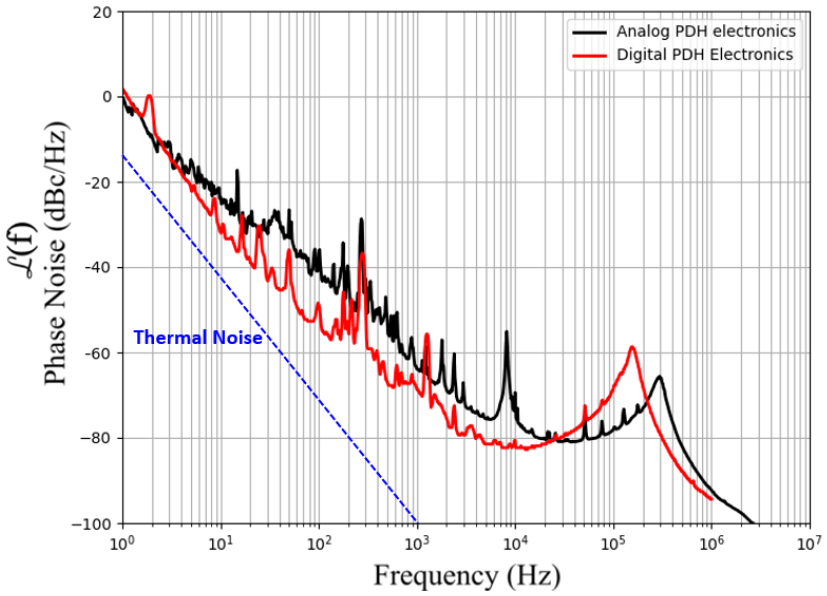

Figure 3.6: Comparison of phase noise spectrum of the compact cavity for two configurations: Red solid line represents the phase noise spectrum of the compact cavity using fully digital PDH locking scheme; Black solid line corresponds to the PSD of phase noise spectrum of the compact cavity using analog PDH locking scheme; Blue dashed line indicates the cavity thermal noise limit.

With the utilization of the PDH frequency locking scheme, the analog electronics achieved 0 dBc/Hz at a 1 Hz offset frequency, displaying a slope of f^{-2} in between 3 Hz and 3 kHz (solid black line). Transitioning to a digital control system using the RP resulted in a phase noise of 3 dBc/Hz at a 1 Hz offset frequency, displaying a slope of f^{-3} in between 1 Hz and 30 Hz.

While the analog scheme outperforms the digital counterpart at 1 Hz offset frequency, the digital system exhibits notably lower phase noise beyond 3 Hz. Notably, in terms of slope, the analog method follows an f^{-2} characteristic corresponding to white frequency noise potentially originating from the electronic frequency-control loop [132] , whereas the digital method demonstrates an f^{-3} trend corresponding to flicker frequency noise. The shift from an analog to a digital setup effectively mitigates this white frequency noise, moving the system closer to adhering to the cavity thermal noise limit.

It's essential to note that the analog electronics measurement was conducted with the guiding screw fully tightened, securing the cavity firmly through the viton ball. Contrastingly, during the digital setup measurement, the guiding screw was loosened, allowing the cavity to rest solely on the viton pads. This adjustment potentially contributed to improving the phase noise curve slope from f^{-2} to f^{-3}, indicating that proper force adjustment for cavity stability might aid

noise reduction.

3.4.2 Acceleration sensitivity

The Fabry-Pérot cavity was designed with a double tetrahedral geometry to minimize vibrational sensitivities. The cavity is supported by a non-hyperstatic three-point holding system, which ensures balanced forces and effectively eliminates x and z axis translations. FEM simulations confirmed very low acceleration sensitivities, below 10^{-12}/m.s^{-2}, in all three directions [132].

For acceleration measurements, a dedicated setup was constructed. The vacuum chamber with free-space optical components was mounted on its walls, and pigtailed fiber components were placed on a thin breadboard supported by four sorbothane mounts at its corners. This assembly was further placed on an active vibration isolation platform capable of modulation in all axial directions from 0.1 Hz to 200 Hz. The entire setup, along with the laser and control electronics, was placed on an optical table designed to shield against ground vibrations.

Jacques Millo from the TF department conducted the acceleration sensitivity measurements. To calculate the acceleration sensitivity coefficients $k_{x,y,z}$, sinusoidal modulation was applied to the active isolation platform, and the corresponding acceleration noise spectrum S_{a_i} and phase noise spectrum S_ϕ were measured. Accelerations of 10^{-4} m/s^2 were applied at frequencies of 2 Hz and 6 Hz. The resulting acceleration sensitivities are presented in Table 3.1.

Axis	Acceleration Sensitivity at 2 Hz	Acceleration Sensitivity at 6 Hz
x	1.5×10^{-11} /m.s^{-2}	1.2×10^{-10} /m.s^{-2}
y	8.7×10^{-12} /m.s^{-2}	7.7×10^{-10} /m.s^{-2}
z	1.1×10^{-10} /m.s^{-2}	1.9×10^{-10} /m.s^{-2}

Table 3.1: Acceleration sensitivity in three directions (x, y and z) measured at 2 Hz and 6 Hz [132].

From Table 3.1, it is observed that the measured acceleration sensitivities were significantly higher than those obtained through FEM simulations. Particularly, for the z-axis, the measured acceleration sensitivity at both frequencies was on the order of 10^{-10}/m.s^{-2}, much higher than the FEM simulation values of 10^{-12}/m.s^{-2}. For a white acceleration noise level of 95 dBm^{2}s^{-4}/Hz, the vibration noise contributing to the fractional frequency noise would reach 1.4×10^{-15} in a quiet environment. This is very close to the previously calculated theoretical thermal noise limit of 1×10^{-15}. In a noisy environment, the vibration noise may become a limiting factor for the frequency stability. The absence of a free-space optical isolator in the optical path is suspected to allow the formation of parasitic etalons. These etalons are caused by unwanted reflections between optical surfaces, and their interference patterns are highly sensitive to shifts in the optical path length. When vibrations occur, they can cause these surfaces to move, altering the path length and modulating the laser's frequency.

3.4.3 Coefficient of thermal expansion (CTE)

The CTE measurements were carried out by Séverine Denis. As direct measurement of the cavity length change is not feasible, we resorted to monitoring the change in frequency, which corresponds to relative length variations. This was achieved by locking the laser to the cavity using the PDH technique. Subsequently, the laser frequency was measured at small temperature intervals within the vacuum chamber, generating data points that were plotted against temperature.

The primary objective of this analysis was to identify the temperature at which a fitted line through the data points crosses zero, indicating the inversion point or zero crossing temperature of the cavity, where relative length variations become null. The measurement of the cavity CTE provides valuable insights into its thermal behavior and aids in the design and optimization of the cavity performance. The obtained results are shown in Fig. 3.10.

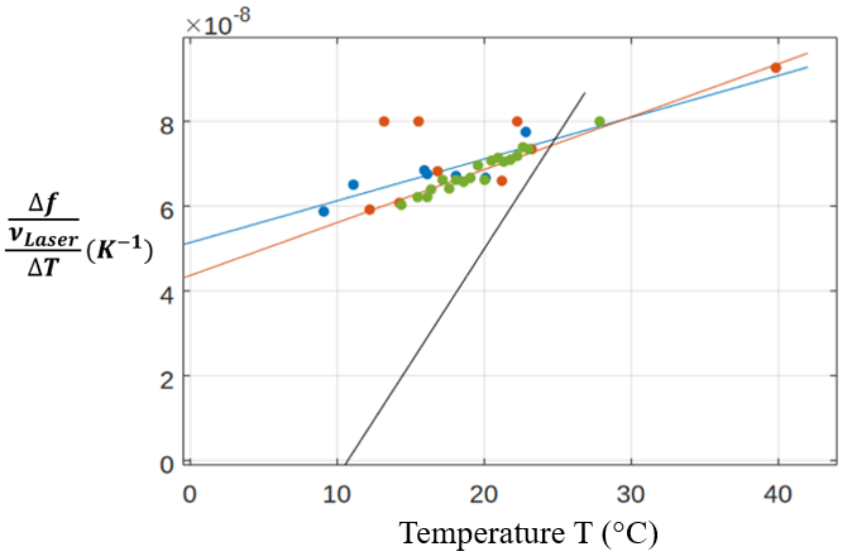

Figure 3.7: CTE ($\frac{\Delta f/\nu_{Laser}}{\Delta T}$) versus temperature under different configurations for the cavity measured by Séverine Denis and Jacques Millo. The first set (orange points) represents measurements with the cavity resting on viton pads and secured by a viton ball applying force via a guided screw. In the second set (blue points), the applied force was reduced by slightly loosening the screw to examine the effect of lower force on the cavity. The third set (green points) shows measurements with the screw completely removed, allowing the cavity to rest solely on the viton pads, assessing the thermal response with no additional force. The black solid line represents the expected behaviour of the CTE of the cavity.

The CTE measurements were conducted using three different configurations to thoroughly analyze the cavity thermal behavior. In the first set of measurements shown by the orange points, the cavity was positioned as desired, resting on the viton pads, and securely held in place by applying a specific force from a viton ball through a guided screw.

For the second set of measurements shown by the blue points, the force applied from the top through the viton ball was slightly reduced by loosening the screw. This allowed for the examination of the cavity response to a slightly different level of force exerted on it.

Finally, in the third configuration shown by the green points, the guiding screw was completely removed, and the cavity was allowed to rest solely on the viton pads. This configuration aimed to assess the cavity thermal response when there was no additional force applied from the guiding screw.

Upon examining the measurements from the three configurations depicted in Fig. 3.7, it becomes evident that there is an absence of a CTE zero crossing at room temperature, contrary to the expectation derived from FEM simulations. Extrapolating fitted lines through the data points reveals that the zero crossing temperature lies significantly below 0°C. Several potential explanations exist for the failure to obtain the zero crossing, including:

1. FEM simulations yielded inaccuracies in replicating the effective CTE for the composite material cavity.

2. A spacer made from ULE with different intrinsic characteristics is being used causing a considerable shift of T_0 towards a significantly lower temperature.

3. The spacer could be composed of Zerodur, a material frequently used in the construction of Fabry-Pérot cavities. While Zerodur shares similarities with ULE material, particularly in exhibiting a CTE zero crossing near room temperature, we assume Zerodur has either a very small or significantly high zero-crossing temperature. This allows us to approximate its CTE as a constant value over the relevant temperature range.

4. The cavity holder, composed of stainless steel, could potentially contribute to the absence of the zero crossing phenomenon. This could stem from the material's inherent thermal expansion and contraction in response to temperature fluctuations.

5. A substantial temperature difference exists between the peltier's temperature and the actual temperature of the cavity. This disparity arises due to the presence of two shield layers, and the absence of a sensor to gauge the precise temperature within the cavity.

The hypotheses outlined in points 1, 2, and 3 can potentially find resolution through the construction of a new cavity incorporating a ULE spacer with a precisely controlled intrinsic CTE. Furthermore, addressing the hypotheses detailed in point 4 involves the fabrication of a new cavity holder utilizing INVAR, renowned for its minimal thermal expansion characteristics. These strategies have been systematically implemented and documented in Chapter 4 of my thesis.

To address the concern raised in point 5 regarding temperature monitoring accuracy, a viable solution involves the installation of a temperature probe within the innermost shield of the cavity holder. This measure ensures a more precise monitoring of the cavity temperature dynamics.

Within this chapter, particular emphasis has been placed on an examination of point 3. This involved conducting FEM simulations and thermal noise calculations, documented in the

subsequent sections to determine whether the cavity spacer material is constructed from ULE or zerodur.

3.4.4 Thermal Expansion through FEM simulations

To investigate the absence of a CTE zero crossing in the Fabry-Pérot cavity, the initial step involved determining the material composition of the spacer, whether it is ULE or Zerodur, using FEM simulations. Guillaume Le Têtu from the TF department conducted these simulations using COMSOL Multiphysics with the Structural Mechanics and Thermal Stress modules.

Selection of geometry and parameters for simulation

The simulations involved two distinct configurations:

1. Spacer made from ULE with Fused Silica Mirrors and ULE rings.
2. Spacer made from Zerodur with Fused Silica Mirrors and ULE rings.

These simulations were undertaken to gain insight into the material composition of the cavity spacer and to determine whether Zerodur aligns with the observed behavior in the experimental CTE plot. In order to ascertain the exact material from which the spacer is composed, we aimed to simulate the two aforementioned configurations and subsequently plot the relative length variation ($\frac{\Delta L}{L}$) of the cavity against temperature (T). This comparison of results would provide us with theoretical insights. The simulation variables considered for these analyses are detailed in Table 3.2.

Property	ULE	Zerodur	Fused Silica	Viton
Young's Modulus (Pa)	67.8×10^9	90.3×10^9	73×10^9	3.5×10^6
Poisson's Ratio	0.17	0.24	0.16	0.4
Density (kg/m^3)	2210	2530	2202	1600
H.C. (J/(kg.K))	767	800	772	1600
T.C. (W/(m.K))	1.31	1.46	1.38	0.25
CTE (1/K)	Variable	41.9×10^{-9}	5.1×10^{-7}	70×10^{-6}

Table 3.2: Parameters for FEM simulations, where H.C. represents the heat capacity at constant pressure, T.C. denotes the thermal conductivity, and CTE stands for the coefficient of thermal expansion.

To streamline the simulations, we imposed fixed constraints on the viton pads within the software, thereby restricting their movement in any direction. Fused Silica materials possess constant CTE within the temperature range of 0°C to 50°C. ULE exhibits a parabolic response, reaching zero thermal expansion at a specific temperature, after which it inversely rises. Our primary objective is to identify this inversion point, commonly referred to as the zero crossing. To achieve this, we assigned constant CTE values for components made from Zerodur and Fused Silica. However, for ULE components, we treated the CTE as a variable, ranging from 0°C to 50°C, with an anticipated

inversion point temperature (T_0) set at 25°C. We calculated the relative length variation for the ULE spacer concerning temperature change using the equation:

$$\frac{\Delta L}{L} = \alpha_{ULE}(T)\Delta T \tag{3.1}$$

where,

-ΔT is the change in the temperature,

-$\alpha_{ULE}(T)$ are the CTE values for ULE.

$\alpha_{ULE}(T)$ is given by the equation

$$\alpha_{ULE}(T) = a(T - T_0) \tag{3.2}$$

where,

-a=2.49×10^{-9} K^{-2} [25].

To determine the relative length variation ($\frac{\Delta L}{L}$) with the change in temperature (T), we chose two points P_0 and P_1 on the centre of the two mirrors respectively. We define the displacement components (u,v,w) along the x,y and z axes of these two points as (u_0, v_0,w_0) for P_0 and (u_1, v_1,w_1) for P_1. The optical axis is y. The positions of P_0 and P_1 are shown in Fig. 3.8.

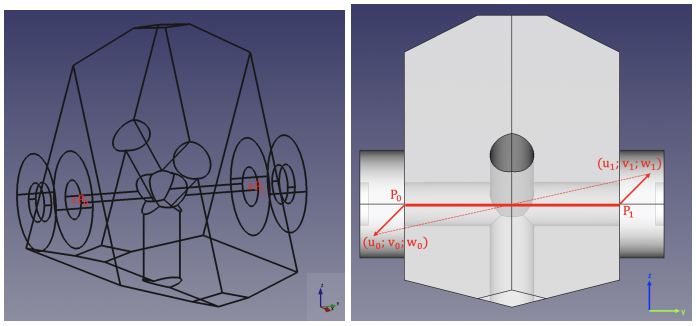

Figure 3.8: Points under consideration for relative length fluctuations due to change in temperature

To estimate the deformation of the cavity due to the mirrors, superposition of translations along x, y and z axes and rotations across x and z axes are considered. But according to [131], translations along the x and z axes are negligible and does not influence the optical axis that is the y axis of the cavity. Relative length variations are given by the equation

$$\frac{\Delta L}{L} = \frac{\sqrt{(u_1 - u_0)^2 + (L + v_1 - v_0)^2 + (w_1 - w_0)^2} - L}{L} \tag{3.3}$$

where,

- $L = 25$ mm is the length of the cavity.

Since we are considering negligible effects from the translations across x and z axes, the relative

length variation due to the y axis is given by the equation

$$\frac{\Delta L}{L} = \frac{v_1 - v_0}{L} \tag{3.4}$$

Simulation Results

Simulations were conducted across temperatures from 0°C to 50°C, incrementing by 0.5°C. In Figures 3.9(a) and 3.9(c), stress and displacement maps, respectively, for the ULE spacer at 0°C and 50°C are depicted.

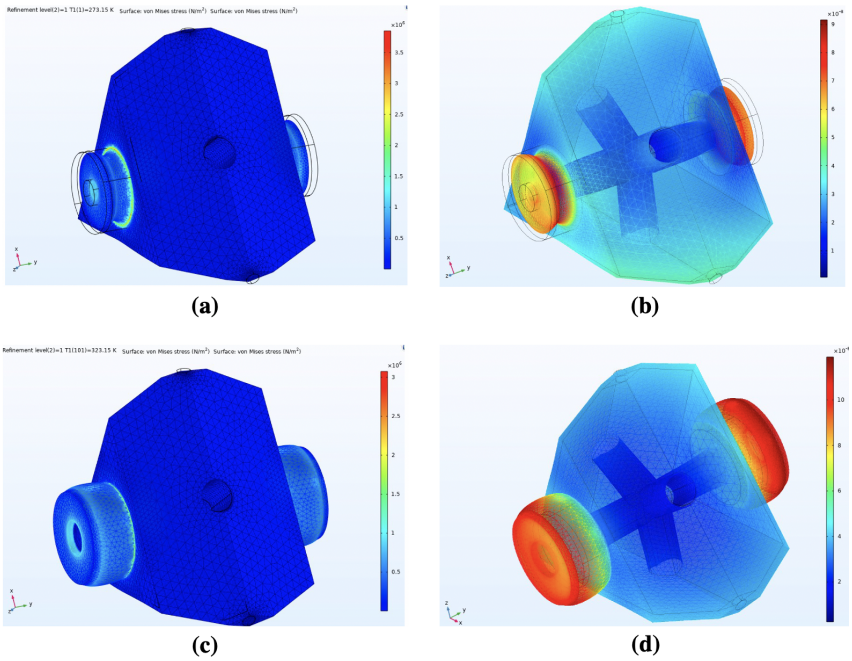

Figure 3.9: Stress and displacement map for 0°C and 50°C for cavity made of ULE spacer : (a) & (b) stress and displacement map at 0°C respectively; (c) & (d) stress and displacement map at 50°C respectively.

In examining the stress maps (Figures 3.9(a) and 3.9(c)), it's clear that stress affects the fused silica spacer junction, aligning with expectations. Stress increases notably at 50°C. These simulations aimed to highlight that only the fused silica mirrors exhibit length variations with temperature changes. The displacement maps (Figures 3.9(b) and 3.9(d)) also reveal maximum displacement within the fused silica domain. Notably, these results remained consistent even when applying gravitational force, confirming its negligible impact on length variations in response to temperature changes.

Similar observations were made with a Zerodur spacer. The fused silica domain showed the most significant stress and displacement changes from 0°C to 50°C. Simulating the same geometry with a gravitational force of $1g$ yielded consistent results, reaffirming gravity's minimal effect regardless of the spacer material.

Ultimately, we plot the relative length variation ($\frac{\Delta L}{L}$) against temperature (T) for the previously mentioned configurations. This graph aims to estimate the cavities' zero crossing temperature and illustrate the curve's behavior. This plot depicted in Fig. 3.10.

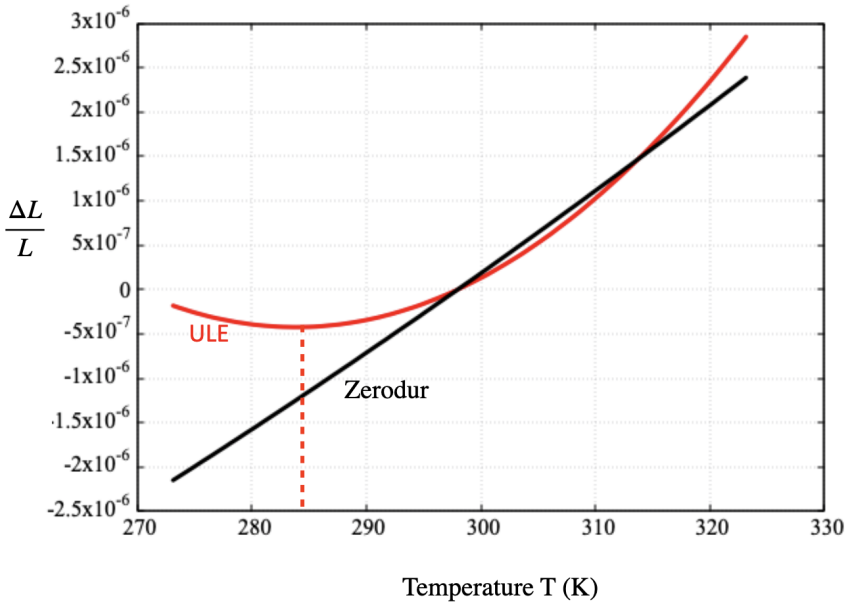

Figure 3.10: Relative length variation ($\frac{\Delta L}{L}$) vs. Temperature (T) : Red solid line represents the configuration where the spacer is made from ULE ; Black solid line represents the configuration where the spacer is made from Zerodur

The plot in Fig. 3.10 illustrates distinct characteristics of the spacers: the ULE-made spacer (red solid line) shows a parabolic trend indicates an inversion point at around 11°C whereas the Zerodur spacer (black solid line) demonstrates a linear trend. To verify this with the experimental data to determine the material composition of the spacer, we need measurements at temperatures below 11°C. Unfortunately, due to limitations imposed by the temperature controller, conducting measurements at temperatures below 11°C, crucial for confirming this theory, is unfeasible with the current cavity setup. Therefore, the simulations are inconclusive in determining both the cause for the absence of the CTE zero crossing and the precise material composition of the spacer.

3.4.5 Thermal Noise

Initially uncertain about the spacer material composition, we conducted inconclusive FEM simulations to estimate its identity. To address this, we aimed to calculate the cavity thermal noise under two scenarios: one with a ULE spacer and another with a Zerodur spacer. Our hypothesis was that differing thermal noise effects on the cavity would distinguish between the two materials, aiding in identification.

To calculate the cavity thermal noise, we modeled the spacer as a double tetrahedron and optically contacted two mirrors (one plane and one concave) made of fused silica (SiO_2) to the

spacer. These mirrors featured AlGaAs reflective coatings, each with a thickness (w) of 6.83 μm. Simplifying the cavity as a cylinder with a radius (R_{sp}) of 22 mm and a central bore diameter (r_{sp}) of 5 mm allowed for the passage of a 190 μm laser beam waist.

Considering fused silica's properties, we used a Young's modulus (E) of 70.3 GPa, a Poisson's ratio (σ_{FS}) of 0.16, and a loss angle (ϕ_{sb}) of 1×10^{-6} [138]. The reflective coatings' properties, comprising AlGaAs, included a Poisson's ratio (σ_{coat}) of 0.32 and a loss angle (ϕ_{ct}) of 2.5×10^{-5} [56].

To compute the thermal noise for the spacer, we required the properties of ULE and Zerodur. For ULE, we considered a Young's modulus (E) of 73 GPa, a Poisson's ratio (σ_{coat}) of 0.17, and a loss angle (ϕ_{ULE}) of 1.6×10^{-5} [32]. Similarly, for Zerodur, we utilized a Young's modulus (E) of 90.3 GPa, a Poisson's ratio ($\sigma_{Zerodur}$) of 0.24, and a loss angle ($\phi_{Zerodur}$) of 3.2×10^{-4} [29].

The outcomes of the thermal noise calculations for each component, encompassing the spacer, mirrors, and mirror coatings, are detailed in Table 3.3.

Type	$S_x^{spac.}(f)$ f^{-1}(m^2/Hz)	$S_x^{sub.}(f)$ f^{-1}(m^2/Hz)	$S_x^{coat.}(f)$ f^{-1}(m^2/Hz)	$S_x(f)$ f^{-1}(m^2/Hz)
Zerodur(spac.) FS(sub.) AlGaAs(coat.)	1.6 x 10^{-34}	2.1 x 10^{-34}	2.3 x 10^{-34}	1 x 10^{-33}
ULE(spac.) FS(sub.) AlGaAs(coat.)	9.7 x 10^{-36}	2.1 x 10^{-34}	2.3 x 10^{-34}	8.8 x 10^{-34}

Table 3.3: Thermal noise contributions from different components of the Fabry-Pérot cavity, including the total thermal noise contribution. The abbreviations used are FS for Fused Silica, spac. for spacer, sub. for substrate, and coat. for coating.

The calculations are performed for both ULE and Zerodur spacers. Additionally, Table 3.4 illustrates the relative contributions of each cavity component to the overall thermal noise.

Type	Spacer(%)	Coatings(%)	Substrates(%)
Cavity with Zerodur spacer	15	44	41
Cavity with ULE spacer	1	51	48

Table 3.4: Relative contribution of the spacers made of ULE and zerodur, fused silica mirrors and AlGaAs coatings on the thermal noise of the Fabry-Pérot cavity

Information from Tables 3.3 and 3.4 highlights the significant impact of thermal noise with a Zerodur spacer, contributing approximately 15 % to the total, while the ULE spacer's impact remains minimal at 1 %. The dominance of mirror and coating contributions (more than 40 %) in both scenarios diminishes the spacer's influence, resulting in minimal disparity in thermal noise between

the two materials.

Proceeding with the conversion of total thermal noise ($S_x(f)$) to phase noise ($S_\varphi(f)$) at 1 Hz Fourier frequency and frequency noise ($\sigma_y(s)$) at a 1 second integration time, we found nearly identical phase noise (-12 dBrad^2/Hz at 1 Hz) and frequency noise (1×10^{-15} at 1 second) for cavities made from Zerodur and ULE. This similarity underscores the challenge in deducing spacer material based solely on thermal noise calculations. Thus, the choice of spacer material seems to exert a limited impact on the cavity thermal noise, maintaining a comparable level in both instances.

3.5 Conclusion

This chapter shows the performance evaluation of a compact ULE Fabry-Pérot cavity, showcasing a measured finesse of 247,000, aligning with an FSR of 6 GHz. Insights into the cavity design, mounting procedures, and vacuum chamber setup are provided, alongside the implementation of a digital Pound Drever Hall (PDH) frequency locking technique for improved functionality. Notably, the digital electronics approach yielded a commendably low phase noise of 3 dBc at a 1 Hz Fourier frequency, exhibiting an f^{-3} slope when compared to an f^{-2} slope from the previously measured phase noise with analog PDH electronics..

Nevertheless, several limitations came to light concerning the cavity operation. Initially, thermal noise impeded achieving a fractional frequency stability below 1×10^{-15} within a 1-second integration time. Additionally, measurements revealed that vibration and acceleration sensitivities exceeded the values predicted by simulations.

A pivotal observation was the absence of a CTE zero crossing. Potential reasons were identified, primarily focusing on the cavity material composition—whether constructed from ULE or a similar material like zerodur. The discrepancy could also arise from using ULE with altered characteristics, potentially shifting the CTE zero crossing and resulting in inaccuracies in our simulations. Despite employing FEM simulations and conducting thermal noise calculations, determining the cavity material and deciphering the absence of a zero crossing remained inconclusive.

Consequently, a decision was made to develop a new cavity with modifications in design, employing ULE with controlled and documented intrinsic properties. Detailed information about this new cavity can be found in Chapter 4 of my thesis.

Chapter 4

Towards a new Transportable Ultra Stable Laser

4.1 Introduction

This chapter presents the realization of a new transportable ultra stable laser based on an updated version of the compact Fabry-Pérot cavity [131] described in Chapter 3 of this thesis. The chapter begins with an overview of the objectives and structure, followed by a summary of the key contributions and research questions addressed. The significance and novelty of the work are highlighted, setting the stage for the subsequent sections.

A description of the modified design and geometry of the Fabry-Pérot cavity is provided. The changes made to the cavity are explained, emphasizing the improvements in stability and portability. The design considerations, such as mirror coatings and materials, are discussed, along with their impact on the performance of the cavity.

The newly designed mount for the Fabry-Pérot cavity, made of INVAR, is presented. The rationale behind choosing INVAR as the material is discussed, comparing it to other metals like stainless steel. The advantages and disadvantages of INVAR are evaluated, taking into account factors such as thermal expansion, mechanical stability, and vibration damping. The detailed design and construction of the mount are described, highlighting its role in maintaining the stability and performance of the cavity.

A compact, low-noise, and high-current rated power supply distribution setup designed for the compact cavity setup and the optical fiber link setup is introduced. The design considerations, circuitry, and components used in the power supply setup are detailed. The functionality and performance of the power supply distribution system are evaluated, highlighting its role in powering the electronic components of the cavity setup and the optical fiber link.

An updated and compact optical and electronics scheme designed for the compact cavity and the 25 m long optical fiber link used to disseminate the ultra-stable frequency from the

USL is presented. Notably, this optical fiber link is 10 m longer than the one discussed in Chapter 2 of this thesis. The extension was made to align with the practical implementation of the setup as detailed in Chapter 2, where the objective is to compare two ultra-stable lasers positioned in separate rooms within the laboratory, approximately 25 m apart. The design and integration of the fiber optical components and electronics for both setups into two 19-inch rack mountable boxes are described. The synchronization, signal routing, and data acquisition aspects are discussed, emphasizing the efficient and reliable transfer of the ultra-stable frequency over the optical fiber link.

The technique of cavity mode matching, which involves adapting the spatial mode of a laser beam to the resonance mode of the Fabry-Pérot cavity, is detailed. The experimental setup used to achieve cavity mode matching is presented, along with the procedures employed. Furthermore, the generation of a beatnote with another ultra-stable laser, locked to a spherical Fabry-Pérot cavity located in a different room, is explained. The utilization of the noise-compensated optical fiber link to transmit signals between the experimental room and the room housing the USL locked to the spherical cavity is also discussed.

The measurements conducted with the compact cavity are presented. This includes the finesse measurement using the cavity ringdown technique. The experimental setup, the data acquisition procedures, and analysis methods for the finesse measurement are explained. The measurement of birefringence of the mirror coatings is discussed, including the phenomenon of mode splitting. The technique implemented to measure the coefficient of thermal expansion (CTE) of the cavity is described, along with the challenges encountered. The effect of phase noise on the performance of the cavity and fractional frequency measurements are also presented. Finally, a detailed conclusion is provided, discussing the issues associated with the cavity and suggesting future improvements.

4.2 Design and Geometry

The geometric configuration of the cavity was maintained identical to its previous version. However, in the previous iteration, a notable absence of CTE zero crossing was observed. Our investigation led us to suspect that this anomaly was attributed to the utilization of an outdated ULE material for manufacturing the spacer, the CTE of which remained unknown at a specific temperature.

Considering the impact of this factor, we made the decision to introduce a new and modified spacer. As part of this modification, we eliminated the ULE rings located on the back of the mirrors. To counterbalance the CTE mismatch between the fused silica mirrors and the ULE spacer, we procured a ULE material with a higher intrinsic CTE value. It is anticipated that the ULE spacer will exhibit a CTE zero crossing at approximately 48 ± 5°C. By taking into account the

influence of the two fused silica mirrors on the spacer, we calculated an anticipated temperature inversion for the overall cavity, estimated to occur around 18±5°C. The new and updated Fabry-Pérot cavity with ULE spacer, Fused Silica mirrors and AlGaAs coatings is shown in Fig. 4.1

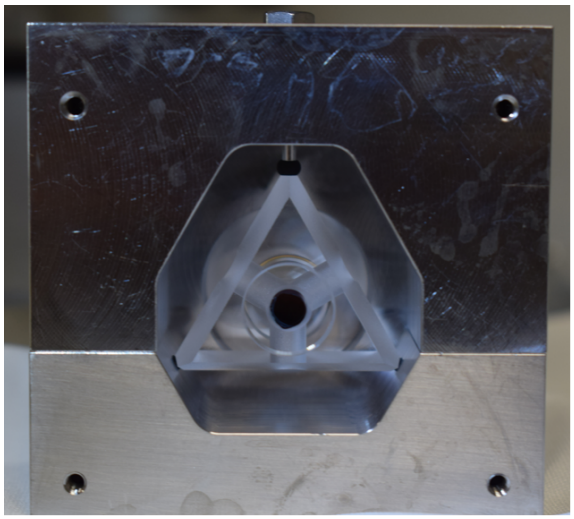

Figure 4.1: Updated version of compact Fabry-Pérot cavity. The overall design is maintained. Dimensions have been scaled to adapt to the absence of ULE rings using [131].

4.3 Cavity support

The choice to replace the stainless steel support for the cavity with a new support fabricated from Invar 36 was made in response to the identified limitations hindering the achievement of the desired cavity performance, as detailed in Chapter 3. Stainless steel, being the material used in the previous support, exhibited sensitivity to temperature fluctuations due to its higher coefficient of thermal expansion (CTE). It was suspected that this sensitivity introduced challenges in maintaining dimensional stability as the temperature varied.

Invar 36, also known as FeNi36, belongs to the family of low expansion iron-nickel alloys. Composed of 64 % iron (Fe) and 36 % nickel (Ni), Invar 36 possesses exceptional properties, with its most valuable characteristic being an extremely low CTE. In fact, Invar has the lowest CTE among all metals, making it an ideal choice for applications requiring precise dimensional control under varying temperature conditions [139][140].

Metal	CTE ($\times 10^{-6} K^{-1}$)
Aluminium	23.6
Copper	17.0
Gold	14.2
Stainless Steel	16.0
Invar	0.5 to 2.0
Super Invar	0.3 to 1.0

Table 4.1: Comparison of coefficient of thermal expansion (CTE) for different metals.

A comparison of the CTE values for different metals further highlights the advantage of Invar 36 over stainless steel. Table 4.1 illustrates that Invar 36 exhibits a CTE range of 0.5 to 2.0 $\times 10^{-6}$ K^{-1}, whereas stainless steel has a CTE of around 16 $\times 10^{-6}$ K^{-1}. This substantial difference of approximately 14×10^{-6} K^{-1} in CTE enables Invar 36 to provide superior dimensional stability and minimize the impact of temperature variations on the cavity length.

The design of the new support for housing the cavity remains consistent with the previous version, as detailed in Section 3.2 of Chapter 3. The cavity is securely housed within a central enclosure comprising three parts, all fabricated from Invar. To ensure proper placement, the cavity rests on the bottom part of the central enclosure using two Viton pads. These pads, 2 mm in diameter and 1 mm thick, are positioned through 0.5 mm deep pockets machined on the bottom holder. The cavity is held in place by an Invar piston, guided by translation through the use of an SS screw and a 3.5 mm diameter Viton sphere, as discussed in Section 3.2.

It is worth noting that modifications were made to the design of the translation system, specifically the piston, due to the complex geometry and guidance system of the previous version. Invar is a rigid metal, and machining it requires specialized expertise that is not readily available in all industries. Therefore, a simpler design was adopted for the translation system to facilitate the machining process while ensuring the functionality and performance of the cavity.

In addition to the support structure, the thermal shielding technique employed in the previous version of the cavity remains unchanged. A copper shield with a polished gold surface acts as the shield, providing effective thermal insulation and protection against external influences. Figure 4.2 visually depicts the updated support for the new cavity, showcasing the integration of the Invar 36 components and the overall assembly.

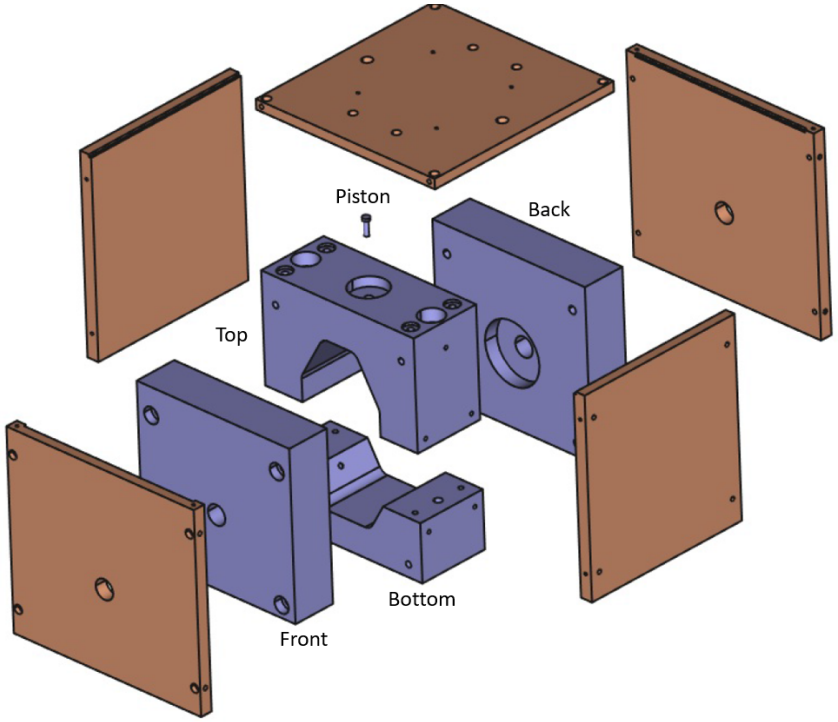

Figure 4.2: CAD assembly of the enclosure to house the Fabry-Pérot cavity. Blue parts constitute the inner enclosure made of Invar where the cavity is housed. Brown parts constitute the copper shield with polished gold layer that acts as a thermal shield to reduce the effect of temperature fluctuations on the cavity.

By leveraging the unique properties of Invar 36, including its low CTE and dimensional stability, the new support design not only addresses the limitations associated with the previous stainless steel support but also accommodates the smaller geometry of the cavity. This comprehensive approach ensures improved performance, enhanced temperature stability, and reliable operation of the cavity in various environments.

4.4 Vibration Isolation

In order to mitigate the effects of mechanical vibrations, a vibration isolation system has been implemented. A compact and highly effective active vibration isolation platform, the Table Stable TS-C30, measuring $300 \times 300 \times 70$ mm (length, width, height), serves as the primary support structure for the vacuum chamber associated with the Fabry-Pérot cavity.

To augment the vibration isolation capabilities, passive isolation has been incorporated into the setup. The vacuum chamber, securely fastened onto the active vibration isolation platform, is further mounted on a secondary optical breadboard. This secondary breadboard, resting on an optical table, is supported by four sorbothane posts situated at the corners of the breadboard. These posts contribute to passive isolation by effectively attenuating vibrations transmitted through the optical table. The entire vibration isolation system, encompassing the active vibration

isolation platform, vacuum chamber, and passive isolation configuration, is depicted in Figure 4.3.

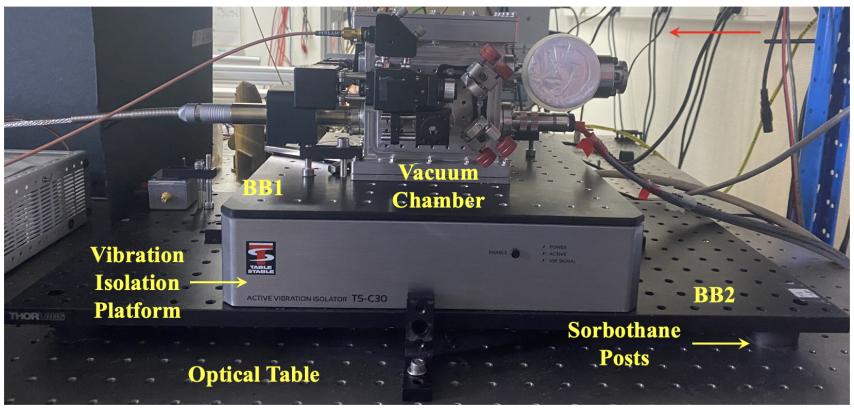

Figure 4.3: Photograph of the vacuum chamber housing the cavity resting on a vibration isolation platform (Table Stable TS-C30), where BB1 and BB2 are Breadboard 1 and Breadboard 2.

4.5 Power Supply

4.5.1 Introduction

In our previous version of the ultra-stable laser system and optical fiber link, we utilized low-noise linear power supplies. However, these power supplies are characterized by significant size and weight, contributing approximately 35 liters in volume and 30 kg in the weight budget allocated to the electronics of the fiber link and the compact cavity combined. This reliance on large linear power supplies was necessitated by the diverse voltage and current requirements of the various system components. Consequently, the presence of multiple linear power supplies added considerable bulk to our overall setup. Table 4.2 provides a listing of the voltage and power ratings associated with several components within the ultra-stable laser and optical fiber link systems.

Component	Quantity	Voltage (V)	Current (A)	Power (W)
RF Amplifiers	1	+24 V	0.5 A	12 W
RF and DC Amplifiers RIO laser diode Photodiodes	1 1 3	$\pm$15 V	2 A	30 W
RF Amplifiers Temperature controlled breadboard Temperature controller	2 1 1	+12 V	2.3 A	28 W
Red Pitaya	2	+5 V	3 A	15 W
Total				85 W

Table 4.2: Voltage, current and power ratings of various electronic components used for the compact Fabry-Pérot cavity and noise compensated optical fiber link.

From Table 4.2, we can observe that our equipment configuration involves the use of five different voltage levels (+24 V, $\pm$15 V, +12 V, +5 V) with varying current requirements, resulting in a total

power demand of 85 W. Notably, the highest power consumptions are observed in the +15 V, +12 V, and +5 V supplies.

This distinction arises due to specific equipment connections. The +15 V supply powers the laser, one DC amplifier, one RF amplifier, and three fast photodiodes. Meanwhile, the +5 V supply is responsible for driving two Red Pitayas, each with a current requirement of 1.5 A. Additionally, the +12 V supply caters to the needs of the temperature-controlled breadboard, which has a current requirement of 2 A, as well as two RF amplifiers. Understanding these voltage-specific power allocations is crucial for ensuring appropriate power supply provisioning in our setup. The power supply distribution for the previous version of the USL is depicted in Fig. 4.4.

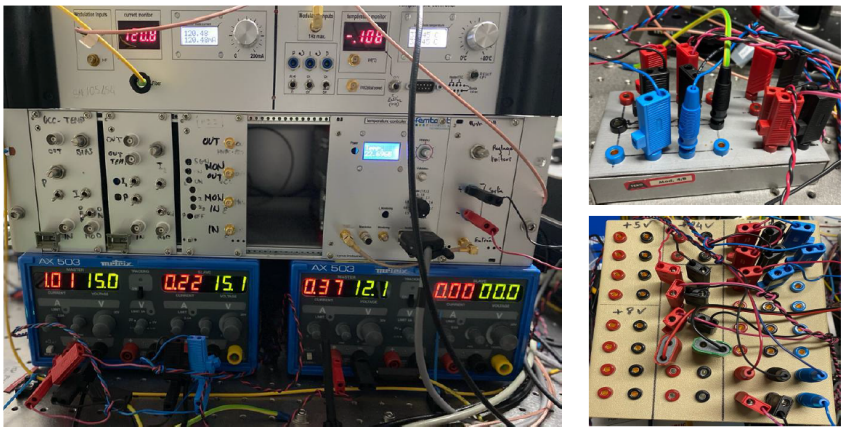

Figure 4.4: Picture showcasing the power supply distribution setup for the old USL, featuring two linear power supplies generating ±15 V and 12 V. Each linear power supply measures 120 mm×270 mm×225 mm (Height, Length, Breadth) and weighs 6 kg. Right hand side picture depicts two custom-made electronic boards, which utilized banana cables, to deliver power to the respective electronic components. So we had a total weight of 12 kg and a height of approximately 3U (where U signifies rack units).

Similarly, the power supply distribution setup for the phase noise compensated optical fiber link is shown in Fig. 4.5.

Figure 4.5: Power supply distribution for optical fiber link that includes a combination of four linear power supplies, supplying $\pm$15 V, +15 V and +12 V with a total weight of 25 kg and occupying a dimension of approximately 5U.

Figures 4.4 and 4.5 illustrate the comprehensive power supply distribution for both the USL and the optical fiber link. It is important to note that for the 5 V power supply required by the redpitayas, the provided AC-DC converter from the company was used in both the setups.

When consolidating the entire power supply configuration, the collective weight approximates 40 kg and occupies 8U in total for the combined setups. This considerable weight and size render it impractical for portable applications due to its substantial mass and bulkiness.

4.5.2 Power Supply Model

Given the impractical heaviness and size of the linear power supplies, an alternative compact, low-noise power supply solution was devised. Figure 4.6 illustrates the schematic representation of this compact power supply, showcasing its design intended to achieve a smaller footprint.

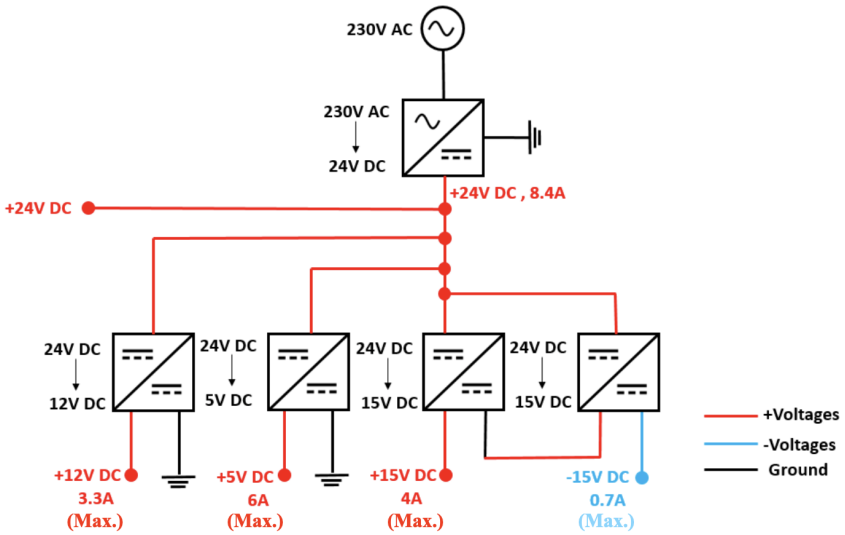

Figure 4.6: Scheme of the new, updated and compact power supply for the USL and the optical fiber link.

Table 4.2 revealed that both the USL and the optical fiber link necessitated five distinct voltages, each with varying current ratings, amounting to a cumulative power demand of 85 watts. To fulfill these specifications, compact AC-DC and DC-DC converters were employed.

A 230 VAC - 24 VDC converter (Traco Power TXLN 200-124) with a high output current of 8.4 A and power rating of 201 W was selected as the main power source. This AC-DC converter has a length, width and depth of 212 mm, 115 mm and 30 mm respectively. From the 24 VDC output, power was distributed to four DC-DC converters to generate the required specific voltages. The chosen DC-DC converters are

1. 24 VDC-12VDC (Traco Power TEN 40-2412WIR) with an output current rating of 3.3 A with dimensions of approximately 51 mm×25 mm×10 mm (L×B×H).
2. 24 VDC-5 VDC (Traco Power THM 30-2411WI) with an output current rating of 6 A with dimensions of approximately 25 mm×51 mm×10 mm (L×B×H).
3. 24 VDC-15 VDC (Traco Power TRI 10-2413) with an output current rating of 0.7 A with dimensions of approximately 32 mm×20 mm×12 mm (L×B×H).
4. 24 VDC-15 VDC (Traco Power TEL 10-2423WI) with an output current rating of 4 A with dimensions of approximately 14 mm×24 mm×8 mm (L×B×H).

For the +15 V and -15 V power supplies, two 24 VDC-15 VDC converters were used, with the ground terminal of one connected to the positive terminal of the other to obtain the desired polarities. Alternatively, a single DC-DC converter providing a single -15 V output could be used. Gilles Martin from the electronics department of Femto-ST Institute developed a specialized compact PCB dedicated to housing all the necessary DC-DC converters with filtering. The AC-DC module

was kept separate. This PCB was designed to include adequate filtering mechanisms, ensuring interference avoidance and proficient noise reduction. Subsequently, the PCB was securely housed within an aluminium enclosure with dimensions of 222 mm$\times$146 mm$\times$56 mm (Length, Width, Height), serving as a shield against external electromagnetic interference.

The recently introduced compact power supply configuration boasts a power rating of roughly 201 Watts, surpassing the required capacity for the two setups by a factor of 2.5. Notably, it maintains a compact form factor, measuring approximately 2U in dimension and weighing only 1 kg. This marks a significant advancement compared to the prior power supply configuration, which collectively weighed 40 kg and occupied roughly 8U in dimensions. Moreover, the increased power ratings of this new supply allow for the integration of several additional pieces of equipment into the setups.

4.5.3 Power Supply Noise Spectrum

To determine the performance of the compact power supply, a voltage noise analysis was conducted. Please note that due to shortage of time, the whole power supply setup that included all the DC-DC and AC-DC converters was not characterised. We only characterised the 5 V DC-DC converter that was supplied by a linear Metrix power supply.

We utilized a low-noise Agilent FFT 35670A dynamic signal analyzer for our measurements. To assess the behavior of the power supply output signal across a load, denoted as R_L, we connected it to the power supply denoted as VDC being tested. The load used in our experiments was a redpitaya. We employed the redpitaya as the load to evaluate its effect on the signals from three different power supply configurations:

1. Redpitaya supplied by 5 V adapter provided by the manufacturer of Redpitaya.
2. Redpitaya supplied by linear Metrix power supply.
3. Redpitaya supplied by DC-DC converter (Tracopower) supplied by linear Metrix power supply.

In order to ensure the reliability of our measurements and verify that external factors such as temperature fluctuations and vibrations did not affect the results, we conducted the same measurements in a controlled environment within a Faraday cage. This allowed us to isolate the setup from external electromagnetic interference. In addition, we included an extra measurement to assess the machine noise. To accomplish this, a 50 Ω load was connected to one of the input channels of the FFT analyzer, and we carried out the measurements using the same configurations as before. The power spectral density of voltage noise versus frequency plots for the four previously mentioned configurations are depicted in Figure 4.7. Measurements performed in and out of the Faraday cage gave identical results.

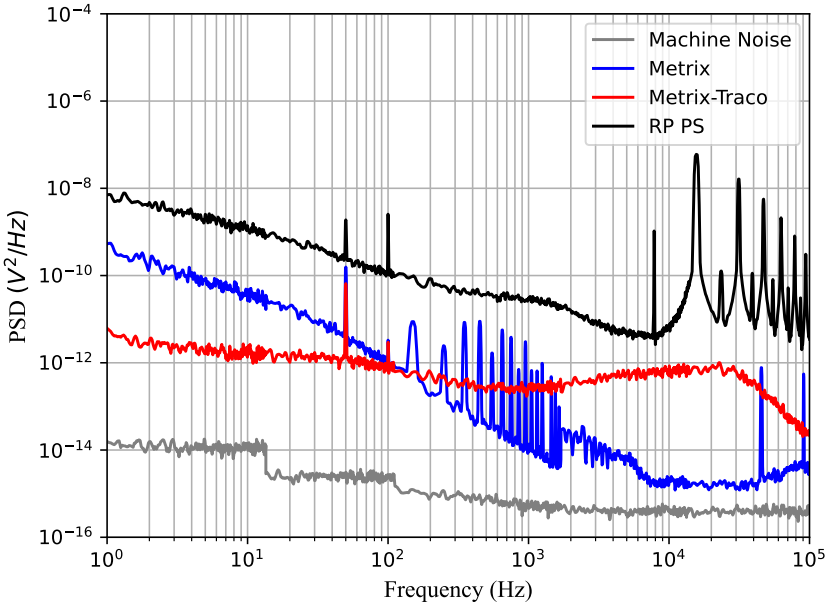

Figure 4.7: Comparison of PSD of voltage noise between different power supplies. The black solid line represents the noise spectrum of the redpitaya power supply, the red solid line corresponds to the noise spectrum of the Traco power supply supplied by a linear Metrix power supply and the blue solid line represents the noise spectrum of the standalone Metrix power supply. The gray line represents the noise spectrum of the FFT analyser.

The PSD of voltage noise for the above mentioned power supplies at 1 Hz Fourier frequency is listed in Table 4.3.

Equipment	PSD ($V^2Hz^{-}1$)	PSD ($dBrad^2Hz^{-}1$)
Redpitaya Power Supply (black)	7e-09	18
Metrix Power Supply (cyan)	5e-10	6
Metrix-Traco Power (red)	3.5e-12	-15

Table 4.3: PSD of voltage noise for the above mentioned configurations at 1 Hz Fourier frequency.

Figure 4.7 and Table 4.3 provide insights into the performance of different power supplies. It is evident that the redpitaya power supply, specifically a wall AC-DC adapter, exhibits the poorest performance at 1 Hz, with a PSD of 7×10^{-9} V^2/Hz. Comparatively, the linear power supply demonstrates better performance, with a PSD of 5×10^{-10} V^2/Hz at 1 Hz. However, the Traco power supply stands out with the best performance, boasting a significantly lower PSD of 3.5×10^{-12} V^2/Hz at 1 Hz. Notably, at higher frequencies, the linear power supply outperforms the Traco power supply. To enhance the performance of the Traco power supply, appropriate filtering to reduce higher frequencies can be implemented. Simultaneously, upon reviewing the gray curve depicting the voltage noise from the FFT analyzer, we can observe that it registers significantly lower noise than the measured voltage noise levels of the power supplies, affirming that machine noise is negligible within our context.

Additionally, we also observe that the noise spectrum of the Traco power supply in

a Faraday cage closely resembles that in a normal environment. Similarly, the noise spectra of the redpitaya power supply exhibit similar behavior in both normal and Faraday cage conditions. These measurements suggest that room conditions have minimal impact on the performance of the power supplies. Notably, consistent bumps at 200 Hz and 300 Hz are observed in the Traco power supply's noise spectra, both in normal and Faraday cage environments. Addressing these bumps may require effective filtering and shielding measures.

In the third column of Table 4.3, I converted the noise in the powersupply, measured in V^2/Hz, to phase noise, expressed in dBrad^2/Hz, using the equation 1.45. This conversion assumes that all the power supply voltage noise translates into the error signal, leading to potential overestimation in the calculated S_φ(f) values. Further measurements are necessary to fully understand how the power supplies affect the PDH for the cavity. Time constraints prevented these additional measurements. Nevertheless, in our comparative analysis, the S_φ(f) value for the Tracopower supply supplied by the Metrix power supply at the 1 Hz Fourier frequency reached -15 dBrad^2/Hz, which is lower than the cavity's estimated thermal noise limit of -12 dBrad^2/Hz.

As detailed in subsection 4.5.2, our implemented compact power supply setup replaced the linear Metrix power supply with a compact 24 V Tracopower AC-DC converter to power the 24 V to 15 V Tracopower DC-DC converter. While the performance of this specific setup wasn't evaluated due to time constraints, the performance of the 24 V to 5 V Tracopower DC-DC converters outlined in this section allows an estimation of the composite power supply's performance. This estimation suggests that it would meet the necessary standards, performing well below the thermal noise limit of the cavity and the phase noise of the optical fiber link required for frequency transfer.

4.6 Compact Electronics Boxes

In this section, I will describe a compact and transportable scheme for the USL and the optical fiber link used for signal distribution. The scheme combines the cavity setup and the optical fiber link setup into two compact 19 inch rack mountable boxes. These boxes have dimensions of 88 mm$\times$483 mm$\times$466 mm (Height, Length, Breadth). Box 1 (B1) contains all the fiber optical components, while the electronics required to operate the cavity and the fiber link are housed in another box (B2). The updated scheme is illustrated in Figure 4.8.

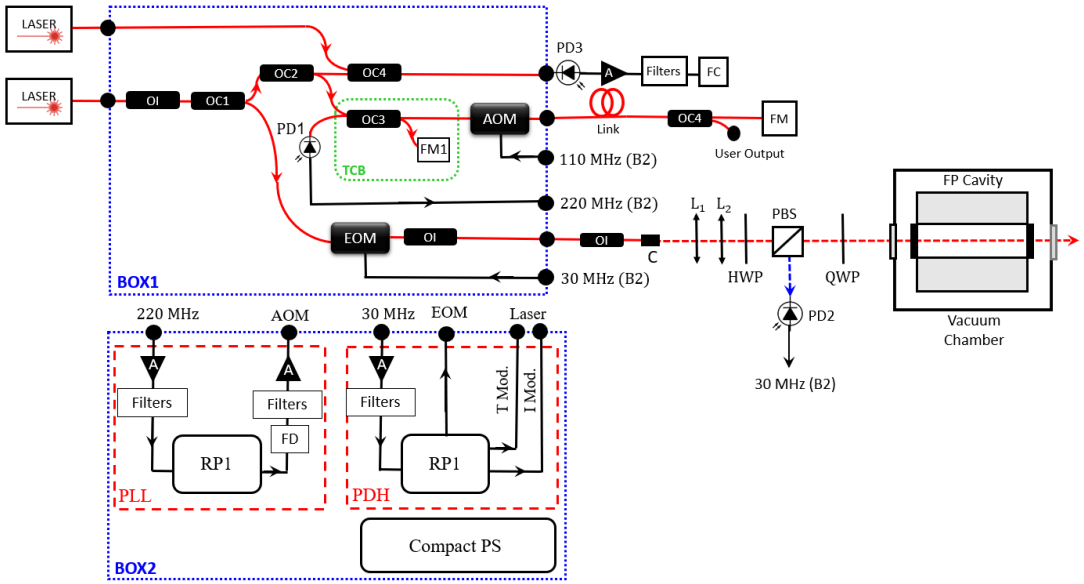

Figure 4.8: Schematic of the compact electronics design for the compact Fabry-Pérot cavity and optical fiber link. The components included are: optical isolator (OI), optical coupler (OC), photodiode (PD), Acousto Optical Modulator (AOM), Electro Optical Modulator (EOM), Faraday mirror (FM), RF amplifier (A), half wave plate (HWP), quarter wave plate (QWP), frequency doubler (FD), redpitaya (RP), temperature modulation to the laser (T. Mod.), current modulation to the laser (I Mod.), power supply (PS), collimator (C), frequency counter (FC), temperature controlled breadboard (TCB), lens (L), and Faraday rotator (FR).

B1 integrates the necessary fiber optical components for the cavity and optical fiber link. The laser input is stabilized within the cavity by passing through a PM isolator (OI) and a 90:10 PM optical coupler (OC1). Utilizing the 10 % output of OC1, the laser is further stabilized within the cavity using an EOM and another PM isolator. The fibered output of the isolator is connected to a collimator positioned on the side of the vacuum chamber via a drilled hole at the bottom of Box 1, minimizing fiber length. The setup includes lenses (L1 and L2) for mode matching, a HWP, a PBS, a FR, and injection mirrors as described in Chapter 3.

Additionally, the 90 % output of OC1 is directed to OC2, where the 10 % output is utilized for cavity characterization by creating a beatnote with a superior USL. For ultra-stable frequency transfer via a Doppler cancellation scheme, another 90:10 optical coupler is employed. Its 90 % output feeds a 25 m optical fiber through an AOM, while the 10 % output is reflected back using FM1 to generate a beatnote signal with the retro-reflected signal from the remote end of the link. PD1 detects the beatnote signal, which is then transmitted to B2 for further processing with a digital PLL. To maintain stability, the reference arm of the Michelson interferometer is secured on top of a temperature-controlled breadboard (TCB). Refer to Figure 4.9 for the picture of Box 1.

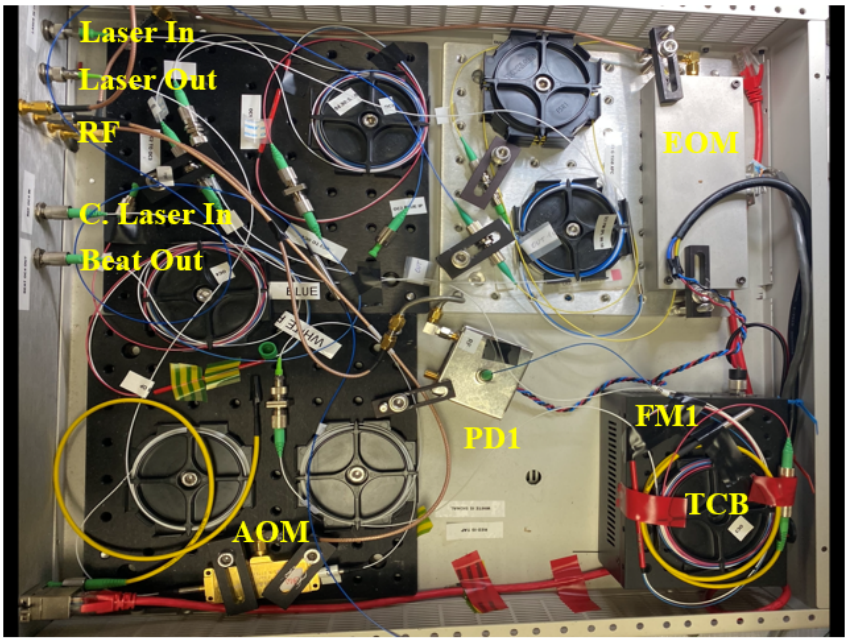

Figure 4.9: Integration of fiber optical components for the compact cavity and optical fiber link within B1 (88 mm×483 mm×466 mm). C. Laser In is the cavity laser input port, AOM is acousto optical modulator for the fiber link stabilisation, PD1 is photodiode used for the fiber link, TCB is the temperature controlled breadboard, EOM is electro optical modulator for the PDH technique.

The second box, B2, houses all the necessary electronics for the system. This includes two Redpitayas dedicated to PDH lock and PLL functions, RF filters, couplers, and a range of RF amplifiers, including a high-gain amplifier specifically designed to drive the AOM.

To ensure efficient power distribution and connectivity, a compact power supply, as described in Section 4.5, is also integrated into B2. This power supply provides power to all electronic components within the box and external components, such as the laser and temperature controller, via banana connectors located on the front panel of the box. A laboratory-designed PCB with dedicated DC-DC converters is securely housed in a stainless steel box for effective shielding.

In the setup for the optical fiber link, the 220 MHz signal from photodiode PD1 in B1 is received through an SMA cable connected to the front panel of B1. The digital phase-locked loop is implemented using the Redpitaya in an undersampling configuration. The correction signal for the AOM in B1 is transmitted via an SMA connector on the front panel of the box. Additionally, two RF couplers are included for monitoring the input and output signals.

Likewise, for the cavity setup, the 30 MHz signal from the photodiode mounted on the vacuum chamber is received through an SMA cable connected to the front panel of B1. The Pound-Drever-Hall (PDH) locking technique is established using the second Redpitaya mounted inside B2. Please refer to Fig. 4.10 for the picture of Box 2.

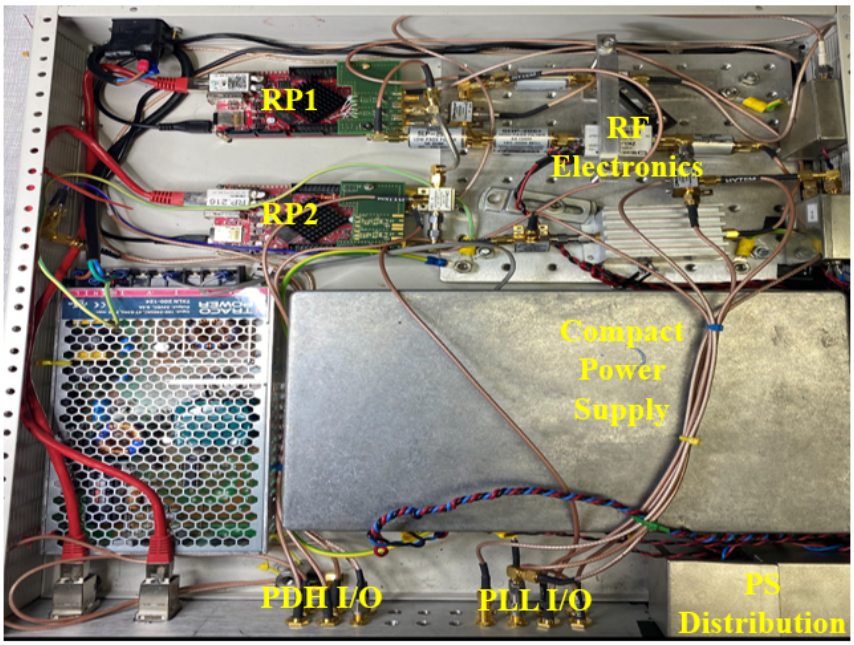

Figure 4.10: Merged electronics components for compact cavity and optical fiber link in Box 2 (88 mm×483 mm×466 mm) that includes the compact power supply and RF electronics for both the USL and the optical fiber link. RP1 is the redpitaya used for fiber link stabilisation, RP2 is the redpitaya used for PDH technique, PLL I/O are the input and output ports for the phase locked loop of the fiber link, PDH I/O are the input and output ports for the PDH technique.

The complete setup, depicted in Figure 4.8, showcases the integration of the compact cavity and the optical fiber link using the two boxes.

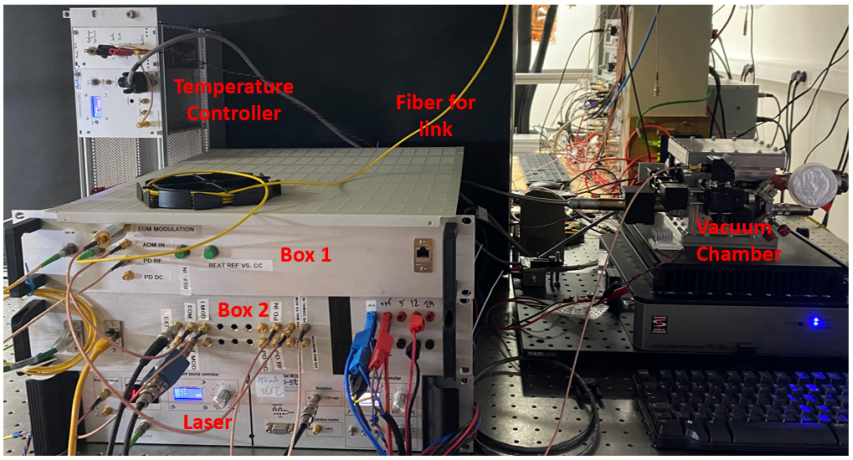

Figure 4.11: Setup of the compact ultra stable laser based on the compact Fabry-Pérot cavity and the optical fiber link.

The collective volume of the entire setup, encompassing the electronics, temperature controller, laser for the optical fiber link, and Fabry-Pérot cavity (excluding the vacuum chamber and vibration isolation table), amounts to roughly 10U. This is notably more compact compared to the prior version, which took up around 20U, inclusive of the laser and power supplies. It's worth noting

that further reduction to 6U is feasible by substituting the temperature controller with a PCB-based alternative that can be integrated into Box 2. While this enhancement hasn't been implemented in the current setup, it remains a planned enhancement for future iterations.

4.7 Cavity Mode Matching

Cavity mode matching is a crucial step in the design of an USL. It involves aligning the Gaussian mode of the laser beam with the fundamental Gaussian mode of the cavity. This ensures efficient trapping and amplification of the light within the cavity, resulting in higher photon densities and stronger optical effects. The mode matching scheme for our USL is illustrated in Fig. 4.12.

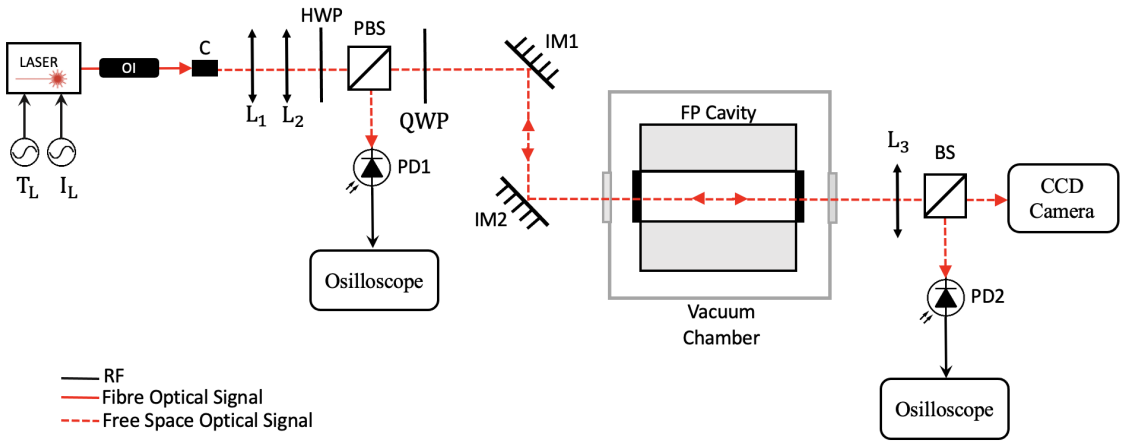

Figure 4.12: The implemented scheme illustrates the mode matching process between the laser beam and the fundamental mode of the cavity. Key components include a collimator (C), three lenses (L_1, L_2, and L_3) for adjusting the beam waist and converging the transmitted beam, a half-wave plate (HWP), a Faraday rotator (FR), injection mirrors (IM1 and IM2) for fine-tuning the beam's position and angle, a polarized beam splitter (PBS), a beam splitter (BS), and control parameters such as laser temperature (T_L) and laser current (I_L).

The laser beam is directed to a collimator through a fibered PM isolator, serving as the final fibered component in the setup. The collimated output is a free-space laser beam that requires mode matching with the cavity mode and guidance to the input mirror within the vacuum chamber. Two lenses, denoted as L_1 and L_2 with focal lengths f_1 and f_2, respectively, are utilized to adjust the beam's waist according to the cavity mode.

The beam is further guided into the cavity using two injection mirrors (IM1 and IM2). IM1 facilitates the positioning of the laser beam on the mirror, while IM2 allows for adjustment of the beam's angle upon entering the cavity. Initial alignment involves visually aligning the beam with the central axis of the cavity by adjusting IM1. If the beam is approximately aligned, a portion of it is reflected off the first mirror. Subsequently, IM2 is adjusted to ensure that the back-reflected beam coincides with the incident beam. The output or transmission of the cavity is then examined.

At the cavity transmission point, a lens denoted as L_3 is employed to converge the transmitted beam. A 90:10 beamsplitter (BS) divides the convergent beam, with 90 $\%$ of the output directed to a photodiode and the remaining 10 $\%$ to a CCD camera. The camera tracks the beam's shape, while the photodiode intercepts the beam. Proper positioning adjustments of L_3 enable imaging of the second mirror of the cavity on the camera, facilitating alignment of the beam with the cavity optical axis.

Once the incident beam is roughly aligned with the cavity optical axis, confirmed through camera imaging, the laser frequency is swept by introducing a small modulation to the laser temperature. During the frequency sweep, multiple TEM modes are observed as flashing patterns on the camera. Simultaneously, the transmission photodiode shows several peaks corresponding to each of the excited cavity modes. This spectrum repeats after each free spectral range. By slightly adjusting the alignment, changes in the intensities of the excited cavity modes can be observed.

To determine the fundamental mode of the cavity (TEM00 mode), a flashing mode is selected, and its order is determined. The laser frequency is then swept to identify the direction in which the mode order decreases. It is important to note that a lower-order mode will exhibit lower intensity compared to its adjacent higher-order mode. Once a lower-order mode is identified, the temperature modulation is halted, and current modulation of the laser is initiated. As mentioned in the control electronics section, temperature modulation has a larger range but slower response, while current modulation has a smaller range but faster response. Incorporating current modulation assists in maintaining the visibility of the lower-order mode on the screen. The alignment of the laser is then adjusted to enhance the power in the lower-order mode. The process is repeated until the lower-order mode achieves equal or greater intensity than its adjacent higher-order mode. This iterative procedure continues until the TEM00 mode is attained. The coupling is estimated to be more than 80 $\%$.

4.8 Measurements

4.8.1 Setup

To characterize the USL locked to the compact Fabry-Pérot cavity, it is essential to conduct a comparative analysis with a more advanced device that surpasses the performance of our USL. In our specific case, we employ another USL locked to a spherical Fabry-Pérot cavity, exhibiting a fractional frequency stability of 2×10^{-15} at a 1 second integration time [141].

To generate a beatnote signal between these two lasers, we implement a dedicated experimental setup, as depicted in Figure 4.13. The USL based on the spherical cavity is situated in a separate room (Room B), distinct from the location of our USL based on the compact cavity (Room A). To facilitate beatnote generation, we employ a compensated fiber link within our experimental arrangement.

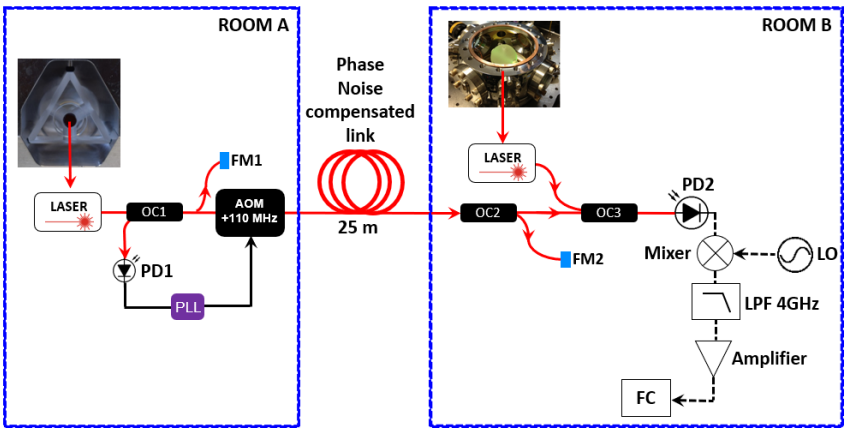

Figure 4.13: The diagram illustrates the scheme used to generate a beatnote between two USLs located in separate rooms, achieved through a laboratory-scale noise-compensated optical fiber link. PLL is phase locked loop, OC1-OC3 are fiber optical couplers, PD1 and PD2 are photodiodes, FM1 and FM2 are Faraday mirrors, LO is local oscillator, LPF is low pass filter, FC is frequency counter.

For establishing the interconnection between the two rooms, we connect the output port of the Acousto-Optic Modulator (AOM) in Room A to a 25 meter long suspended fiber link, enabling transmission to Room B. Within Room B, we extract the laser signal from Room A using a 90/10 optical coupler (OC2). The 90 % output port of OC2 serves the purpose of beatnote generation, while the remaining 10 % is routed back to Room A for noise compensation through the utilization of a Faraday mirror.

The 90 % port of OC2 is subsequently connected to another 2x2 optical coupler (OC3), with the second input receiving the stabilized output from the USL locked to the spherical cavity. As a result, a beatnote signal is generated between the two lasers at the output of OC3, which is subsequently detected using a photodiode (PD2). In our particular case, the frequency of the beatnote was measured to be 3.8 GHz.

To accommodate the limited measurement bandwidth of our frequency counter, we employed frequency mixing techniques. Specifically, we mixed the 3.8 GHz beatnote signal with a 3.78 GHz signal from a frequency synthesizer, which is synchronized with an H-MASER. This mixing process was accomplished using a frequency mixer, resulting in a 20 MHz signal at the output. The 20 MHz signal is subsequently amplified, filtered, and directed to our frequency counter or phase noise analyzer for further analysis.

4.8.2 Finesse

Joannès Barbarat from the TF Department provided assistance in conducting finesse measurements for the cavity. To determine the finesse, we utilize the cavity ring down method. This involves measuring the decay in intra-cavity power and the intensity of transmitted light over time after switching off the incident light. The finesse is extracted by analyzing the decay curve of the

transmitted light intensity. The experimental setup for measuring finesse is depicted in Figure 4.14.

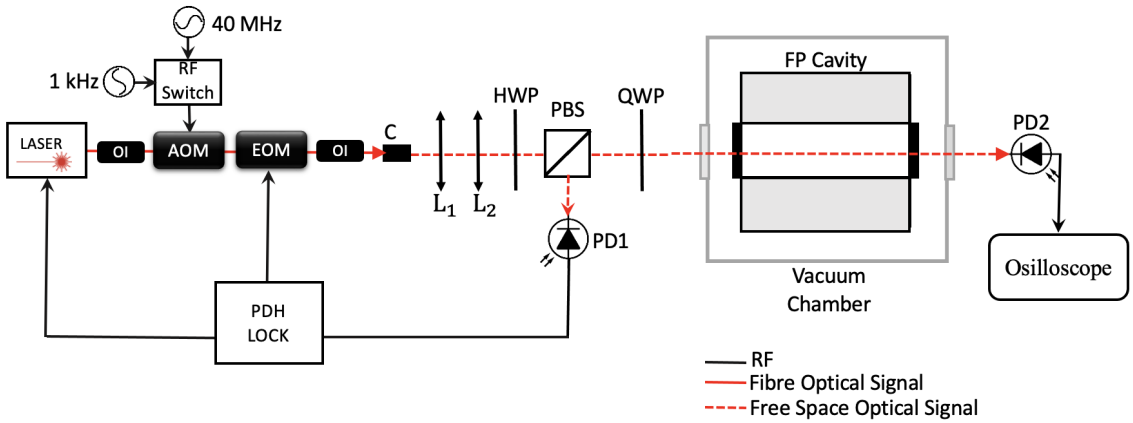

Figure 4.14: Implemented scheme illustrating the Fabry-Pérot cavity ringdown method used to determine the finesse of the cavity.

Initially, the laser is stabilized on the cavity using the Pound-Drever-Hall (PDH) lock. Then, an RF switch with a response time of 1 ms connected to an acousto-optic modulator (AOM) is used to interrupt the incident optical beam. By activating the RF switch, the AOM's modulation frequency is blocked, resulting in no transmission of optical power. A photodiode placed at the cavity transmission measures the optical decay time, which is displayed on an oscilloscope. The optical decay signal and the exponential decay fit for this signal is shown in Fig. 4.15

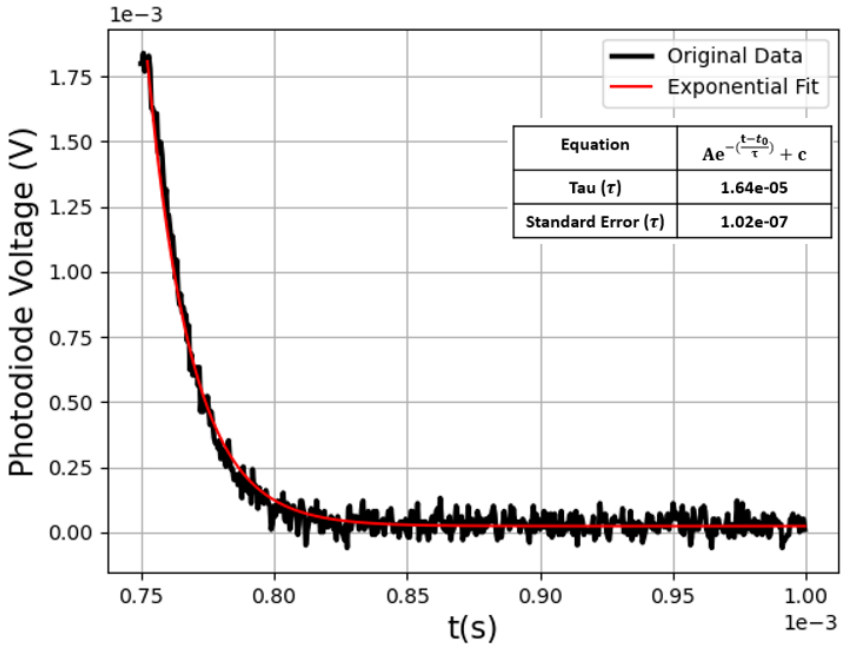

Figure 4.15: Exponential decay time of intra-cavity power when the light to the cavity is switched off, measured as voltage on the photodiode over time. Black curve is the original data and the red curve is the fitted data.

Based on the data shown in Figure 4.15, we obtained a decay time (τ) of 16.5 μs. It is important to mention that the photodiode used in the measurement had a response time of 8.5 μs. To fit the experimental data (represented by the black solid line in Figure 4.15), we applied a decaying exponential function (represented by the red solid line) using the equation:

$$f(t) = Ae^{-(\frac{t-t_0}{\tau})} + c \tag{4.1}$$

Here, A represents the amplitude, t is the time, τ is the decay time constant, and c is the offset. The relationship between the finesse ($\mathcal{F}$) of the cavity and the decay time can be expressed by the equation:

$$\mathcal{F} = \frac{\tau \pi c}{L} \tag{4.2}$$

In this equation, c corresponds to the speed of light in a vacuum, and L denotes the length of the cavity. For a cavity with a length of 25 mm, the finesse ($\mathcal{F}$) is calculated to be 625,000, given the measured decay time of 16.5 μs. This corresponds to a very narrow linewidth of 9.6 kHz which is corresponds to a significant improvement in terms of the previously measured linewidth of 24 kHz and a finesse of 247,000 for the old version of the cavity.

4.8.3 Birefringence

The mirrors used in our cavity are coated with crystalline materials that exhibit birefringent properties [54]. As a consequence, the TEM modes of the cavity are split due to variations in cavity length experienced by light with different polarizations. To demonstrate this effect, we initially align the cavity to the fundamental TEM00 mode. Subsequently, by rotating the Faraday rotator (FR) to adjust the polarization of the incident laser beam, we observe the second TEM00 mode when scanning the cavity free spectral range. The frequency difference between these two modes is 2.2 kHz. We optimize the polarization by adjusting the Faraday rotator until the intensity of the second mode reaches its maximum. Following this, we stabilize the laser and proceed with a finesse measurement. We achieved the same finesse for the two modes.

4.8.4 Thermal expansion

Our objective is to determine T_0 through a systematic approach. The experimental procedure involves initially stabilizing the laser on the cavity, followed by utilizing a phase noise compensated link to generate a beatnote with another ultra-stable laser based on a spherical cavity. Additional information on the generation of the beatnote can be found in section 4.8.1. Next we introduce small temperature steps of either 0.5°C or 1°C on the temperature controller. Due to the presence of multiple layers of shielding within the chamber, a temperature gradient is established, necessitating a 24-hour waiting period for the temperature to stabilize. Throughout this

stabilization period, we continuously measure and record the frequency change of the beatnote using a frequency counter. Specifically, we observe the change in frequency (Δf) normalized to the laser frequency (ν_{Laser}) over each temperature step (ΔT). This yields data points representing the specific behavior at different temperature intervals.

We commence our measurements from an initial temperature of 33.5°C. During the experiment, we anticipate a change in the beatnote frequency shift sign when the cavity temperature approaches the inversion temperature. The expected range for T_0 lies between 18°C to 28°C. To visualize the relationship between $\frac{\Delta f/\nu_{Laser}}{\Delta T}$ and temperature for our cavity, we present a graphical representation in Fig. 4.16.

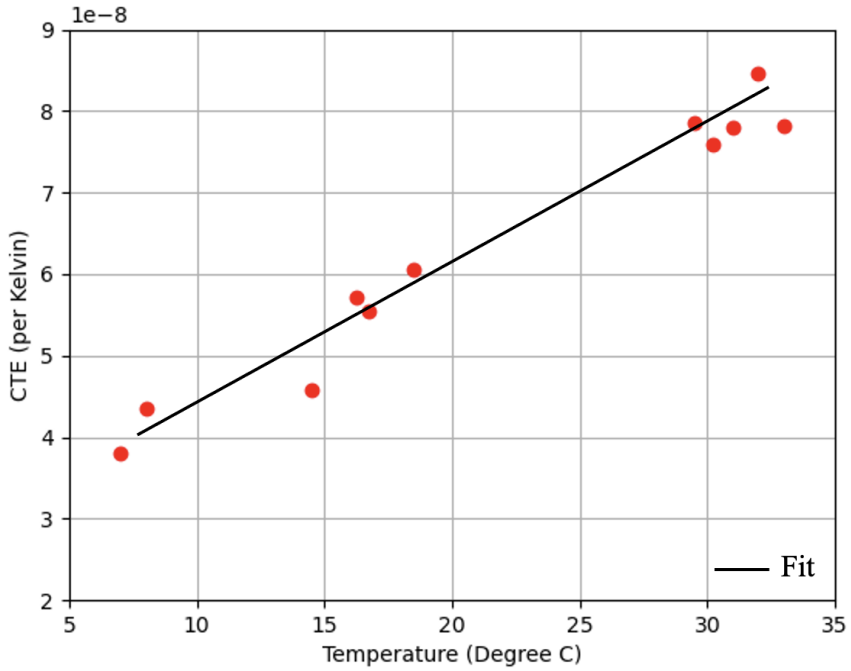

Figure 4.16: Measurement of CTE ($\frac{\Delta f/\nu_{Laser}}{\Delta T}$) versus temperature for the USL.

From the Fig. 4.16, we observed no zero crossing or sign change in the beatnote frequency on a temperature range between 32°C and 5°C. Further temperature reduction was not possible due to limitations imposed by the temperature controller. Our investigation led us to suspect that the peltier element, responsible for temperature regulation inside the vacuum chamber and located at the bottom of the copper shield, was unable to effectively dissipate the generated heat during the cooling process. To facilitate further cooling, we introduced a heat sink beneath the vacuum chamber. We positioned four peltier elements on each side of the heat sink to enhance cooling efficiency. With these modifications in place, we were able to achieve a temperature of 5°C. Additionally, we implemented a fan to improve air circulation.

Despite these measures, we did not observe any sign change in the beatnote frequency, even at 5°C. A linear fit to these data points indicates a sign change at -20°C. We identified several

potential reasons for not achieving a zero crossing in the CTE for our cavity:

1. Accuracy of FEM simulations was compromised by the reduced size of the cavity, which measures 25 mm, in contrast to larger cavities exceeding 100 mm in length. The shift in CTE caused by the presence of fused silica on the entire spacer exceeded our expectations through the simulations, likely due to the smaller length of the cavity.

2. The temperature inside the vacuum chamber could pose a challenge. The temperature probe, located next to the peltier element on the copper shield, limited our ability to obtain an accurate measurement of the actual temperature of the cavity.

3. Additionally, we suspect inadequate heat dissipation from the peltier element inside the vacuum chamber.

4. The transmission of optical power from the laser to the cavity, with a magnitude of 100 μW, may contribute to cavity heating and cause a temperature discrepancy between the temperature probe reading beside the peltier element and the actual temperature of the cavity.

5. The ULE spacer's intrinsic CTE might differ from specifications, leading to a shift in the overall CTE of the composite cavity below 0°C.

Kindly acknowledge that these are hypotheses, requiring thorough investigation to understand the absence of the zero crossing. Potential steps involve cooling the cavity below 0°C using a low-power cryogenic cooler, implementing an improved vacuum chamber with superior heat dissipation, placing a temperature probe in close proximity to the cavity, and measuring the ULE spacer's intrinsic CTE without the mirrors. However, due to time constraints, these measures couldn't be executed during my thesis.

4.8.5 Phase Noise

Furthermore, an examination of the impact of phase noise on the cavity was conducted by analyzing the beatnote signal with the spherical cavity. The procedure encompassed two primary steps:

Initially, we assessed the phase noise of the cavity with the fiber link in its free-running state. Subsequently, we engaged the noise compensation for the fiber link and conducted a replication of the identical measurement. The Power Spectral Density (PSD) depicting phase noise in decibels relative to the carrier (dBc/Hz) as a function of Fourier frequency was measured for both scenarios. The comparative illustration is provided in Fig. 4.17

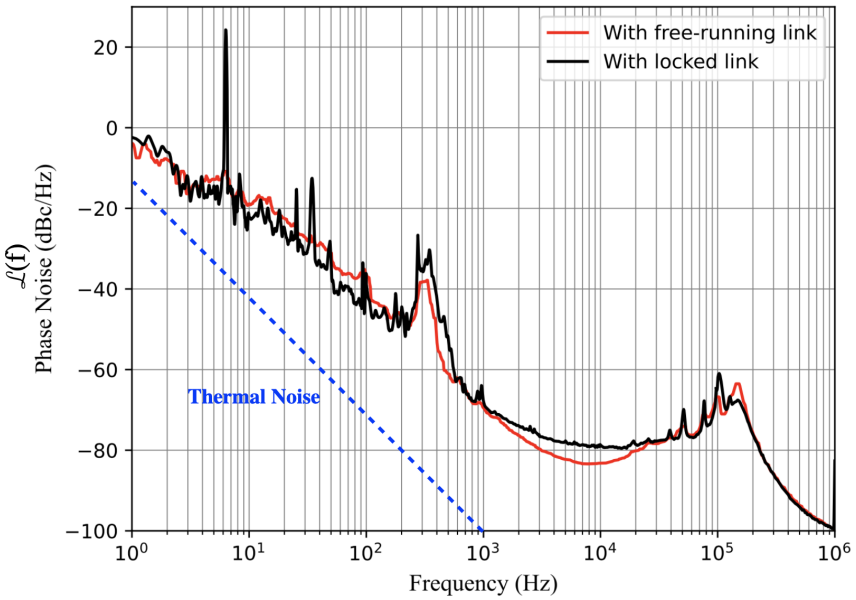

Figure 4.17: PSD of phase noise for the updated compact cavity. Red solid line represents the PSD of phase noise of the cavity measured with the free running link. Black curve represents the PSD of phase noise for the cavity with a noise compensated link.

We have achieved a commendably low phase noise level of -3.85 dBc/Hz at a Fourier frequency of 1 Hz with an f^{-2} slope that corresponds to a fractional frequency stability of 2.8×10^{-15} at 1 second integration time. An analysis of the phase noise curve highlights a noticeable increase in noise between 4 Hz and 250 Hz in the red curve. Remarkably, this elevated noise is reduced in the black curve, which corresponds to the PSD of phase noise when utilizing an active noise-compensated link. Our observation suggests that the noise may originate from the optical fiber responsible for signal transmission between the distinct rooms as we used a 25 m long optical fiber link in contrast to a tested 15 m long noise compensated optical fiber link. Increase in the size of the fiber link need more precise adjustments to the parameters governing the proportional-integral-derivative control of the PLL for the fiber link setup which could effectively mitigate and diminish this noise.

Furthermore, it's noteworthy that both the red and black curves manifest a distinct peak at 7 Hz. We attribute this peak to the inherent behavior of the control electronics at this specific frequency.

Upon comparing the PSD of phase noise between the new and old version of the cavities (blue curve) as detailed in Chapter 3, a noticeable variance in the slope of the PSD curve becomes apparent. The prior cavity exhibited an f^{-3} slope, whereas the current cavity displays an f^{-2} slope. This alteration in slope may be attributed to the utilization of a compact electronics configuration.

Concurrently, during the measurements conducted with the previous cavity version, the cavity rested solely on Viton pads without any applied holding force via the top viton ball utilizing the guided screw. By reducing the top viton ball applied force for the new cavity, it may be possible to further diminish the phase noise, potentially contributing to an enhancement in the slope of

the PSD curve.

4.8.6 Fractional frequency stability

A K&K frequency counter was utilized to measure the fractional frequency fluctuations of the laser. We determined the frequency of the beatnote between our USL and the USL synchronized to the spherical cavity, which possesses a fractional frequency instability of 2×10^{-15} at 1 second integration. The stability of the spherical cavity was measured in an independent experiment by beating with a cryogenic sapphire oscillator, ensuring its fractional frequency instability is well-characterized before use in our measurements. The resulting data was used to create a plot illustrating the Modified Allan Deviation (MDEV), shown in Fig. 4.18.

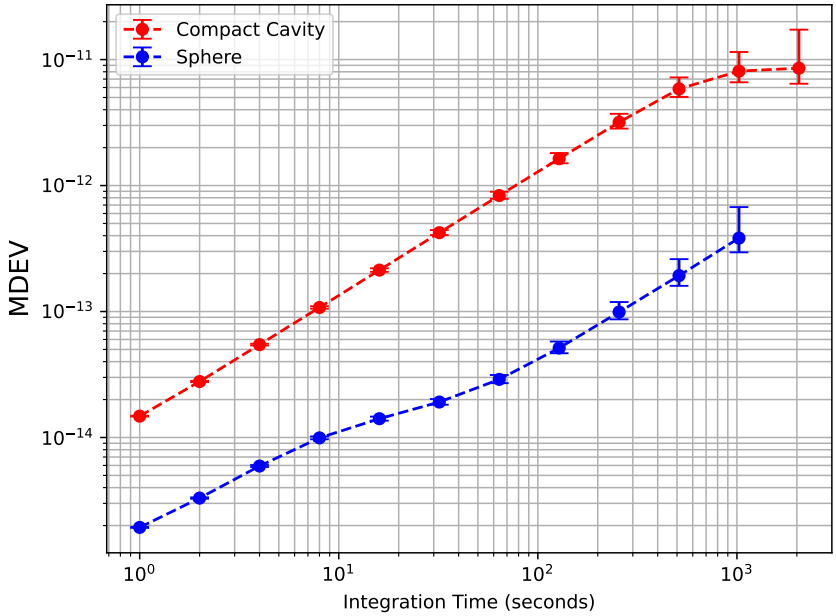

Figure 4.18: Modified Allan deviation of the compact cavity version 2 (red solid line). Blue solid line represents the modified Allan deviation for the reference, i.e., the spherical cavity.

Based on the data presented in Fig. 4.18, we attained a fractional frequency instability of 1×10^{-14} with a 1 second integration time. However, an increase in instability proportional to τ was observed for longer integration times. It is important to note that a linear drift was already removed from the frequency trace before calculating the MDEV. Despite this correction, the increase in instability proportional to τ persists, which suggests the presence of additional noise sources that could be influencing the long-term stability of our cavity. . It is worth noting that the anticipated instability of our cavity was 1×10^{-15} at a 1 second integration time. A comparative analysis against the thermal noise limit of the cavity (which stands at 1×10^{-15} for the same integration time) and the expected MVAR from the PSD of phase noise (amounting to 4×10^{-15} for a 1 second integration time) reveals a significant disparity among these values. The observed divergence in stability outcomes could be attributed to the following factors:

1. Optical Fiber Link Noise: The utilization of optical fiber links to transmit signals between rooms has introduced noise into our measurements. This noise is primarily attributed to the suspension of the fibers over tables, which may induce interference.

2. Electronics Interference: The PDH stabilization mechanism and the PLL electronics might be introducing noise due to insufficient shielding. Proper shielding measures could alleviate this issue.

3. Our operation at a temperature significantly deviating from the expected coefficient of thermal expansion zero crossing (T_0) for the cavity leads to length fluctuations within the cavity. This, in turn, can directly impact fractional frequency stability.

4. Lack of Passive Shielding: Absence of passive shielding for the vacuum chamber renders it susceptible to noise stemming from acoustic vibrations generated by room air conditioning systems.

To address these challenges and approach the thermal noise limit of our cavity, potential strategies include implementing robust shielding for electronics associated with PDH and PLL, particularly emphasizing the shielding of redpitaya boards. Operating in closer proximity to the cavity expected T_0 and introducing passive shielding for the vacuum chamber in the form of an enclosure could collectively contribute to enhanced stability.

It has been noted in Section 4.8.5 that a phase noise of -3.85 dBc/Hz for the cavity at 1 Hz Fourier frequency corresponded to an FFS of 4×10^{-15} at 1 second integration time. The difference in the observed FFS and the one through the phase noise can be mostly because of the noise generated by the compact version of the electronics. Proper shielding of the cables and use of specific filters can help improve the stability more.

4.9 Conclusion

In this concluding chapter, a transportable USL based on a compact Fabry-Pérot cavity was introduced. The revised design and mounting technique of the cavity were presented, alongside the rationale behind these updates.

The chapter offered an overview of the enhanced Fabry-Pérot cavity scheme, integrated with a 25 m long optical fiber link setup designed for transmitting the ultra-stable signal from the cavity between separate rooms. The concept and design of a compact power supply distribution system with minimal noise and substantial power capacity was also shown. This system catered to the power requirements of both the cavity and the link electronics.

A detailed examination of the integration process was provided, encompassing the incorporation of fiber optical components and electronics associated with the compact cavity and the optical fiber link setups. These components were seamlessly housed within two distinct 19-inch rack-mountable enclosures, alongside the compact power supply.

The chapter culminated in an in-depth analysis of the conducted measurements, including finesse measurements, mirror birefringence evaluations, coefficient of thermal expansion assessments, fractional frequency stability assessments, and phase noise measurements. Notably, a finesse of 625000 was achieved for this cavity—an achievement for a cavity equipped with crystalline-coated mirrors. Additionally, a phase noise of -3.8 dBc/Hz at 1 Hz Fourier frequency was attained, surpassing the previous cavity phase noise by 3.85 dBC/Hz at 1 Hz Fourier frequency. Moreover, the fractional frequency stability reached a level of 1×10^{-14} at 1 second integration time.

Notably, CTE zero crossing remained elusive, detailed along with possible explanations. Future work includes characterizing the whole transportable setup and conducting vibration sensitivity measurements, while further investigating the absence of CTE zero crossing.

Conclusion and Future Works

In conclusion, this work synthesizes the advancements in developing a transportable ultra-stable laser, featuring a room-temperature ULE Fabry-Pérot cavity and ultra-stable frequency transfer over fiber links. Key innovations include the adoption of digital phase-locked loops and the digital Pound-Drever-Hall method for frequency control, surpassing traditional analog techniques that not only enhance metrological applications but also set new standards for the integration of digital electronics in precision measurement technologies.

An aspect of this work involved the design, stabilization, and characterization of a 15 meter optical fiber link employing heterodyne Michelson interferometry and the incorporation of a digital phase-locked loop in various configurations underscored the challenges and solutions in achieving metrological level performances, especially in transporting signals from ultra-stable lasers or atomic clocks without compromising the frequency stability. This work also highlighted the crucial optimizations needed for enhancing the stability of fiber links, such as thermal shielding and the use of broadband RF baluns and H-MASERs as external clocks, despite challenges such as fiber length and optical noise. Digital PLLs, in particular, have been noted for their stability, flexibility, and adaptability, marking significant progress in the field. A low noise in terms of fractional frequency stability for the fiber link at 2×10^{-18} at 1 second integration time was measured for the fiber link. This result ensured easy transport of ultra-stable frequencies from state-of-the-art ultra stable lasers. Additionally, the implementation of a compact and transportable 19 inches rack mountable 25 m compact fiber link setup with an inbuilt compact and low noise power supply, designed for local signal transportation from an ultra stable laser, ensuring the preservation of frequency stability have also been demonstrated.

The second aspect of this work involved the development a transportable ultra-stable laser featuring a compact, 25 mm ULE Fabry-Pérot cavity, operating effectively at room temperature, and enhanced by advanced digital frequency stabilization using the Pound-Drever-Hall technique. The project involved the exploration of two different cavity designs: the first one, designed by Alexandre Didier. Severine Denis was responsible for the initial implementation of the digital PDH electronics for this USL, which I further optimized to significantly enhance system performance. My

contributions were focused on refining this digital PDH setup and investigating the reasons behind the missing CTE zero crossing. The application of the digital PDH frequency locking technique led to substantial improvements in system performance, most notably achieving a low phase noise of 3 dBc at a 1 Hz Fourier frequency with an f^{-3} slope in contrast to the previously measured f^{-2} slope.

Due to the absence of CTE zero crossing for the first version of the cavity, a subsequent version was designed and developed. This updated cavity retained the original design but omitted ULE rings from the mirrors and the spacer was fabricated from ULE with a known CTE. This modification was aimed at addressing the unexpected absence of CTE zero crossing—a key parameter for stabilizing cavity dimensional changes with temperature fluctuations, potentially caused by variability in the material composition of ULE or similar materials like Zerodur. The cavity housing was replaced with INVAR, a low thermal expansion material suitable for this purpose. Additionally, a 25 mm optical fiber frequency dissemination setup was integrated directly with the cavity, and the entire system was housed in two 19-inch rack-mountable boxes, housing the optical and electronics components for both the cavity and fiber link, making the setup both compact and transportable. A low-noise power supply was also designed to support the entire configuration and was incorporated into one of these boxes.

The new cavity setup achieved a fractional frequency stability of 1×10^{-14} at 1 second integration time and a phase noise of -3.85 dBc/Hz at 1 Hz Fourier frequency was measured for this cavity through the 25 mm optical fiber link by beating it with another USL based on a spherical cavity. Despite these improvements, the new cavity version also exhibited the absence of CTE zero crossing at room temperature, suggesting ongoing issues with material variability.

Future work will prioritize the characterization of the transportable USL setup, focusing on vibration and acceleration sensitivity measurements and identifying the reasons behind the missing coefficient of thermal expansion zero crossing. The cavity has been sent to the Physikalisch-Technische Bundesanstalt (PTB) in Braunschweig, Germany, for measurements of the ULE spacer's intrinsic CTE and to determine the effects of Fused Silica mirrors on the CTE zero crossing shift for the entire cavity. Further investigations will include a detailed analysis of the cavity electronic systems, as initial findings suggest electronic noise may be a limiting factor in achieving the cavity's thermal noise limit. Optimization of the digital phase-locked loop for the 25 meter optical fiber link and the Pound Drever Hall setup is essential for enhancing stability. The next phase involves integrating the entire transportable cavity and fiber link system into a mobile rack to assess its stability and phase noise performance in a compact, deployable configuration. This evaluation aims to understand the system's operational reliability under laboratory conditions. The setup will then undergo field testing to examine the impact of environmental factors on the laser frequency stability. This step will provide data on the system performance and adaptability in various conditions, contributing to the advancement of frequency stabilization technologies for practical applications.

This future research will systematically address current challenges and enhance the capabilities of USL systems for precision measurement and frequency stabilization, focusing on material properties, electronic noise reduction, and environmental robustness.

5 Appendix

5.1 Cavity Mount Design

5.1.1 Top Section

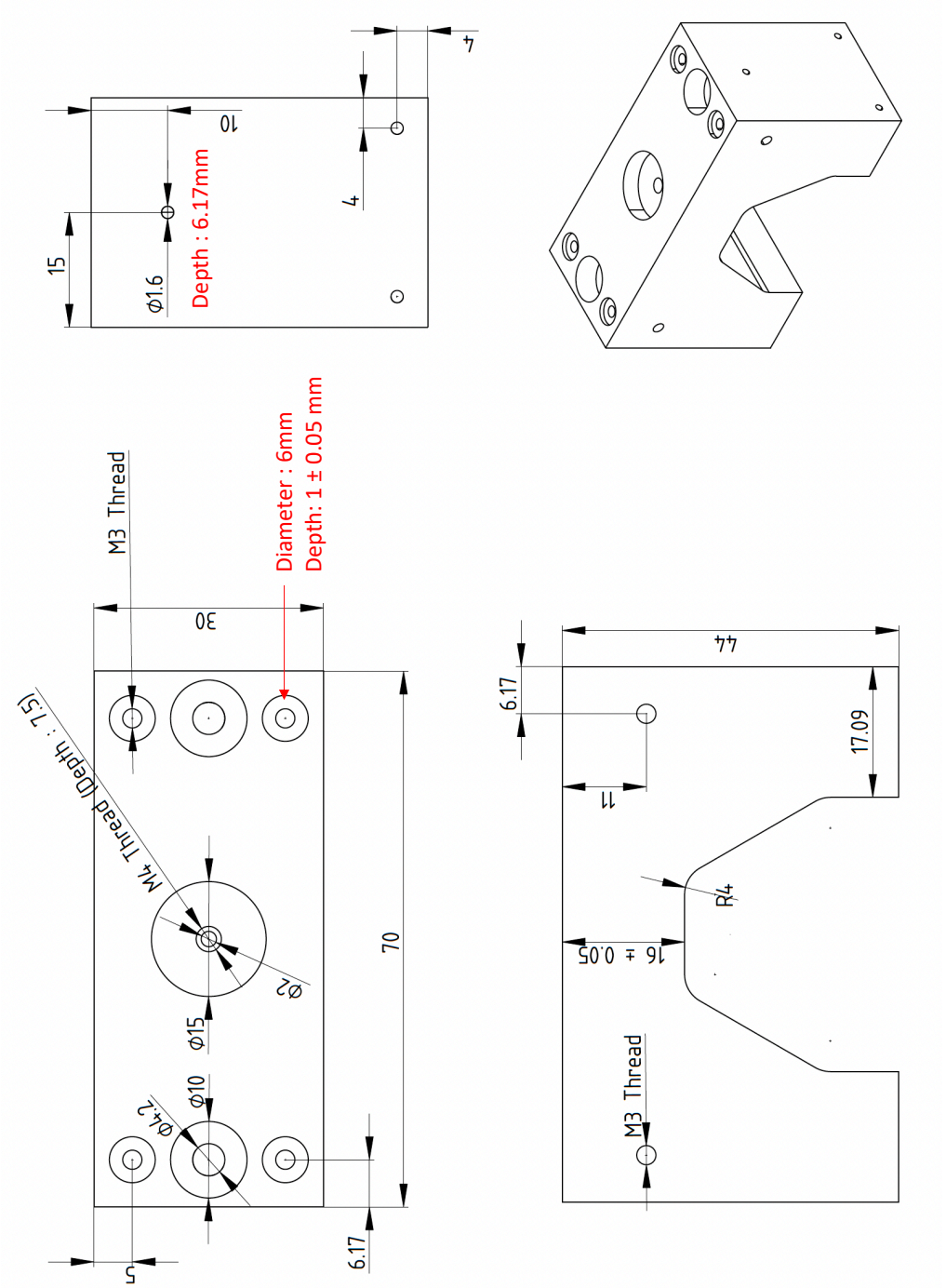

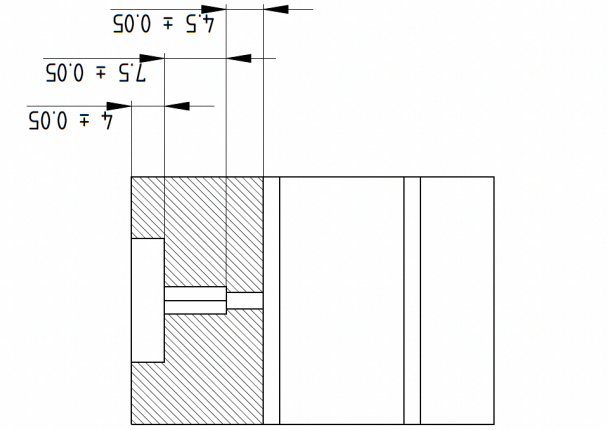
4.5 ± 0.05
7.5 ± 0.05
4 ± 0.05

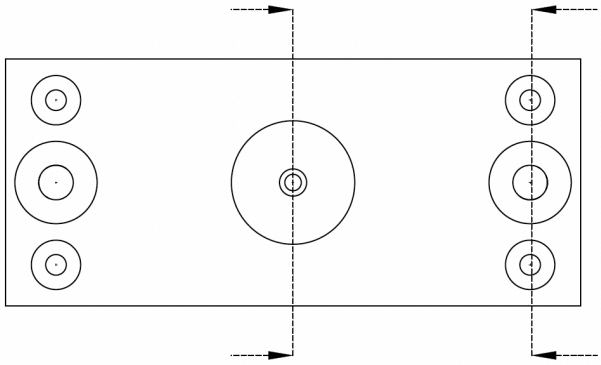

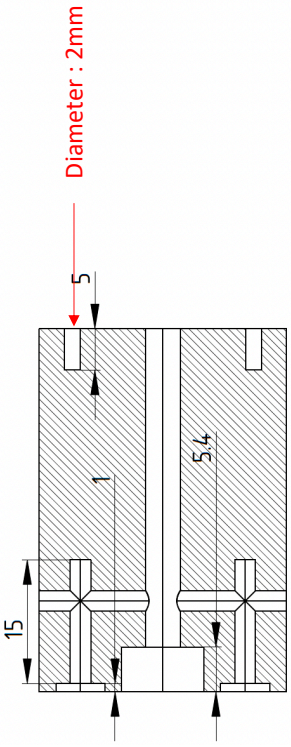
Diameter : 2mm
5
1
5.4
15

5.1.2 Bottom Section

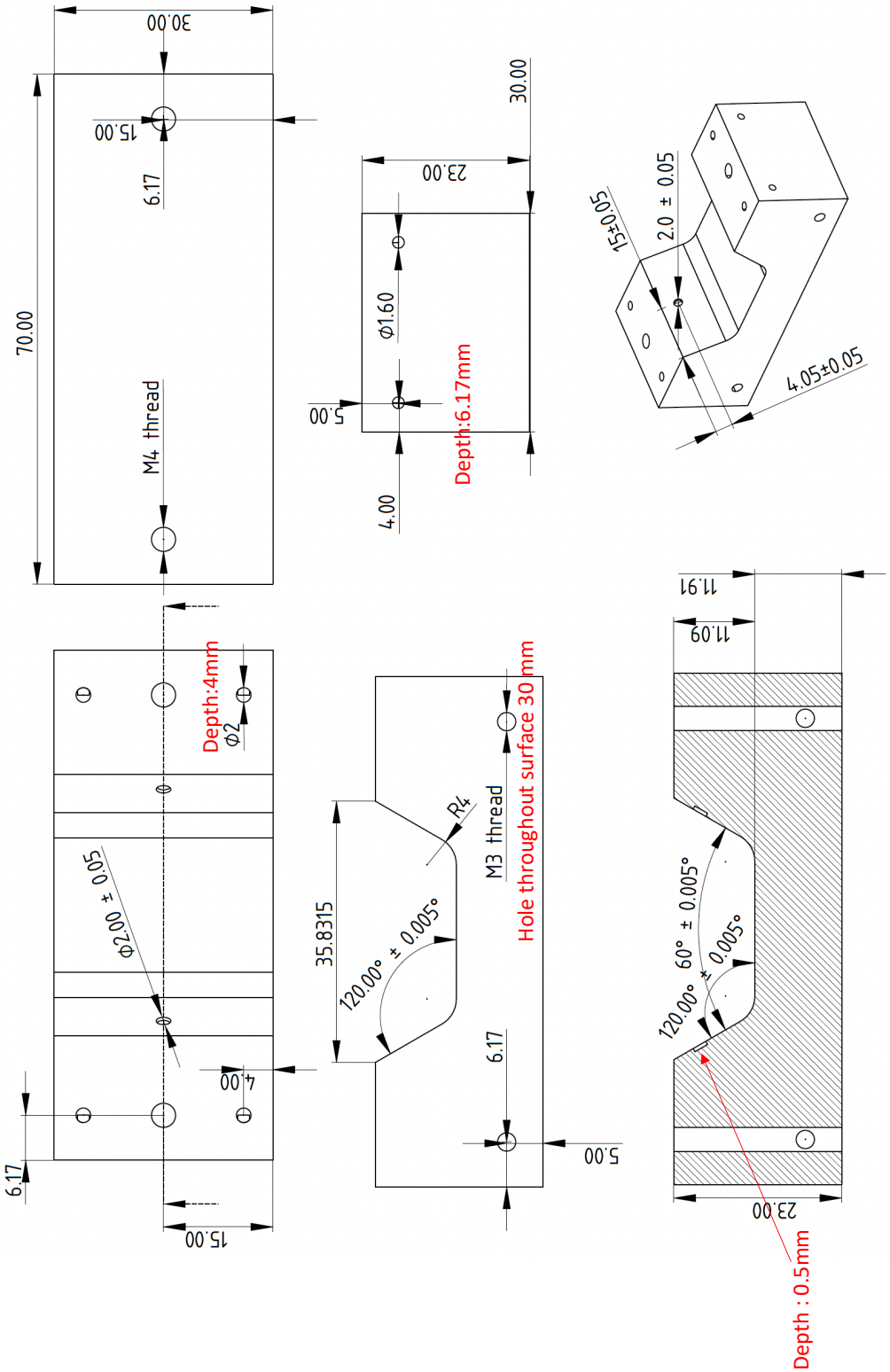

5.1.3 Guide

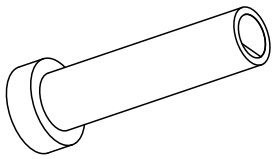

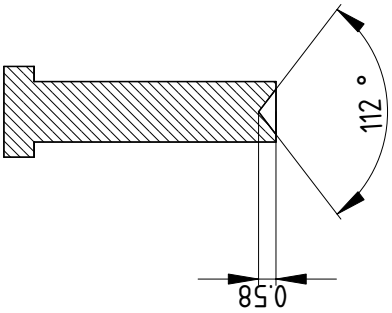

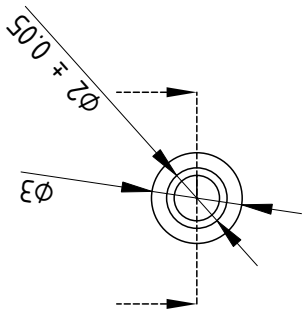

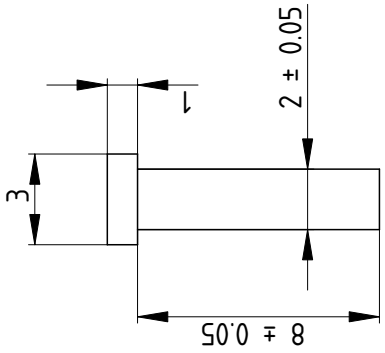

5.2 Compact Cavity Design

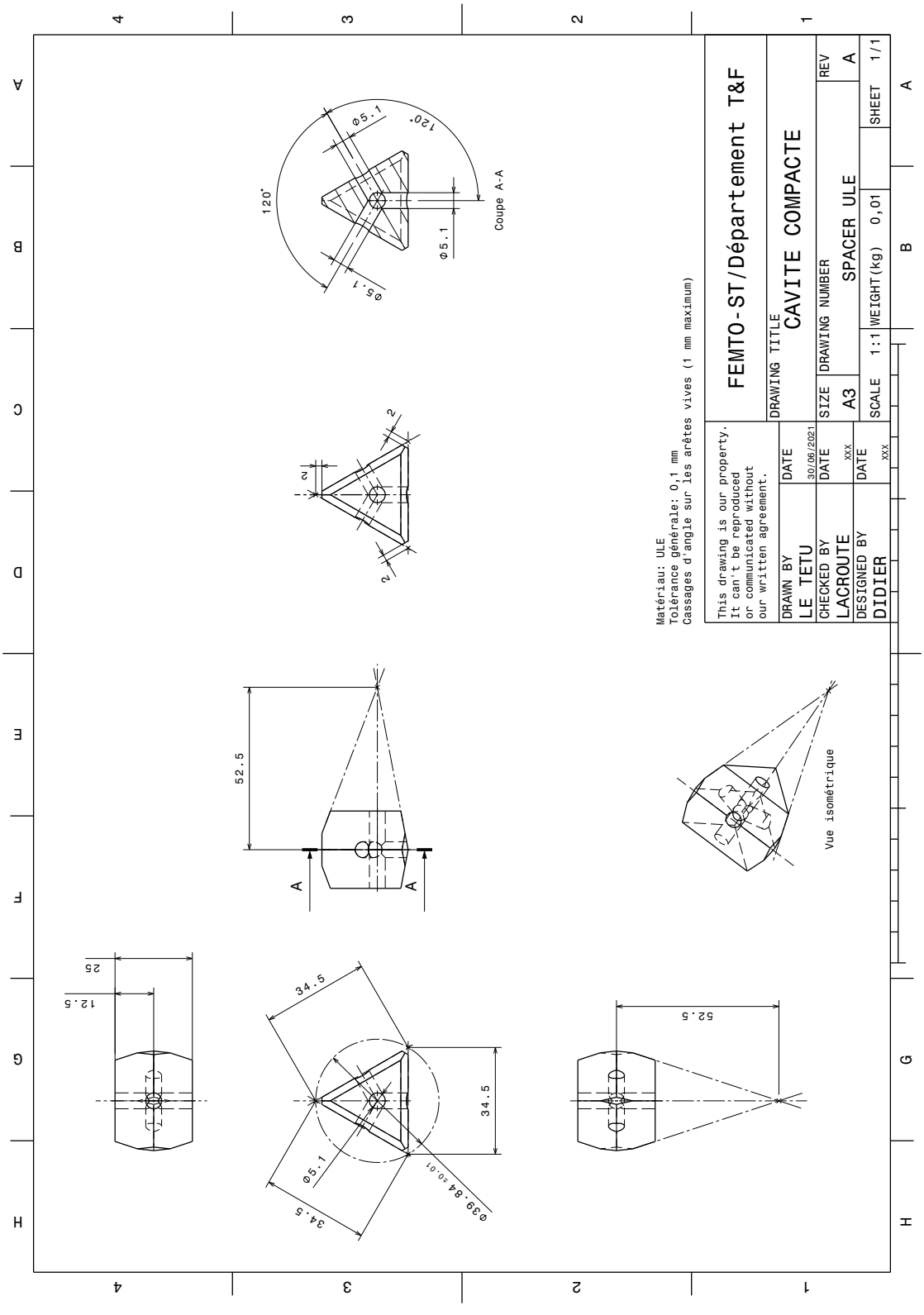

5.3 Compact Power Supply PCB Layout

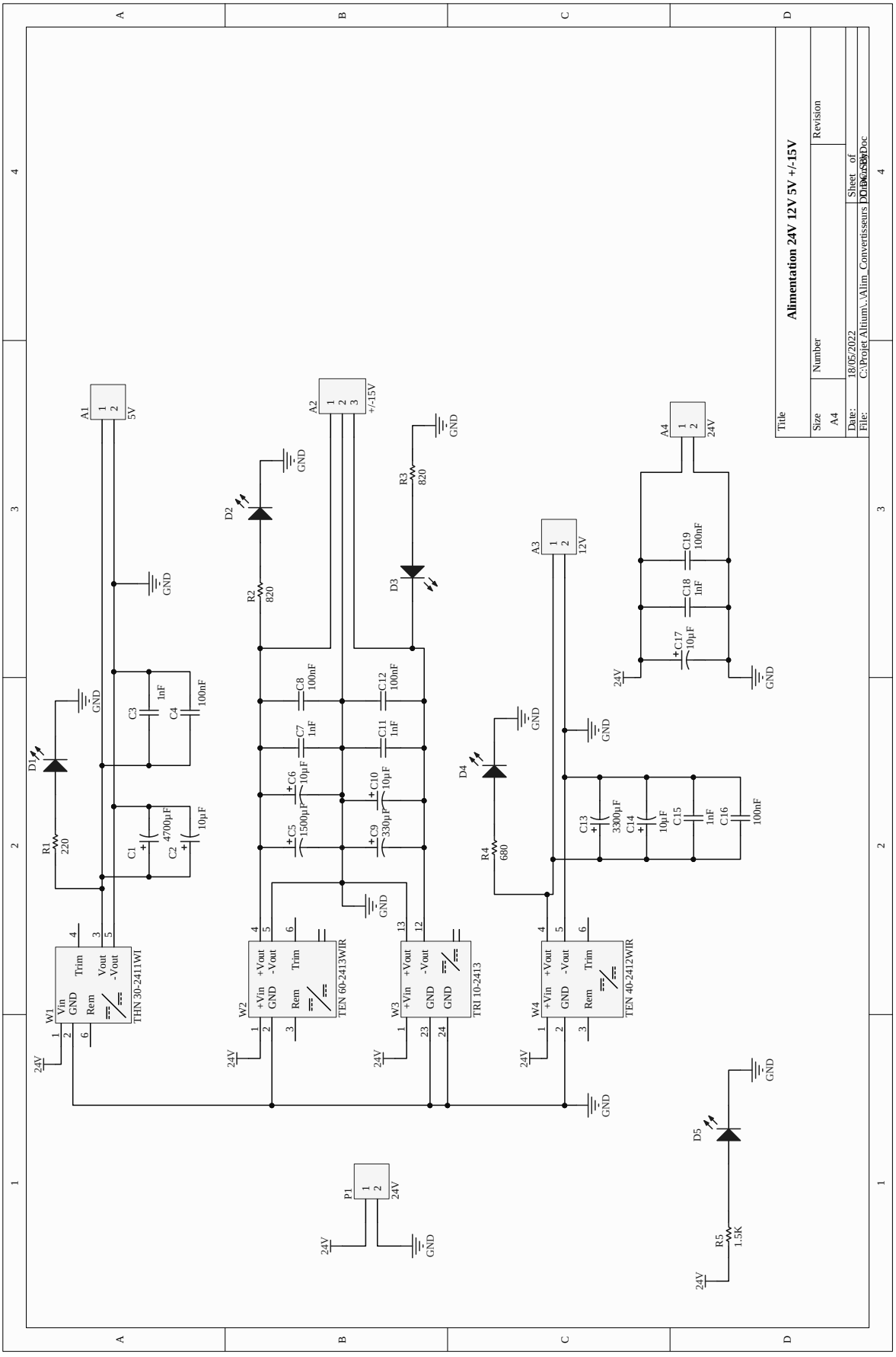

This article has been accepted for publication in IEEE Transactions on Ultrasonics, Ferroelectrics, and Frequency Control. This is the author's version which has not been fully edited and content may change prior to final publication. Citation information: DOI 10.1109/TUFFC.2021.3125066

Digital Doppler-cancellation servo for ultra-stable optical frequency dissemination over fiber

Shambo Mukherjee, Jacques Millo, Baptiste Marechal, Séverine Denis, Gwenhaël Goavec-Mérou, Jean-Michel Friedt, Yann Kersalé, Clément Lacroûte

***Abstract*—Progress made in optical references, including ultra-stable Fabry-Perot cavities, optical frequency combs and optical atomic clocks, have driven the need for ultra-stable optical fiber networks. Telecom-wavelength ultra-pure optical signal transport has been demonstrated on distances ranging from the laboratory scale to the continental scale. In this manuscript, we present a Doppler-cancellation setup based on a digital phase-locked loop for ultra-stable optical signal dissemination over fiber. The optical phase stabilization setup is based on a usual heterodyne Michelson-interferometer setup, while the Software Defined Radio (SDR) implementation of the phase-locked loop is based on a compact commercial board embedding a field programmable gate array, analog-to-digital and digital-to-analog converters. Using three different configurations including an undersampling method, we demonstrate a 20 m long fiber link with residual fractional frequency instability as low as 10^{-18} at 1000 s, and an optical phase noise of -70 dBc/Hz at 1 Hz with a telecom frequency carrier.**

I. Introduction

With the joint progress of ultra-stable Fabry-Perot (FP) cavities, optical frequency combs (OFCs) and atomic optical standards, the development of optical frequency references has reached both an unprecedented level of performances and an advanced degree of industrial integration. While laboratory FP cavities have reached the 10^{-17} level [1]–[5], many transportable prototypes have been developed [6]–[9] and several companies have developed FP-based ultra-stable lasers. OFCs have also become a wide-spread laboratory tool, and transportable models have been demonstrated [10]. Optical atomic clocks have shown the same level of progress, with both optical lattice and single-ion clocks reaching the 10^{-18} accuracy level and below [11]–[15].

This progress in ultra-stable optical references impacts many fields, including time and frequency metrology, precision spectroscopy, microwave photonics [16] and fundamental physics [17], [18]. Several proposals have argued for the development of ultra-stable optical fiber networks on the continental scale [19], [20]. Such networks are already being deployed within national and international frameworks. In practice, ultra-stable optical links have been implemented at several scales, from the laboratory or campus [21], [22] to inner- and inter-city links [23]–[25] and beyond, with long-haul fiber links [26]–[29].

Such ultra-stable fiber links are based on a heterodyne Michelson interferometer in which one of the arms is shortened to exhibit length fluctuations as small as possible. The second arm includes the required length to transfer the optical signal to the end-user. The resulting beatnote phase fluctuations are directly related to the length difference fluctuations between the reference arm and the optical fiber link. If the length of the reference arm is stable enough, phase fluctuations detected with a photodiode at the interferometer output corresponds to the link optical length fluctuations caused by vibrations and thermal perturbations. From this signal an active loop filter generates a compensation signal to cancel the link phase noise. This is the so-called Doppler-cancellation scheme [23], [30], [31], which can also work by post-processing the link phase fluctuations [32]. State-of-the-art long-haul optical fiber links reach a residual link fractional frequency stability in the 10^{-19} or below for integration times above 1000 s seconds, on distances of over 1000 km [27], [33]–[35].

In parallel to such advances, the recent years have seen the advent of digital-electronics in the fields of stabilized lasers, time-and-frequency metrology and atomic physics. With analog-to-digital and digital-to-analog converters (ADCs and DACs), field programmable gate arrays (FPGAs) and direct digital synthesis (DDSs) having reached levels of performance, integration and ease-of-use competitive with analog electronics including for radiofrequency (RF) applications, several laboratories and companies have started to move from analog to digital electronics control loops [36]–[39]. Such Software Defined Radio (SDR) setups bring the possibility to implement different schemes using the same hardware with the benefit of software long term stability and reconfigurability when implementing classical analog processing techniques, and enable the simple duplication of systems and electronic functions, the possibility to control many different channels in parallel with a high data rate and strong computing power, along with small components footprint. Beyond these advantages, discrete time digital signal processing brings a new paradigm illustrated here with sub-sampling and benefiting from high order Nyquist zones [40]. Digital implementation of the local oscillator as a numerically controlled oscillator (NCO), and mixing in the FPGA removes the classical analog challenges of local oscillator leakage through the mixer and I,Q imbalance when recovering the phase from a quadrature demodulation. This approach has led to numerous novel developments [41]–[47].

Among these approaches, Tourigny-Plante *et al.* use the CORDIC arctan algorithm to digitally extract the signal phase [45]. The phase-locked loop (PLL) is implemented on the same board used in this manuscript, clocked by its internal

The authors are with the FEMTO-ST Institute, univ. Bourgogne Franche-Comté, CNRS, ENSMM, 26 rue de l'Épitaphe, 25000 Besançon, France (e-mail: clement.lacroute@femto-st.fr).

This article has been accepted for publication in IEEE Transactions on Ultrasonics, Ferroelectrics, and Frequency Control. This is the author's version which has not been fully edited and content may change prior to final publication. Citation information: DOI 10.1109/TUFFC.2021.3125066

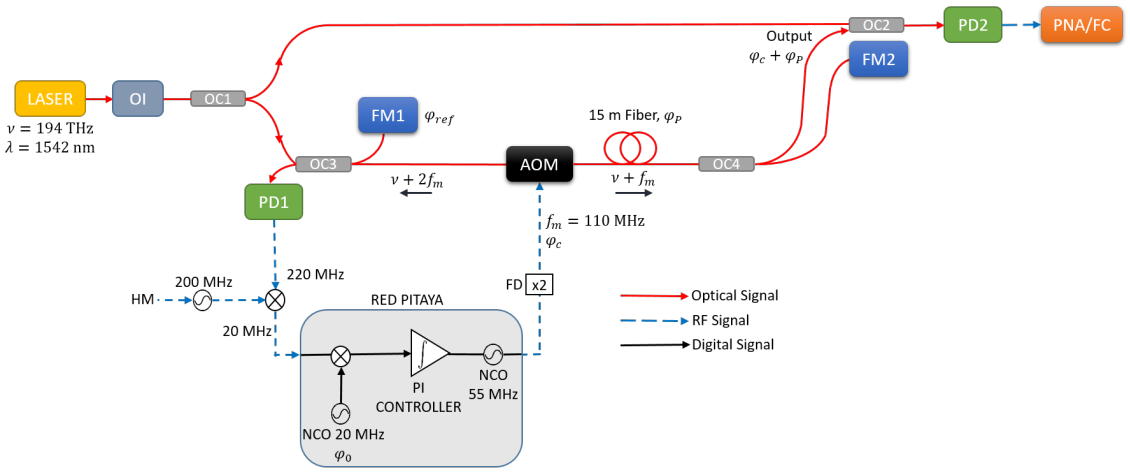

Fig. 1: Experimental scheme of the stabilized optical signal transfer through a 20 m long optical fiber link. The stabilization setup consists in a heterodyne Michelson interferometer (HMI) formed between optical coupler OC3 and the Faraday mirrors FM1 and FM2. Digital control of the optical phase measured at photodiode 1 (PD1) is performed through a digital phase-locked loop. Characterization of the link output phase noise is performed by comparison to the laser source through a Mach-Zehnder interferometer formed between optical couplers OC1 and OC2. Relevant frequencies and phases have been indicated. See text for details. HM: Hydrogen Maser, OI: Optical Isolator, OC: Optical Coupler, PD: Photodiode, AOM: Acousto Optic Modulator, PLL: Phase-Locked Loop, FM: Faraday Mirror, NCO: Numerically Controlled Oscillator.

quartz, using an open-source code available online [48]. The digital PLL is demonstrated on a Doppler-cancellation scheme similar to the one presented here and characterized in-loop. Another approach is presented by Cárdenas-Olaya *et al.*, using a tracking DDS scheme that is, to our knowledge, not openly documented [49]. The noise of the digital instrumentation has been carefully characterized [50] and demonstrated experimentally by two-way compensation of long-haul optical fiber links [51].

In this manuscript, we present a digitally controlled Doppler-cancellation setup developed to provide a stabilized fiber output to a compact FP cavity [52] on the laboratory scale. We have put the emphasis on simplicity using off-the-shelf optical components and a compact, digital electronics control loop. The digital control loop can be fully reproduced using the OSC-IMP environment, with all code being openly released under the CeCILL Licence [53]. As presented in the next Section, we rely on a simple demodulation scheme to access the signal phase noise, different from the arctan approach developed in [45] or the tracking DDS approach of [49]. While in-situ characterization of the Ref. [50] setup is implemented using two-way compensation [51], we present a more traditional Doppler-compensation setup with out-of-loop characterization. In addition to the standalone configuration of the digital board, presented also in [45], we characterize external referencing and undersampling using this board.

Section II presents the setup, including both the optical interferometers and the control electronics. Section III illustrates the results obtained in three different configurations, namely using a stand-alone digital board, an externally clocked digital board, and using undersampling. Section IV puts these results in perspective with the current state-of-the-art and applications of ultra-pure signal optical fiber transfer.

II. Methods

The aim of the setup is to transfer an ultra-stable signal at the laboratory scale (few tens of meters) using an optical fiber while maintaining the spectral purity and frequency stability of the signal. To do so, the main challenge is to reduce the phase disturbances caused by the thermal sensitivity and mechanical vibrations sensitivity of the optical fiber through the path of the link and to compensate these phase fluctuations using a PLL.

A. Principle of the compensated link

The link, including the noise compensation, is based on a heterodyne Michelson interferometer (HMI) scheme (Fig. 1) in which the beam splitter is the fiber coupler OC3. The short arm of the Michelson interferometer that defines the phase reference φ_{ref} of the link is formed between OC3 and the Faraday mirror FM1. The long arm used to transfer the optical reference that includes the 15 m of optical fiber is the path between OC3 and another Faraday mirror FM2 in which the phase is affected by environmental perturbations φ_P. This path includes an acousto-optical modulator (AOM) driven at $f_m \approx$ 110 MHz that adds a controlled phase φ_c to this arm. The optical coupler OC4 extracts the signal at the end of the link, with phase $\varphi_u = \varphi_P + \varphi_c$. The beatnote signal on PD1 carries the phase of the link at $2f_m \simeq 220$ MHz and

This article has been accepted for publication in IEEE Transactions on Ultrasonics, Ferroelectrics, and Frequency Control. This is the author's version which has not been fully edited and content may change prior to final publication. Citation information: DOI 10.1109/TUFFC.2021.3125066

is demodulated by an RF reference signal at $f_0 = 220$ MHz[1]. The error signal $\varepsilon = 2(\varphi_P + \varphi_c - \varphi_{ref}) - \varphi_0$ with φ_0 the contribution of this RF reference, vanishes when the loop filter is activated to compensate the noise of the link. Please note that the factor 2 comes from the double pass of the light in the two arms of the HMI. Thus the phase at the output of the link is $\varphi_u = \varphi_{ref} + \frac{1}{2}\varphi_0$. With this basic model we see that the noise compensation is ultimately limited by the phase fluctuations of the reference arm φ_{ref} and the RF reference φ_0. A more detailed analysis of the link various noise contributions can be found in [54].

B. Optical setup

The experiment is fed by a free-running, commercial fibre laser (NKT Photonics Koheras Adjustik, with a typical phase noise of 80 dBrad^2/Hz at 1 Hz) of wavelength $\lambda = 1542$ nm with about 14 mW optical output power. The 90/10 fiber beam splitter OC1 splits the laser into the two parts of the setup, with 10% going to the characterization part. The light is injected in the 15 m fiber through the 90/10 coupler OC3 using the 90%-port. At the end of the link the 90/10 coupler OC4 sends 90% to the output port and 10% to Faraday Mirror FM2. With this configuration 35% of the power injected in the link is transmitted to the end user (at the output point on Fig. 1) and the beatnote signal on PD1 is realized with 8.1% of the laser output power coming from the reference arm and 0.17% from the round trip. Should this be too low, this could be increased to 1.3% by using 50/50 couplers for OC3 and OC4, with an end user total transmission decreased to 11%.

Since the signal provided by the photodiode PD1 is processed by the PLL to phase lock the link (in-loop signal), it can not be used to evaluate the performances of the link. A dedicated part of the setup is implemented to characterize the signal transmitted by the link (Fig. 1). We use a heterodyne Mach-Zehnder interferometer (HMZI) formed between beamsplitters OC1 and OC2 to characterize the link output phase noise. One arm of the HMZI is formed by a short uncompensated fiber path between OC1 and OC2, while the second arm is formed by the ultra-stable link and its output fiber.

In practice, the evaluation of performances of the link requires to place the end close to the beginning. In order to passively reduce the effect of uncompensated fiber paths (OC1-OC2, OC1-OC3, OC3-FM1 and OC4-OC2, with a total length of 4.5 m), the entire setup except for the 15 m patch-cord is placed on a floated optical table and underneath a wooden box that provide passive acoustic isolation and thermal shielding from the room air conditioning residual temperature fluctuations.

Moreover, the uncompensated fiber path between OC4 and OC2 is partially corrected for by placing the FM2 close to OC2 and using the same length of fiber, so that thermal perturbation, fluctuating slowly, affect these two fibers similarly and the compensation matches the perturbations in the output fiber.

[1]Please note that in practice we use two different schemes, with cascaded analog and digital demodulation at 200 MHz and 20 MHz or direct digital demodulation of the 220 MHz beatnote.

The ultra-stable link performance is analyzed by characterizing the 110 MHz beatnote signal on PD2 using either a phase noise analyzer (PNA, Rohde & Schwarz FSWP) or a frequency counter (FC, K+K FXE) to quantify both phase noise and fractional frequency stability.

C. Control electronics

Our control electronics is centered on a digital PLL implemented on an FPGA integrated on a system on a chip (SoC). The commercial board (RP, Red Pitaya STEMlab 125-14) includes an analog to digital converter (ADC, 14 bits, 125 MS/s/channel, two channels), a digital to analog converter (DAC, 14 bits, 125 MS/s/channel, two channels) as well as the SoC including an embedded processor (Xilinx Zynq 7010). Fig. 2 sketches the electronics setup used in the two first measurements of this work. Modifications for the last step will be described in section III-C. Compliance with the Nyquist–Shannon theorem during sampling by the ADC, in addition to the front-end filters, requires downconverting the 220 MHz of the HMI beatnote signal to 20 MHz, below the Nyquist frequency $f_N = 62.5$ MHz of the ADC thanks to a 200 MHz signal source that is derived from an active hydrogen MASER (HM) using a DDS synthesizer. The resulting signal is filtered and amplified to provide a 11.6 dBm signal to the input connector of the board taking care to add a $50\ \Omega$ load in parallel to the high-impedance ADC input (the jumper on the board is positioned to the ± 1 V full scale).

The functions to process the signal for digital PLL are the same than with analog electronic: demodulation with a phase reference, low-pass filtering, loop filter and modulation of a controlled oscillator (see Fig. 2). Data provided by the 14-bits ADC, processed by these functions and sent to the DAC are signed and fed with a constant data rate of 125 MS/s. A 16-bits amplitude and 40-bits phase accumulation register NCO is the phase reference of the phase-locked loop. The demodulation is implemented with a multiplication process with a 14 bits output followed by a finite impulse response (FIR) filter configured with 25 coefficients each encoded in 16 bits.

In this manner, the signal recorded from the ADC at baseband is frequency transposed by the multiplication with the complex NCO acting as an ideal mixer that avoids the classical imbalance and lack of quadrature issues found in hardware implementations. The phase detector is a complex to real part converter since no gain was observed when using the more time and resource consuming arctan CORDIC implementation which would extend the linearity range to large phase offsets. In this short link investigation, no phase slip was observed once the lock is activated, and the setpoint remains in the locally linear behaviour of the complex to real phase detector. Using the CORDIC implementation might be necessary for implementing longer links, to ensure linearity and avoid cycle slips.

The FIR filter cutoff frequency is 4 MHz with more than 40 dB rejection for frequencies above 14 MHz. The FIR output is a 32 bits data stream. A dynamic shifter is then used to reduce the number of bits to 14 before the loop filter

This article has been accepted for publication in IEEE Transactions on Ultrasonics, Ferroelectrics, and Frequency Control. This is the author's version which has not been fully edited and content may change prior to final publication. Citation information: DOI 10.1109/TUFFC.2021.3125066

while adapting the range to the signal dynamics on the fly for the generation of the correction signal. The output is added to a constant value used to bias the frequency of the output DDS based on a second NCO. Then, data are sent to the channel 1 of the DAC. As the Nyquist-Shannon sampling theorem must also be satisfied for this converter, the NCO center frequency is set at 55 MHz and then the signal is frequency doubled, filtered and amplified to drive the AOM, which then corrects the optical fiber link phase fluctuations. Another DDS is implemented in the FPGA-chip based on a third NCO that outputs to channel 2 of the DAC. For most measurements presented below, this allows us to determine the digital phase reference contribution to the lock performance. The NCOs are implemented as 40 bits accumulators clocked at a rate of 125 MHz, leading to a $125 \cdot 10^6/2^{40} \simeq 0.11$ mHz resolution. The accumulator feeds a lookup table generating a sine wave encoded with 4096 values matching the 12-bit DAC resolution.

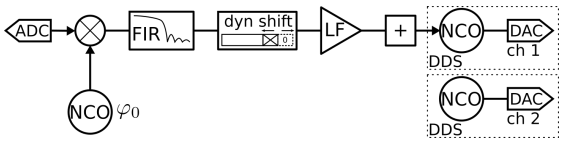

Fig. 2: Digital control scheme. The digital board offers two parallel channels. The two channels are similar and benefit from the digital implementation of duplicating functionality, emphasizing the flexibility of the SDR approach. We use the first one for locking. The second channel is used as a DDS for the experiments presented here. The design is based on separate blocks each representing a function. ADC: analog to digital converter. NCO: numerically controlled oscillator. FIR: finite impulse response filter. dyn shift: dynamic shifter (adds or removes least significant bit(s), set on-the-fly by user). LF: loop filter (proportional integrator function). See text for details.

Details and designs can be found here: https://github.com/oscimp/app/tree/master/redpitaya/double_iq_pid_vco

The embedded processor is used to run a GNU/Linux operating system (OS) dedicated to these applications (Buildroot). A digital signal processing framework dedicated to time & frequency metrology application has been developed and is available to the community at https://github.com/oscimp/oscimpDigital providing a consistent set of the real time signal processing blocks configuring the FPGA, the Linux drivers communicating with hardware, and the userspace libraries providing the flexibility of a user friendly interface for controlling the various processing blocks. This OS interfaces most of the basic functions described above, including network connectivity and file storage for long term logging as required for metrology application, and allows modifications of parameters by the users such as filter coefficients and DDS's frequencies. Among other features, a key one is the optimization of the resolution in agreement with the range of the error signal by using the dynamic shift register. This block selects 14 consecutive bits among the data 32 bits. The number of discarded lowest significant bits n is set by the user (where 18-n will be the number of discarded most significant bits). This reduction of the data size can be crucial since each single mathematical operation enlarges the number of bits required to losslessly encode the output.

Such an inflation of the number of bits in the data flow is not relevant because (i) it will rapidly surpass resources available in the FPGA, (ii) part of the lowest significant bits can often be neglected and (iii) the output DAC ultimately limits the resolution (14 bits for the RP).

This is also useful for adjusting the resolution when the input level range is changing. A high n will ensure that higher amplitude signals full dynamic is captured without overflows at the servo input, which is useful for monitoring the signal in open-loop (monitoring not shown in the circuit diagram), while a lower n guarantees a full resolution of the nearly vanishing error signal when the PLL is engaged.

As mentioned above, we use the characterization photodiode (PD2) to analyze the link output phase noise and fractional frequency stability carried by the 110 MHz beatnote. While the PNA input can directly analyze the 110 MHz signal phase-noise, the frequency counter input bandwidth is 60 MHz. When measuring fractional frequency stability, we thus mix the 110 MHz signal from PD2 with a 100 MHz signal from a synthesizer clocked by an HM in order to generate a 10 MHz signal.

III. Results

We present the results obtained with our setup, including both phase noise and fractional frequency stability. We have investigated three configurations based on the Figs. 1 and 2 general scheme. In §III-A, we use a stand-alone board, and all the digital electronics controls are clocked by the board internal quartz oscillator. In §III-B, we use the same scheme but this time adding a highly stable external clock to the digital electronics board. In §III-C, the Fig. 1 scheme is slightly modified as we implement undersampling, again using an external clock.

A. Using the board internal quartz oscillator

In this section, we use the board internal quartz oscillator to clock the digital controls. The results obtained are shown in Fig. 3.

Fig. 3 (a) shows the fractional frequency stability (FFS, estimated by the modified Allan deviation) of the free-running (black solid circles) and locked (red solid squares) PD2 signal. The locked link stability starts at around 8×10^{-18} at 1 s with an initial $\tau^{1/2}$ slope, followed by a 3×10^{-17} plateau until 1000 s and a linear frequency drift for longer integration times. The correction provides more than a factor of 10 instability reduction between 1 s and 1000 s, while the link instability is reduced by a factor 50 at 1 s.

In order to determine the contributions of the digital control board to the link performances, we have also monitored the NCO phase fluctuations with the DDS implemented on the channel 2 of the DAC set to 55 MHz for free-running measurements and to 20 MHz when the lock is engaged. In open-loop, the 55 MHz frequency noise will be multiplied

This article has been accepted for publication in IEEE Transactions on Ultrasonics, Ferroelectrics, and Frequency Control. This is the author's version which has not been fully edited and content may change prior to final publication. Citation information: DOI 10.1109/TUFFC.2021.3125066

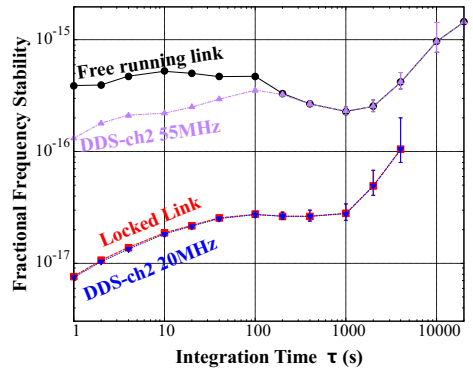

(a)

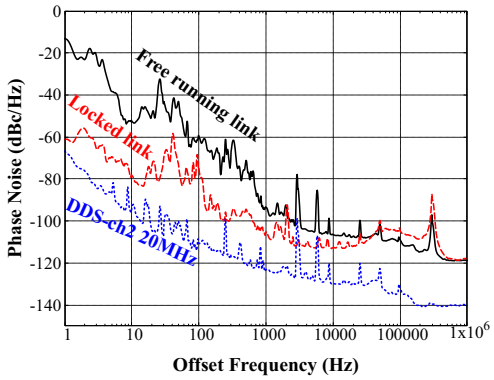

(b)

Fig. 3: Stand-alone digital configuration. (a) Fractional frequency stability of free running link (solid black circles), locked link (solid red squares), 55 MHz RP output (solid purple triangles), 20 MHz output (solid inverted blue triangles). (b) Phase Noise of free running link (black straight line), locked link (red dashed line), 20 MHz output (blue dotted line). All RP signals are normalized to the 194 THz carrier frequency.

by 2 at the board output. In closed-loop, the 20 MHz NCO frequency fluctuations are divided by 2 through the control loop at the user end (see II-A). To analyze their contributions, we scale the 55 MHz and 20 MHz signals by multiplying their frequency fluctuations by 2 and 0.5, respectively, and normalize them by 194 THz for FFS plots.

The FFS of the 55 MHz signal shows that the DDS used to drive the AOM is limiting for integration times longer than 200 s when the link is free running. This phase fluctuation is cancelled when the loop is closed and we see that the FFS of a 20 MHz signal scaled to the link output frequency overlaps with the stabilized link FFS indicating that the phase reference of the PLL φ_0 is the limitation. The corresponding DDS FFS at 20 MHz is around 1.6×10^{-10} at 1 s, consistent with the measurement presented in [55].

Fig. 3 (b) shows the single-sideband phase noise spectrum of the free-running (black line) and locked (red dashed line) PD2 signal. The locked link instability is -60 dBc/Hz at 1 Hz, reaching a -110 dBc/Hz floor around 10 kHz. The lock bandwidth is ≈ 40 kHz.

Please note that the NCO contribution at the link output is of about -66 dBc/Hz at 1 Hz. If we scale this back to the digital board clock frequency, this corresponds to -31 dBc/Hz at 1 Hz at 125 MHz. This is in good agreement with the RP internal quartz phase noise presented in [55]. This implies that the NCO performance is entirely determined by the board internal quartz, justifying the use of an external clock for improved performance.

B. Using the board clocked by an external clock

To further investigate the fundamental limitation of the RP we provide an external low noise 125 MHz clock signal to the digital control board. This signal is generated by a DDS clocked by an active HM, and is coupled to the board through a balun to respect impedance matching. The contribution of the clock signal is now estimated at 10^{-19} or below. The results are shown in Fig. 4.

Fig. 4 (a) shows the fractional frequency stability (estimated by the modified Allan deviation) of the free-running (black solid circles) and locked (red solid squares) PD2 signal when using an external clock. The locked link stability starts at around 2×10^{-18} at 1 s with a 8×10^{-18} bump at ten seconds, and then reaches a floor below 10^{-18}. The link instability is reduced by a factor 100 from 1 s to 400 s.

Fig. 4 (b) shows the single-sideband phase noise spectrum of the free-running (black line) and locked (red dashed line) PD2 signal when using an external clock. The locked link phase noise is below -70 dBc/Hz at 1 Hz, reaching a -110 dBc/Hz floor around 10 kHz. The lock bandwidth is ≈ 40 kHz, as in the previous section. The NCO contribution is again consistent with the external clock phase noise measured by [55].

C. Implementing undersampling with the Red Pitaya

In this section, we use undersampling in order to directly extract the phase noise from the 220 MHz output of the lock photodiode PD1. To do so, we have patched the commercial board by bypassing the anti-aliasing filters to directly send the signal to the sample and hold of the ADC (this would be unnecessary for boards such as the STEMlab 122-16 with direct RF sampling up to 550 MHz). The board unbalanced to balanced amplifier that acts as a low pass filter is replaced by a passive balun transformer, so as to benefit from the full 750 MHz bandwidth of the LTC2145 analog to digital converter frontend. This enables undersampling the signal, under the strong assumption of a pure and known beatnote frequency; this is mandatory for recovering the useful signal when it does not comply with the Nyquist–Shannon theorem.

We use this method to avoid the use of a mixer and synthesizer at the output of PD1. In addition to removing these potential noise and aging sources, the local oscillator phase is unknown at startup, whereas the ADC is readily frequency and phase synchronized over a network disseminating time and frequency information. Thus, undersampling allows for

This article has been accepted for publication in IEEE Transactions on Ultrasonics, Ferroelectrics, and Frequency Control. This is the author's version which has not been fully edited and content may change prior to final publication. Citation information: DOI 10.1109/TUFFC.2021.3125066

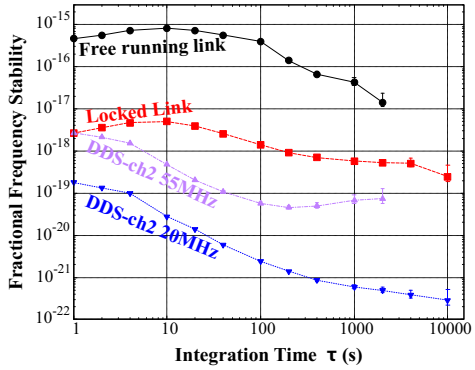

(a)

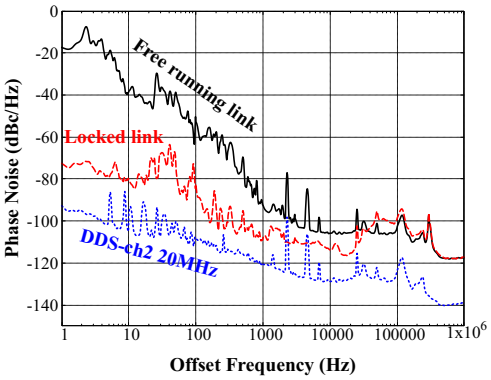

(b)

Fig. 4: External clock digital board configuration. (a) Fractional frequency stability of free running link (solid black circles), locked link (solid red squares), 55 MHz RP output (solid purple triangles), 20 MHz output (solid inverted blue triangles). (b) Phase Noise of free running link (black straight line), locked link (red dashed line), 20 MHz output (blue dotted line). All RP signals are normalized to the 194 THz carrier frequency.

coherent acquisition on the large scale of a laboratory. As shown Fig. 5, we filter and amplify the photodiode signal and send it directly to the modified board. With an external clock at 125 MHz, we work in the second Nyquist band of the input ADC. As a result, the 220 MHz signal is read as a $2 \times 125 - 220 = 30$ MHz sine wave. We demodulate this aliased signal using a 30 MHz NCO. The rest of the setup is unchanged compared to previous sections.

The fractional frequency stability and the phase noise measurements are shown in Fig. 6 by the dashed curves.

Fig. 6 (a) shows the fractional frequency stability (estimated by the modified Allan deviation) of the free-running (black open circles) and locked (red open squares) PD2 signal for the undersampling scheme. The locked link stability starts at around 6×10^{-18} at 1 second with a 4×10^{-18} bump at ten seconds, and then reaches a floor below 10^{-18}. There is a

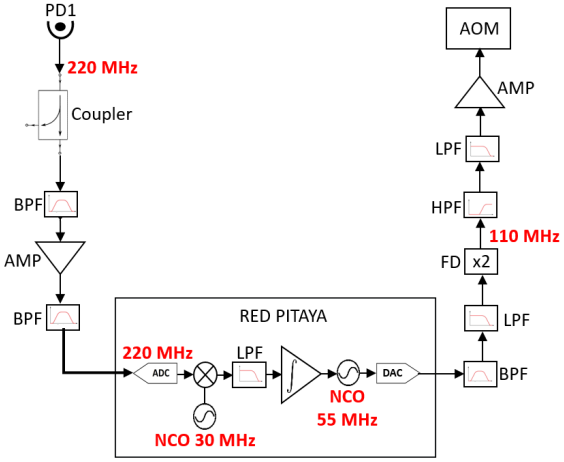

Fig. 5: Control electronics, undersampling servo loop setup. Fluctuations carried by the 220 MHz signal are directly sampled by a Red Pitaya to implement a PLL. Corrections are carried by the 110 MHz signal driving the AOM. See text for details.
PD: Photodiode, LPF: Low Pass Filter, HPF: High Pass Filter, BPF: Band Pass Filter, AMP: Amplifier, FD: Frequency Doubler. The coupler is for monitoring purposes only.

1/100 reduction of the link instability from 1 s to 200 s.

Fig. 6 (b) shows the single-sideband phase noise spectrum of the free-running (black dashed line) and locked (red dashed line) PD2 signal for the undersampling scheme. The locked link instability is -70 dBc/Hz at 1 Hz, reaching a -110 dBc/Hz floor around 10 kHz. The lock bandwidth in this configuration is around 70 kHz.

IV. Discussion

The results obtained with a commercial board-based digital control for a Doppler-compensation scheme are very promising for a wide range of applications that require the local distribution of an optical frequency reference signal.

The measured locking bandwidth for all configurations is between 40 and 70 kHz. With our link length of about 20 m in total, the one-way optical delay τ_{link} is about 100 ns, which determines the best achievable, link-delay-limited bandwidth of $1/(8\times\tau_{link}) \approx 1.25$ MHz (assuming a $\pi/4$ phase margin). The digital board main delay stems from the FIR, and is estimated to be at most 136 ns for our 25-coefficients filter. Lastly, the analog electronics and AOM contribution to the delay is of about 1 μs. With this total 1.236 μs delay, the maximum achievable bandwidth in our configuration is around 100 kHz.

Using a stand-alone board, the fractional stability performance is compatible with compact ultra-stable cavity setups, which have demonstrated fractional frequency stabilities in the range of 10^{-15} as well as ultrastable FP cavities with stabilities in the range of 10^{-16} and slightly below. It is however not

This article has been accepted for publication in IEEE Transactions on Ultrasonics, Ferroelectrics, and Frequency Control. This is the author's version which has not been fully edited and content may change prior to final publication. Citation information: DOI 10.1109/TUFFC.2021.3125066

suitable for the best current FP cavities or atomic clocks. For applications where the optical signal transmitted through the link would serve as a microwave photonics source, the measured phase noise is remarkably low. Assuming perfect division to 10 GHz, the measured phase noise contribution of the link would be -155 dBc/Hz at 1 Hz, with a -205 dBc/Hz floor.

Using an external clock pushes the setup performance towards state-of-the-art, and its residual fractional frequency instability is sufficient to transfer signals at the level of the best FP-based ultrastable lasers in the low 10^{-17}. When using an active HM as a reference, the digital board clock performance will actually be limited by its internal PLL residual noise [55]. According to [55], using instead a 10 MHz reference signal would degrade the SoC PLL residual noise by roughly a factor of 2. Given the typical performance of GPS-disciplined Rb standards, this would still guarantee a link fractional frequency stability well below 10^{-17} at 1 s and a negligible NCO contribution at longer integration times.

Our measured stabilized link performance is however not suitable for the transfer of the signal from state-of-the art optical clocks, with instabilities starting at 10^{-16} or below and integrating as $\tau^{-1/2}$. The measured noise of our setup seems to show a floor near 1000 s which is close to the performance of these clocks. We however believe that the measured fractional frequency stability is limited by our HMI setup rather than the link, and that etalon effects due to the absence of a second AOM near the FM could explain the measured instability. This could be tested in the future to verify that the presented setup is compatible with today's best optical atomic clocks. As our setup is mostly targeted towards compact, less-demanding applications, we have not tried to improve the setup limit. It is clear that the digital board itself should not limit the setup performance even for state-of-the art performance, as the NCO contribution is below 10^{-18} at all integration times and integrates down to the 10^{-22} range. Moreover, the ADC flicker phase noise is about -109 dBc/Hz at 1 Hz, with a floor at -146 dBc/Hz, even for a 220 MHz input frequency, as shown in [56]. This makes the ADC phase noise contribution well below the best phase noise reported here.

As shown in Fig. 6, the undersampling setup provides the same results as the regular externally clocked board, with a simpler setup.

The ch. 2 DDS output is also useful as an indication of the digital board performance. As described in section III-A, the in-loop and out-of-loop NCO contributions are scaled differently, by a factor of 0.5 and 2 respectively. Assuming they have identical FFS determined by the board clock FFS, their impact at the optical carrier frequency should differ by a ratio of $4 \times 55/20 = 11$. However, we observed that this ratio ranges between 15 and 20 at 1 s for our measurements, while for longer integration times, different behaviors are observed. This seems to imply that the assumption of FFS determined only by the digital board clock fails, and that additional frequency noise is added by the NCO. While this is not a limitation for the purpose presented here, this should be explained and is currently under investigation.

V. Conclusion

We have implemented a Doppler-cancellation scheme for optical fiber link phase stabilization that relies on a digital servo-loop. Using a commercial digital control board in three different configurations, including using an external clock and undersampling. Using an external clock, the stabilized link is compatible with current state-of-the-art optical references. Using undersampling simplifies the setup while maintaining this level of spectral purity.

While the fractional frequency stability reached with our measurements could be improved by improving the optical setup, we have determined that the digital electronic board intrinsic noise would limit the performance to the low 10^{-22} range at 10000 s. This shows that low-cost, small footprint devices can be integrated to the most demanding metrological setups. All digital designs are available at

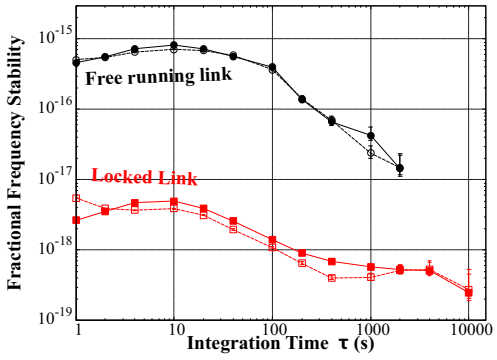

(a)

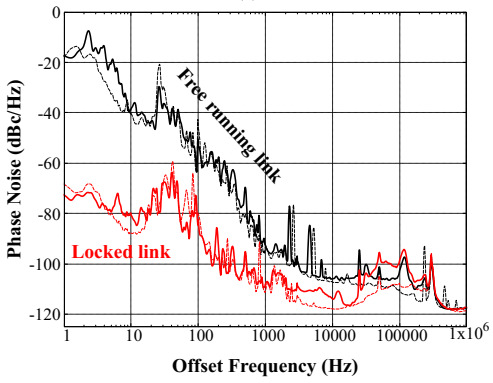

(b)

Fig. 6: (a) Comparison between the external clock (full symbols) and undersampling (with external clock) configurations, free running link with undersampled Red Pitaya (open black circles), locked link (open red squares). All RP signals are normalized to the 194 THz carrier frequency.
(b) Comparison between the Phase Noise of the link with undersampled Red Pitaya (red dashed, black dashed) and normal Red Pitaya (red straight, black straight).

https://github.com/oscimp/oscimpDigital and can therefore be easily duplicated.

VI. Acknowledgements

This work has been supported by the EIPHI graduate school (contract ANR-17-EURE-0002), the labex FIRST-TF (ANR-10-LABX-48-01), the EquipeX OSCILLATOR-IMP (ANR-11-EQPX-0033), the Région Bourgogne Franche-Comté, and the Centre National d'Études Spatiales (CNES, R&T R-S19-LN-0001-019).

Séverine Denis is now with CSEM, Rue Jaquet-Droz 1, 2002 Neuchâtel, Switzerland. Baptiste Marechal is now a Vision Engineer and Developer with Mikron SA, Route du Vignoble 17, 2017 Boudry.

The authors would like to thank Rodolphe Boudot and Marion Delehaye for their careful reading of the manuscript, as well as Léo Tranchart and Ivan Ryger for the FIR delay measurements.

References

[1] S. Häfner, S. Falke, C. Grebing, S. Vogt, T. Legero, M. Merimaa, C. Lisdat, and U. Sterr, "8×10^{-17} fractional laser frequency instability with a long room-temperature cavity," *Optics Letters*, vol. 40, no. 9, pp. 2112–2115, May 2015.

[2] D. Matei, T. Legero, S. Häfner, C. Grebing, R. Weyrich, W. Zhang, L. Sonderhouse, J. Robinson, J. Ye, F. Riehle, and U. Sterr, "1.5 μm Lasers with Sub-10 mHz Linewidth," *Physical Review Letters*, vol. 118, no. 26, p. 263202, Jun. 2017.

[3] W. Zhang, J. Robinson, L. Sonderhouse, E. Oelker, C. Benko, J. Hall, T. Legero, D. Matei, F. Riehle, U. Sterr, and J. Ye, "Ultrastable Silicon Cavity in a Continuously Operating Closed-Cycle Cryostat at 4 K," *Physical Review Letters*, vol. 119, no. 24, p. 243601, Dec. 2017.

[4] W. R. Milner, J. M. Robinson, C. J. Kennedy, T. Bothwell, D. Kedar, D. G. Matei, T. Legero, U. Sterr, F. Riehle, H. Leopardi, T. M. Fortier, J. A. Sherman, J. Levine, J. Yao, J. Ye, and E. Oelker, "Demonstration of a timescale based on a stable optical carrier," *Phys. Rev. Lett.*, vol. 123, p. 173201, Oct 2019.

[5] J. M. Robinson, E. Oelker, W. R. Milner, W. Zhang, T. Legero, D. G. Matei, F. Riehle, U. Sterr, and J. Ye, "Crystalline optical cavity at 4 K with thermal-noise-limited instability and ultralow drift," *Optica*, vol. 6, no. 2, pp. 240–243, Feb 2019.

[6] D. R. Leibrandt, M. J. Thorpe, J. C. Bergquist, and T. Rosenband, "Field-test of a robust, portable, frequency-stable laser," *Optics Express*, vol. 19, no. 11, pp. 10 278–10 286, May 2011.

[7] S. Vogt, C. Lisdat, T. Legero, U. Sterr, I. Ernsting, A. Nevsky, and S. Schiller, "Demonstration of a transportable 1 Hz-linewidth laser," *Applied Physics B*, vol. 104, no. 4, p. 741, Sep. 2011.

[8] B. Argence, E. Prevost, T. Lévèque, R. Le Goff, S. Bize, P. Lemonde, and G. Santarelli, "Prototype of an ultra-stable optical cavity for space applications," *Optics Express*, vol. 20, no. 23, pp. 25 409–25 420, Nov. 2012.

[9] S. Häfner, S. Häfner, S. Herbers, S. Vogt, S. Vogt, C. Lisdat, and U. Sterr, "Transportable interrogation laser system with an instability of mod $\sigma_y = 3 \times 10^{-16}$," *Optics Express*, vol. 28, no. 11, pp. 16 407–16 416, May 2020, publisher: Optical Society of America.

[10] M. Lezius, T. Wilken, C. Deutsch, M. Giunta, O. Mandel, A. Thaller, V. Schkolnik, M. Schiemangk, A. Dinkelaker, A. Kohfeldt, A. Wicht, M. Krutzik, A. Peters, O. Hellmig, H. Duncker, K. Sengstock, P. Windpassinger, K. Lampmann, T. Hülsing, T. W. Hänsch, and R. Holzwarth, "Space-borne frequency comb metrology," *Optica*, vol. 3, no. 12, pp. 1381–1387, Dec. 2016.

[11] N. Hinkley, J. A. Sherman, N. B. Phillips, M. Schioppo, N. D. Lemke, K. Beloy, M. Pizzocaro, C. W. Oates, and A. D. Ludlow, "An Atomic Clock with 10^{-18} Instability," *Science*, vol. 341, no. 6151, pp. 1215–1218, Sep. 2013.

[12] B. J. Bloom, T. L. Nicholson, J. R. Williams, S. L. Campbell, M. Bishof, X. Zhang, W. Zhang, S. L. Bromley, and J. Ye, "An optical lattice clock with accuracy and stability at the 10^{-18} level," *Nature*, vol. 506, no. 7486, pp. 71–75, Feb. 2014.

[13] I. Ushijima, M. Takamoto, M. Das, T. Ohkubo, and H. Katori, "Cryogenic optical lattice clocks," *Nature Photonics*, vol. 9, no. 3, pp. 185–189, Mar. 2015.

[14] N. Huntemann, C. Sanner, B. Lipphardt, C. Tamm, and E. Peik, "Single-Ion Atomic Clock with 3×10^{-18} Systematic Uncertainty," *Physical Review Letters*, vol. 116, no. 6, p. 063001, Feb. 2016.

[15] S. Brewer, J.-S. Chen, A. Hankin, E. Clements, C. Chou, D. Wineland, D. Hume, and D. Leibrandt, "$^{27}Al^{+}$ Quantum-Logic Clock with a Systematic Uncertainty below 10^{-18}," *Physical Review Letters*, vol. 123, no. 3, p. 033201, Jul. 2019.

[16] M. Giunta, J. Yu, M. Lessing, M. Fischer, M. Lezius, X. Xie, G. Santarelli, Y. L. Coq, and R. Holzwarth, "Compact and ultrastable photonic microwave oscillator," *Optics Letters*, vol. 45, no. 5, pp. 1140–1143, Mar. 2020, publisher: Optical Society of America.

[17] A. Derevianko and M. Pospelov, "Hunting for topological dark matter with atomic clocks," *Nature Physics*, vol. 10, no. 12, pp. 933–936, Dec. 2014.

[18] M. Safronova, D. Budker, D. DeMille, D. F. J. Kimball, A. Derevianko, and C. W. Clark, "Search for new physics with atoms and molecules," *Reviews of Modern Physics*, vol. 90, no. 2, p. 025008, Jun. 2018, publisher: American Physical Society.

[19] F. Riehle, "Optical clock networks," *Nature Photonics*, vol. 11, no. 1, pp. 25–31, Jan. 2017.

[20] C. Lisdat, G. Grosche, N. Quintin, C. Shi, S. M. F. Raupach, C. Grebing, D. Nicolodi, F. Stefani, A. Al-Masoudi, S. Dörscher, S. Häfner, J.-L. Robyr, N. Chiodo, S. Bilicki, E. Bookjans, A. Koczwara, S. Koke, A. Kuhl, F. Wiotte, F. Meynadier, E. Camisard, M. Abgrall, M. Lours, T. Legero, H. Schnatz, U. Sterr, H. Denker, C. Chardonnet, Y. L. Coq, G. Santarelli, A. Amy-Klein, R. L. Targat, J. Lodewyck, O. Lopez, and P.-E. Pottie, "A clock network for geodesy and fundamental science," *Nature Communications*, vol. 7, p. 12443, Aug. 2016.

[21] K. S. Kudeyarov, G. A. Vishnyakova, K. Y. Khabarova, and N. N. Kolachevsky, "2.8 km fiber link with phase noise compensation for transportable Yb^{+} optical clock characterization," *Laser Physics*, vol. 28, no. 10, p. 105103, Jul. 2018, publisher: IOP Publishing.

[22] K. Beloy, M. I. Bodine, T. Bothwell, S. M. Brewer, S. L. Bromley, J.-S. Chen, J.-D. Deschênes, S. A. Diddams, R. J. Fasano, T. M. Fortier, Y. S. Hassan, D. B. Hume, D. Kedar, C. J. Kennedy, I. Khader, A. Koepke, D. R. Leibrandt, H. Leopardi, A. D. Ludlow, W. F. McGrew, W. R. Milner, N. R. Newbury, D. Nicolodi, E. Oelker, T. E. Parker, J. M. Robinson, S. Romisch, S. A. Schäffer, J. A. Sherman, L. C. Sinclair, L. Sonderhouse, W. C. Swann, J. Yao, J. Ye, X. Zhang, and Boulder Atomic Clock Optical Network (BACON) Collaboration*, "Frequency ratio measurements at 18-digit accuracy using an optical clock network," *Nature*, vol. 591, no. 7851, pp. 564–569, Mar. 2021.

[23] N. R. Newbury, P. A. Williams, and W. C. Swann, "Coherent transfer of an optical carrier over 251 km," *Optics Letters*, vol. 32, no. 21, pp. 3056–3058, Nov. 2007.

[24] A. Bercy, F. Stefani, O. Lopez, C. Chardonnet, P.-E. Pottie, and A. Amy-Klein, "Two-way optical frequency comparisons at 5×10^{-21} relative stability over 100-km telecommunication network fibers," *Physical Review A*, vol. 90, no. 6, p. 061802, Dec. 2014, publisher: American Physical Society.

[25] E. Cantin, M. Tønnes, R. L. Targat, A. Amy-Klein, O. Lopez, and P.-E. Pottie, "An accurate and robust metrological network for coherent optical frequency dissemination," *New Journal of Physics*, vol. 23, no. 5, p. 053027, may 2021.

[26] O. Lopez, A. Haboucha, B. Chanteau, C. Chardonnet, A. Amy-Klein, and G. Santarelli, "Ultra-stable long distance optical frequency distribution using the Internet fiber network," *Optics Express*, vol. 20, no. 21, pp. 23 518–23 526, Oct. 2012.

[27] D. Calonico, E. K. Bertacco, C. E. Calosso, C. Clivati, G. A. Costanzo, M. Frittelli, A. Godone, A. Mura, N. Poli, D. V. Sutyrin, G. Tino, M. E. Zucco, and F. Levi, "High-accuracy coherent optical frequency transfer over a doubled 642-km fiber link," *Applied Physics B*, vol. 117, no. 3, pp. 979–986, Dec. 2014.

[28] O. Lopez, F. Kéfélian, H. Jiang, A. Haboucha, A. Bercy, F. Stefani, B. Chanteau, A. Kanj, D. Rovera, J. Achkar, C. Chardonnet, P.-E. Pottie, A. Amy-Klein, and G. Santarelli, "Frequency and time transfer for metrology and beyond using telecommunication network fibres," *Comptes Rendus Physique*, vol. 16, no. 5, pp. 531–539, Jun. 2015.

[29] C. Clivati, R. Aiello, G. Bianco, C. Bortolotti, P. D. Natale, V. D. Sarno, P. Maddaloni, G. Maccaferri, A. Mura, M. Negusini, F. Levi, F. Perini, R. Ricci, M. Roma, L. S. Amato, M. S. de Cumis, M. Stagni, A. Tuozzi, and D. Calonico, "Common-clock very long baseline interferometry using a coherent optical fiber link," *Optica*, vol. 7, no. 8, pp. 1031–1037, Aug 2020.

[30] L.-S. Ma, P. Jungner, J. Ye, and J. L. Hall, "Delivering the same optical frequency at two places: accurate cancellation of phase noise introduced by an optical fiber or other time-varying path," *Optics Letters*, vol. 19, no. 21, pp. 1777–1779, Nov. 1994.

[31] J. Ye, J.-L. Peng, R. J. Jones, K. W. Holman, J. L. Hall, D. J. Jones, S. A. Diddams, J. Kitching, S. Bize, J. C. Bergquist, L. W. Hollberg, L. Robertsson, and L.-S. Ma, "Delivery of high-stability optical and microwave frequency standards over an optical fiber network," *JOSA B*, vol. 20, no. 7, pp. 1459–1467, Jul. 2003.

[32] C. E. Calosso, E. K. Bertacco, D. Calonico, C. Clivati, G. A. Costanzo, M. Frittelli, F. Levi, S. Micalizio, A. Mura, and A. Godone, "Doppler-stabilized fiber link with 6dB noise improvement below the classical limit," *Optics Letters*, vol. 40, no. 2, pp. 131–134, Jan. 2015.

[33] F. Stefani, O. Lopez, A. Bercy, W.-K. Lee, C. Chardonnet, G. Santarelli, P.-E. Pottie, and A. Amy-Klein, "Tackling the limits of optical fiber links," *JOSA B*, vol. 32, no. 5, pp. 787–797, May 2015.

[34] S. M. F. Raupach, A. Koczwara, and G. Grosche, "Brillouin amplification supports 1×10^{-20} uncertainty in optical frequency transfer over 1400 km of underground fiber," *Physical Review A*, vol. 92, no. 2, p. 021801, Aug. 2015.

[35] N. Chiodo, N. Quintin, F. Stefani, F. Wiotte, E. Camisard, C. Chardonnet, G. Santarelli, A. Amy-Klein, P.-E. Pottie, and O. Lopez, "Cascaded optical fiber link using the internet network for remote clocks comparison," *Optics Express*, vol. 23, no. 26, pp. 33 927–33 937, Dec. 2015.

[36] R. Bowler, U. Warring, J. W. Britton, B. C. Sawyer, and J. Amini, "Arbitrary waveform generator for quantum information processing with trapped ions," *Review of Scientific Instruments*, vol. 84, no. 3, p. 033108, Mar. 2013, publisher: American Institute of Physics.

[37] K. Huang, H. Le Jeannic, J. Ruaudel, O. Morin, and J. Laurat, "Microcontroller-based locking in optics experiments," *Review of Scientific Instruments*, vol. 85, no. 12, p. 123112, Dec. 2014.

[38] T. Pruttivarasin and H. Katori, "Compact field programmable gate array-based pulse-sequencer and radio-frequency generator for experiments with trapped atoms," *Review of Scientific Instruments*, vol. 86, no. 11, p. 115106, Nov. 2015, publisher: American Institute of Physics.

[39] J. Stuart, R. Panock, C. Bruzewicz, J. Sedlacek, R. McConnell, I. Chuang, J. Sage, and J. Chiaverini, "Chip-Integrated Voltage Sources for Control of Trapped Ions," *Physical Review Applied*, vol. 11, no. 2, p. 024010, Feb. 2019, publisher: American Physical Society.

[40] E. Richter, "Usage of higher order nyquist zones with direct sampling devices," in *Software Defined Radio Academy (SDRA)*, 2020, https://www.youtube.com/watch?v=PI_ROLXqO_Q.

[41] C. J. Hasselwander, Z. Cao, and W. A. Grissom, "gr-mri: A software package for magnetic resonance imaging using software defined radios," *Journal of Magnetic Resonance*, vol. 270, pp. 47–55, 2016.

[42] J. A. Sherman and R. Jördens, "Oscillator metrology with software defined radio," *Review of Scientific Instruments*, vol. 87, no. 5, p. 054711, 2016.

[43] P. Mahnke, "Characterization of a commercial software defined radio as high frequency lock-in amplifier for fm spectroscopy," *Review of Scientific Instruments*, vol. 89, no. 1, p. 013113, 2018.

[44] F. F. Balakirev, S. M. Ennaceur, R. J. Migliori, B. Maiorov, and A. Migliori, "Resonant ultrasound spectroscopy: The essential toolbox," *Review of Scientific Instruments*, vol. 90, no. 12, p. 121401, 2019.

[45] A. Tourigny-Plante, V. Michaud-Belleau, N. Bourbeau Hébert, H. Bergeron, J. Genest, and J.-D. Deschênes, "An open and flexible digital phase-locked loop for optical metrology," *Review of Scientific Instruments*, vol. 89, no. 9, p. 093103, 2018.

[46] G. Stimpson, M. Skilbeck, R. Patel, B. Green, and G. Morley, "An open-source high-frequency lock-in amplifier," *Review of Scientific Instruments*, vol. 90, no. 9, p. 094701, 2019.

[47] T. Preuschoff, M. Schlosser, and G. Birkl, "Digital laser frequency and intensity stabilization based on the stemlab platform (originally red pitaya)," *Review of Scientific Instruments*, vol. 91, no. 8, p. 083001, 2020.

[48] J.-D. Deschenes, digital PLL code base, see https://github.com/jdes/Frequency-comb-DPLL.

[49] C. Cardenas-Olaya and C. Calosso, "Fully digital electronics for fiber-link frequency transfer implemented on red pitaya," *Proceedings of the GNU Radio Conference*, vol. 2, no. 1, Jan. 2021. [Online]. Available: https://pubs.gnuradio.org/index.php/grcon/article/view/95

[50] C. Olaya, A. C., S. Micalizio, M. Ortolano, C. E. Calosso, E. Rubiola, and J.-M. Friedt, "Digital electronics based on red pitaya platform for coherent fiber links," Apr. 2016, pp. 1–4.

[51] A. C. Cárdenas-Olaya, A. Tampellini, E. Bertacco, C. Clivati, A. Mura, D. Calonico, S. Micalizio, and C. E. Calosso, "Digital instrumentation for phase-coherent frequency transfer over 300 km fiber link," Apr. 2019, pp. 1–2.

[52] A. Didier, J. Millo, B. Marechal, C. Rocher, E. Rubiola, R. Lecomte, M. Ouisse, J. Delporte, C. Lacroûte, and Y. Kersalé, "Ultracompact reference ultralow expansion glass cavity," *Applied Optics*, vol. 57, no. 22, pp. 6470–6473, Aug. 2018.

[53] See http://cecill.info/index.en.html and https://spdx.org/licenses/CECILL-B.html#licenseText.

[54] P. A. Williams, W. C. Swann, and N. R. Newbury, "High-stability transfer of an optical frequency over long fiber-optic links," *JOSA B*, vol. 25, no. 8, pp. 1284–1293, Aug. 2008.

[55] A. C. C. Olaya, C. E. Calosso, J.-M. Friedt, S. Micalizio, and E. Rubiola, "Phase Noise and Frequency Stability of the Red-Pitaya Internal PLL," *IEEE Transactions on Ultrasonics, Ferroelectrics, and Frequency Control*, vol. 66, no. 2, pp. 412–416, Feb. 2019.

[56] A. C. Cárdenas-Olaya, E. Rubiola, J.-M. Friedt, P.-Y. Bourgeois, M. Ortolano, S. Micalizio, and C. E. Calosso, "Noise characterization of analog to digital converters for amplitude and phase noise measurements," *Review of Scientific Instruments*, vol. 88, no. 6, p. 065108, Jun. 2017.

Bibliography

[1] N. HINKLEY *et al.*, "An atomic clock with 10^{-18} instability," *Science*, vol. 341, no. 6151, pp. 1215–1218, 2013.

[2] B. BLOOM *et al.*, "An optical lattice clock with accuracy and stability at the 10^{-18} level," *Nature*, vol. 506, no. 7486, pp. 71–75, 2014.

[3] I. USHIJIMA, "Cryogenic optical lattice clocks with a relative frequency difference of 1×10^{-18}," *arXiv preprint arXiv:1405.4071*, 2014.

[4] N. HUNTEMANN *et al.*, "Single-ion atomic clock with 3×10^{-18} systematic uncertainty," *Physical Review Letters*, vol. 116, no. 6, p. 063001, 2016.

[5] S. M. BREWER *et al.*, "$^{27}Al^{+}$ Quantum-Logic Clock with a Systematic Uncertainty below 10^{-18}," *Physical review letters*, vol. 123, no. 3, p. 033201, 2019.

[6] S. HÄFNER *et al.*, "8×10^{-17} fractional laser frequency instability with a long room-temperature cavity," *Optics letters*, vol. 40, no. 9, pp. 2112–2115, 2015.

[7] W. R. MILNER *et al.*, "Demonstration of a timescale based on a stable optical carrier," *Physical Review Letters*, vol. 123, no. 17, p. 173201, 2019.

[8] J. M. ROBINSON *et al.*, "Crystalline optical cavity at 4 K with thermal-noise-limited instability and ultralow drift," *Optica*, vol. 6, no. 2, pp. 240–243, 2019.

[9] W. ZHANG *et al.*, "Ultrastable Silicon Cavity in a Continuously Operating Closed-Cycle Cryostat at 4 K," *Phys. Rev. Lett.*, vol. 119, p. 243601, 2017.

[10] D. MATEI *et al.*, "1.5 μm Lasers with Sub-10 MHz Linewidth," *Physical review letters*, vol. 118, no. 26, p. 263202, 2017.

[11] G. HERNÁNDEZ, "Fabry-Perot interferometers," 1988.

[12] E. BLACK, "An introduction to Pound–Drever–Hall laser frequency stabilization," *American Journal of Physics*, vol. 69, no. 1, pp. 79–87, 2001.

[13] A. E. SIEGMAN, *Lasers*. University Science Books, 1986.

[14] R. W. P. DREVER *et al.*, "A Gravity Wave Detector Using Optical Cavity Sensing," in *9th International Conference on General Relativity and Gravitation*, pp. 265–267, 1980.

[15] R. W. P. DREVER *et al.*, "Laser phase and frequency stabilization using an optical resonator," *Appl. Phys. B*, vol. 31, no. 2, pp. 97–105, 1983.

[16] E. RUBIOLA, *Phase noise and frequency stability in oscillators*. The Cambridge RF and microwave engineering series, Cambridge University Press, 2008.

[17] W. RILEY *et al.*, "Handbook of Frequency Stability Analysis." https://tsapps.nist.gov/publication/get_pdf.cfm?pub_id=50505, 2008.

[18] F. WALLS, "Phase noise issues in femtosecond lasers," *Proceedings of SPIE - The International Society for Optical Engineering*, 2001.

[19] D. ALLAN *et al.*, "Standard terminology for fundamental frequency and time metrology," in *Proceedings of the 42nd Annual Frequency Control Symposium*, pp. 419–425, 1988.

[20] D. ALLAN *et al.*, "A Historical Perspective on the Development of the Allan Variances and Their Strengths and Weaknesses," *IEEE transactions on ultrasonics, ferroelectrics, and frequency control*, vol. 63, no. 4, pp. 513–519, 2016.

[21] D. ALLAN *et al.*, "A Modified "Allan Variance" with Increased Oscillator Characterization Ability," in *Thirty Fifth Annual Frequency Control Symposium*, pp. 470–475, 1981.

[22] J. RUTMAN *et al.*, "Characterization of frequency stability in precision frequency sources," *Proceedings of the IEEE*, vol. 79, no. 7, pp. 952–960, 1991.

[23] S. T. DAWKINS *et al.*, "Considerations on the measurement of the stability of oscillators with frequency counters," *IEEE Transactions on Ultrasonics, Ferroelectrics, and Frequency Control*, vol. 54, no. 5, pp. 918–925, 2007.

[24] E. RUBIOLA *et al.*, "The Companion of Enrico's Chart for Phase Noise and Two-Sample Variances," 2022.

[25] T. KESSLER *et al.*, "Thermal noise in optical cavities revisited," *J. Opt. Soc. Am. B*, vol. 29, no. 1, pp. 178–184, 2012.

[26] M. GORODETSKY, "Thermal noises and noise compensation in high-reflection multilayer coating," *Physics Letters, Section A: General, Atomic and Solid State Physics*, vol. 372, 2008.

[27] H. B. CALLEN *et al.*, "On a Theorem of Irreversible Thermodynamics," *Phys. Rev.*, vol. 86, pp. 702–710, 1952.

[28] H. B. CALLEN *et al.*, "Irreversibility and Generalized Noise," *Phys. Rev.*, vol. 83, pp. 34–40, 1951.

[29] K. NUMATA *et al.*, "Thermal-noise limit in the Frequency Stabilization of Lasers with Rigid Cavities," *Phys. Rev. Lett.*, vol. 93, p. 250602, 2004.

[30] C. SALOMON *et al.*, "Laser stabilization at the millihertz level," *JOSA B*, vol. 5, no. 8, pp. 1576–1587, 1988.

[31] J. DIRSCHERL *et al.*, "A dye laser spectrometer for high resolution spectroscopy," *Optics Communications*, vol. 91, no. 1, pp. 131–139, 1992.

[32] "ULE VALUES." https://www.corning.com/.

[33] J. MILLO *et al.*, "Ultrastable lasers based on vibration insensitive cavities," *Physical Review A*, vol. 79, p. 53829, 2009.

[34] B. C. YOUNG *et al.*, "Visible Lasers with Subhertz Linewidths," *Phys. Rev. Lett.*, vol. 82, pp. 3799–3802, 1999.

[35] T. LEGERO *et al.*, "Tuning the thermal expansion properties of optical reference cavities with fused silica mirrors," *J. Opt. Soc. Am. B*, vol. 27, no. 5, pp. 914–919, 2010.

[36] K. G. LYON *et al.*, "Linear thermal expansion measurements on silicon from 6 to 340 K," *Journal of Applied Physics*, vol. 48, no. 3, pp. 865–868, 1977.

[37] C. M. CAVES, "Quantum-mechanical noise in an interferometer," *Phys. Rev. D*, vol. 23, pp. 1693–1708, 1981.

[38] H.-A. BACHOR *et al.*, "Quantum noise—a limit in photodetection," *Applied Physics B*, vol. 49, no. 4, pp. 291–300, 1989.

[39] O. MOR *et al.*, "Performance analysis of Drever-Hall laser frequency stabilization using a proportional+integral servo," *IEEE Journal of Quantum Electronics*, vol. 33, no. 4, pp. 532–540, 1997.

[40] A. LUDLOW *et al.*, "Optical atomic clocks," *Reviews of Modern Physics*, vol. 87, pp. 637–701, 2015.

[41] T. L. NICHOLSON *et al.*, "Systematic evaluation of an atomic clock at 2×10^{-18} total uncertainty," *Nature communications*, vol. 6, no. 1, pp. 1–8, 2015.

[42] T. ROSENBAND *et al.*, "Frequency Ratio of Al^{+} and Hg^{+} Single-Ion Optical Clocks; Metrology at the 17th Decimal Place," *Science*, vol. 319, no. 5871, pp. 1808–1812, 2008.

[43] C. BRADASCHIA *et al.*, "The VIRGO project: a wide band antenna for gravitational wave detection," *Nuclear Instruments and Methods in Physics Research Section A: Accelerators, Spectrometers, Detectors and Associated Equipment*, vol. 289, no. 3, pp. 518–525, 1990.

[44] A. ABRAMOVICI *et al.*, "Ligo: The laser interferometer gravitational-wave observatory," *science*, vol. 256, no. 5055, pp. 325–333, 1992.

[45] B. ABBOTT *et al.*, "Observation of a kilogram-scale oscillator near its quantum ground state," *New Journal of Physics*, vol. 11, no. 7, p. 073032, 2009.

[46] W. MARSHALL *et al.*, "Towards quantum superpositions of a mirror," *Physical Review Letters*, vol. 91, no. 13, p. 130401, 2003.

[47] C. CHOU *et al.*, "Optical clocks and relativity," *Science*, vol. 329, no. 5999, pp. 1630–1633, 2010.

[48] C. EISELE *et al.*, "Laboratory test of the isotropy of light propagation at the 10^{-17} level," *Physical Review Letters*, vol. 103, no. 9, p. 090401, 2009.

[49] A. BARTELS *et al.*, "Femtosecond-laser-based synthesis of ultrastable microwave signals from optical frequency references," *Opt. Lett.*, vol. 30, no. 6, pp. 667–669, 2005.

[50] Y. V. S. STADNIK *et al.*, "Enhanced effects of variation of the fundamental constants in laser interferometers and application to dark-matter detection," *Phys. Rev. A*, vol. 93, p. 063630, 2016.

[51] S. KOLKOWITZ *et al.*, "Gravitational wave detection with optical lattice atomic clocks," *Phys. Rev. D*, vol. 94, p. 124043, 2016.

[52] Y. LEVIN, "Internal thermal noise in the LIGO test masses: A direct approach," *Phys. Rev. D*, vol. 57, pp. 659–663, 1998.

[53] F. BONDU *et al.*, "Thermal noise in mirrors of gravitational wave interferometric antennas," *Physics Letters A*, vol. 246, pp. 227–236, 1998.

[54] G. COLE *et al.*, "Tenfold reduction of Brownian noise in high-reflectivity optical coatings," *Nature Photonics*, vol. 7, pp. 644–650, 2013.

[55] G. D. COLE *et al.*, "Low-noise substrate-transferred crystalline coatings for precision interferometry," in *Optical Interference Coatings 2016*, p. MB.5, Optica Publishing Group, 2016.

[56] G. COLE *et al.*, "Monocrystalline AlGaAs heterostructures for high-reflectivity high-Q micromechanical resonators in the megahertz regime," *Applied Physics Letters*, vol. 92, 2008.

[57] A. E. VILLAR *et al.*, "Measurement of thermal noise in multilayer coatings with optimized layer thickness," *Physical Review D*, vol. 81, no. 12, 2010.

[58] G. M. HARRY *et al.*, "Titania-doped tantala/silica coatings for gravitational-wave detection," *Classical and Quantum Gravity*, vol. 24, no. 2, p. 405, 2006.

[59] F. BRÜCKNER *et al.*, "Monolithic dielectric surfaces as new low-loss light-matter interfaces," *Opt. Lett.*, vol. 33, no. 3, pp. 264–266, 2008.

[60] G. M. HARRY *et al.*, "Thermal noise in interferometric gravitational wave detectors due to dielectric optical coatings," *Classical and Quantum Gravity*, vol. 19, no. 5, p. 897, 2002.

[61] L. CHEN *et al.*, "Vibration-induced elastic deformation of Fabry-Perot cavities," *Phys. Rev. A*, vol. 74, p. 053801, 2006.

[62] D. LEIBRANDT *et al.*, "Spherical reference cavities for frequency stabilization of lasers in non-laboratory environments," *Optics express*, vol. 19, no. 4, pp. 3471–3482, 2011.

[63] B. ARGENCE *et al.*, "Prototype of an ultra-stable optical cavity for space applications," *Optics express*, vol. 20, no. 23, pp. 25409–25420, 2012.

[64] Z. Y. TAI *et al.*, "Transportable 1555-nm Ultra-Stable Laser with Sub-0.185-Hz Linewidth*," *Chinese Physics Letters*, vol. 34, no. 9, p. 090602, 2017.

[65] S. HÄFNER *et al.*, "Transportable interrogation laser system with an instability of mod $\sigma_y = 3 \times 10^{-16}$," *Opt. Express*, vol. 28, no. 11, pp. 16407–16416, 2020.

[66] S. HERBERS *et al.*, "Transportable clock laser system with an instability of 1.6×10^{-16}," *Opt. Lett.*, vol. 47, no. 20, pp. 5441–5444, 2022.

[67] S. WEBSTER *et al.*, "Force-insensitive optical cavity," *Opt. Lett.*, vol. 36, pp. 3572–3574, 2011.

[68] M. L. KELLEHER *et al.*, "Compact, portable, thermal-noise-limited optical cavity with low acceleration sensitivity," *Opt. Express*, vol. 31, no. 7, pp. 11954–11965, 2023.

[69] L. MA *et al.*, "Delivering the same optical frequency at two places: accurate cancellation of phase noise introduced by optical fiber or other time-varying path," *Opt. Lett.*, no. 19, 1994.

[70] N. R. NEWBURY *et al.*, "Coherent transfer of an optical carrier over 251 km," *Opt. Lett.*, vol. 32, no. 21, pp. 3056–3058, 2007.

[71] T. J. PINKERT *et al.*, "Effect of soil temperature on optical frequency transfer through unidirectional dense-wavelength-division-multiplexing fiber-optic links," *Appl. Opt.*, vol. 54, pp. 728–738, 2015.

[72] K. C. LIN *et al.*, "Effects of gamma radiation on optical fibre sensors," *Optoelectronics, IEE Proceedings -*, vol. 151, pp. 12 – 15, 2004.

[73] D. R. GOZZARD *et al.*, "Characterization of optical frequency transfer over 154 km of aerial fiber," *Opt. Lett.*, vol. 42, no. 11, pp. 2197–2200, 2017.

[74] L. SLIWCZYNSKI *et al.*, "Characterization of the frequency transfer over 300 km of aerial suspended fiber," in *2016 European Frequency and Time Forum (EFTF)*, pp. 1–3, 2016.

[75] S. C. EBENHAG *et al.*, "Measurement and Analysis of Polarization Variations in an Optical Coherent Fiber Communication Network Utilized for Time and Frequency Distribution," 2018.

[76] W. KABISH *et al.*, "Theory of stimulated brillouin scattering in fibers for highly multimode excitations," *Phys. Rev. X*, vol. 14, p. 031053, 2024.

[77] A. FOTIADI *et al.*, "Brillouin interaction between two optical modes selectively excited in weakly guiding multimode optical fibers," *Sensors*, vol. 23, no. 3, 2023.

[78] P. A. WILLIAMS *et al.*, "High-stability transfer of an optical frequency over long fiber-optic links," *J. Opt. Soc. Am. B*, vol. 25, no. 8, pp. 1284–1293, 2008.

[79] N. GISIN *et al.*, "Polarization mode dispersion of short and long single-mode fibers," *Journal of lightwave technology*, vol. 9, no. 7, pp. 821–827, 1991.

[80] D. J. DERICKSON, "Fiber optic test and measurement," 1998.

[81] O. LOPEZ *et al.*, "86-km optical link with a resolution of 2×10^{-18} for RF frequency transfer," *The European Physical Journal D*, vol. 48, no. 1, pp. 35–41, 2008.

[82] C. INCORPORATED, "Corning SMF-28 ULL optical fiber," 2014.

[83] A. BAUCH *et al.*, "Comparison between frequency standards in Europe and the USA at the 10^{-15} uncertainty level," *Metrologia*, vol. 43, no. 1, p. 109, 2005.

[84] A. BROWN *et al.*, "A GPS receiver designed for carrier-phase time transfer," in *Proceedings of the 2000 National Technical Meeting of The Institute of Navigation*, pp. 364–370, 2000.

[85] M. A. LOMBARDI *et al.*, "Time and frequency measurements using the global positioning system," *Cal Lab: International Journal of Metrology*, vol. 8, no. 3, pp. 26–33, 2001.

[86] K. M. LARSON *et al.*, "Carrier-phase time transfer," *IEEE transactions on ultrasonics, ferroelectrics, and frequency control*, vol. 46, no. 4, pp. 1001–1012, 1999.

[87] T. GMBH, "New trends in two-way time and frequency transfer via satellite." Online, 2023.

[88] A. A-KLEIN *et al.*, "Absolute frequency measurement of a SF6 two-photon line by use of a femtosecond optical comb and sum-frequency generation," *Opt. Lett.*, vol. 30, no. 24, pp. 3320–3322, 2005.

[89] A. D. LUDLOW *et al.*, "Sr lattice clock at 1×10^{-16} fractional uncertainty by remote optical evaluation with a ca clock," *Science*, vol. 319, no. 5871, pp. 1805–1808, 2008.

[90] M. MUSHA *et al.*, "Coherent optical frequency transfer over 50-km physical distance using a 120-km-long installed telecom fiber network," *Optics Express*, vol. 16, no. 21, pp. 16459–16466, 2008.

[91] O. TERRA *et al.*, "Brillouin amplification in phase coherent transfer of optical frequencies over 480 km fiber," *Optics express*, vol. 18, no. 15, pp. 16102–16111, 2010.

[92] A. MATVEEV *et al.*, "Precision Measurement of the Hydrogen 1s-2s Frequency via a 920-km Fiber Link," *Physical Review Letters*, vol. 110, no. 23, p. 230801, 2013.

[93] C. CLIVATI *et al.*, "Measuring absolute frequencies beyond the gps limit via long-haul optical frequency dissemination," *Optics express*, vol. 24, no. 11, pp. 11865–11875, 2016.

[94] B. ARGENCE *et al.*, "Quantum cascade laser frequency stabilization at the sub-Hz level," *Nature Photonics*, vol. 9, no. 7, pp. 456–460, 2015.

[95] C. CLIVATI *et al.*, "The optical fiber link LIFT for Radioastronomy," in *2015 Joint Conference of the IEEE International Frequency Control Symposium & the European Frequency and Time Forum*, pp. 769–772, IEEE, 2015.

[96] M. FISCHER *et al.*, "New limits on the drift of fundamental constants from laboratory measurements," *Physical Review Letters*, vol. 92, no. 23, p. 230802, 2004.

[97] T. FORTIER *et al.*, "Precision atomic spectroscopy for improved limits on variation of the fine structure constant and local position invariance," *Physical Review Letters*, vol. 98, no. 7, p. 070801, 2007.

[98] H. MARION *et al.*, "Search for variations of fundamental constants using atomic fountain clocks," *Physical review letters*, vol. 90, no. 15, p. 150801, 2003.

[99] E. PEIK *et al.*, "New limit on the present temporal variation of the fine structure constant," in *AIP Conference Proceedings*, vol. 770, pp. 103–111, American Institute of Physics, 2005.

[100] A. SHELKOVNIKOV *et al.*, "Stability of the proton-to-electron mass ratio," *Physical Review Letters*, vol. 100, no. 15, p. 150801, 2008.

[101] R. WILCOX *et al.*, "Stable transmission of radio frequency signals on fiber links using interferometric delay sensing," *Optics letters*, vol. 34, no. 20, pp. 3050–3052, 2009.

[102] C. PELLEGRINI, "Overview of single pass free electron lasers," 2006.

[103] K. PREDEHL *et al.*, "A 920-kilometer optical fiber link for frequency metrology at the 19th decimal place," *Science*, vol. 336, no. 6080, pp. 441–444, 2012.

[104] S. M. F. RAUPACH *et al.*, "Brillouin amplification supports 1×10^{-20} uncertainty in optical frequency transfer over 1400 km of underground fiber," *Phys. Rev. A*, vol. 92, p. 021801, 2015.

[105] M. SCHIOPPO *et al.*, "Comparing ultrastable lasers at 7 x 10^{-17} fractional frequency instability through a 2220 km optical fibre network," *Nature Communications*, vol. 13, no. 1, p. 212, 2022.

[106] S. DROSTE *et al.*, "Optical frequency transfer over a single-span 1840-km fiber link," in *2013 Joint European Frequency and Time Forum $\&$ International Frequency Control Symposium (EFTF/IFC)*, pp. 1004–1006, 2013.

[107] F. STEFANI *et al.*, "Tackling the limits of optical fiber links," *JOSA B*, vol. 32, no. 5, pp. 787–797, 2015.

[108] N. CHIODO *et al.*, "Cascaded optical fiber link using the internet network for remote clocks comparison," *Optics express*, vol. 23, no. 26, pp. 33927–33937, 2015.

[109] D. CALONICO *et al.*, "High-accuracy coherent optical frequency transfer over a doubled 642-km fiber link," *Applied Physics B*, vol. 117, no. 3, pp. 979–986, 2014.

[110] K. S. KUDEYAROV *et al.*, "2.8 km fiber link with phase noise compensation for transportable Yb^+ optical clock characterization," *Laser Physics*, vol. 28, no. 10, p. 105103, 2018.

[111] K. BELOY, "Frequency ratio measurements at 18-digit accuracy using an optical clock network," *Nature*, vol. 591, no. 7851, pp. 564–569, 2021.

[112] M. BODINE *et al.*, "Optical atomic clock comparison through turbulent air," *Physical Review Research*, vol. 2, no. 3, p. 033395, 2020.

[113] L. C. SINCLAIR *et al.*, "Comparing optical oscillators across the air to milliradians in phase and 10^{-17} in frequency," *Phys. Rev. Lett.*, vol. 120, p. 050801, 2018.

[114] A. BERCY *et al.*, "Two-way optical frequency comparisons at 5×10^{-21} relative stability over 100-km telecommunication network fibers," *Physical Review A*, vol. 90, no. 6, p. 061802, 2014.

[115] M. R. DIETRICH *et al.*, "Use of a Microcontroller for Fast Feedback Control of a Fiber Laser," 2009.

[116] K. HUANG *et al.*, "Microcontroller-based locking in optics experiments," *Review of Scientific Instruments*, vol. 85, no. 12, p. 123112, 2014.

[117] T. PREUSCHOFF *et al.*, "Digital laser frequency and intensity stabilization based on the STEMlab platform (originally red pitaya)," *Review of Scientific Instruments*, vol. 91, no. 8, p. 083001, 2020.

[118] T. PRUTTIVARASIN *et al.*, "Compact field programmable gate array-based pulse-sequencer and radio-frequency generator for experiments with trapped atoms," *Review of Scientific Instruments*, vol. 86, no. 11, p. 115106, 2015.

[119] A. TOURIGNY-PLANTE *et al.*, "An open and flexible digital phase-locked loop for optical metrology," *Review of Scientific Instruments*, vol. 89, no. 9, p. 093103, 2018.

[120] L. C. SINCLAIR *et al.*, "Invited article: A compact optically coherent fiber frequency comb," *Review of Scientific Instruments*, vol. 86, no. 8, p. 081301, 2015.

[121] P. MAHNKE, "Characterization of a commercial software defined radio as high frequency lock-in amplifier for FM spectroscopy," *Review of Scientific Instruments*, vol. 89, no. 1, p. 013113, 2018.

[122] G. A. STIMPSON *et al.*, "An open-source high-frequency lock-in amplifier," *Review of Scientific Instruments*, vol. 90, no. 9, p. 094701, 2019.

[123] C. E. CALOSSO *et al.*, "Tracking DDS for coherent optical links," in *2013 Joint European Frequency and Time Forum & International Frequency Control Symposium (EFTF/IFC)*, pp. 885–888, 2013.

[124] C. C-OLAYA *et al.*, "Fully Digital Electronics for Fiber-Link Frequency Transfer Implemented on Red Pitaya," *Proceedings of the GNU Radio Conference*, vol. 2, no. 1, 2021.

[125] C. C-OLAYA and others., "Digital electronics based on red pitaya platform for coherent fiber links," in *2016 European Frequency and Time Forum (EFTF)*, pp. 1–4, 2016.

[126] C. C-OLAYA and others., "Digital Instrumentation for Phase-Coherent Frequency Transfer over 300 km Fiber Link," in *2019 Joint Conference of the IEEE International Frequency Control Symposium and European Frequency and Time Forum (EFTF/IFC)*, pp. 1–2, 2019.

[127] "Redpitaya documentation." https://redpitaya.readthedocs.io/en/latest/.

[128] "Digital signal processing framework." https://github.com/oscimp/oscimpDigital/.

[129] C. C. OLAYA *et al.*, "Phase Noise and Frequency Stability of the Red-Pitaya Internal PLL," *IEEE Transactions on Ultrasonics, Ferroelectrics and Frequency Control*, vol. 66, no. 2, pp. 412 – 416, 2019.

[130] M. MATUSKO *et al.*, "Automatic Characterization of a Fully-Digital Doppler Cancellation Technique for Local Ultra-Stable Frequency Dissemination," in *2023 Joint Conference of the European Frequency and Time Forum and IEEE International Frequency Control Symposium (EFTF/IFCS)*, pp. 1–4, 2023.

[131] A. DIDIER, *Développement de cavités Fabry-Perot ultra-stables pour références de fréquence optique de nouvelle génération*. PhD thesis, Université de Franche-Comté, 2016.

[132] A. DIDIER *et al.*, "Ultracompact reference ultralow expansion glass cavity," *Appl. Opt.*, vol. 57, no. 22, pp. 6470–6473, 2018.

[133] G. COLE *et al.*, "Substrate-transferred GaAs/AlGaAs crystalline coatings for gravitational-wave detectors," *Applied Physics Letters*, vol. 122, no. 11, p. 110502, 2023.

[134] G. COLE *et al.*, "High-performance near- and mid-infrared crystalline coatings," *Optica*, vol. 3, no. 6, pp. 647–656, 2016.

[135] D. KEDAR *et al.*, “Frequency stability of cryogenic silicon cavities with semiconductor crystalline coatings,” *Optica*, vol. 10, no. 4, pp. 464–470, 2023.

[136] J. YU *et al.*, “Excess noise and photoinduced effects in highly reflective crystalline mirror coatings,” *Phys. Rev. X*, vol. 13, p. 041002, 2023.

[137] A. DIDIER *et al.*, “Design of an ultra-compact reference ULE cavity,” *Journal of Physics: Conference Series*, vol. 723, no. 1, p. 012029, 2016.

[138] J. MILLO *et al.*, “Ultrastable lasers based on vibration insensitive cavities,” *Physical Review A*, vol. 79, no. 5, 2009.

[139] R. A. PAQUIN, *Handbook of Optics, Volume 2*. Citeseer, 1995.

[140] R. A. PAQUIN, “Materials for Optical Systems,” 2018.

[141] A. DIDIER *et al.*, “Ultra-low phase noise all-optical microwave generation setup based on commercial devices,” *Appl. Opt.*, vol. 54, no. 12, pp. 3682–3686, 2015.